NOTICE

AVIS

The quality of this microform is heavily dependent upon the quality of the original thesis submitted for microfilming. Every effort has been made to ensure the highest quality of reproduction possible.

If pages are missing, contact the university which granted the degree.

Some pages may have indistinct print especially if the original pages were typed with a poor typewriter ribbon or if the university sent us an inferior photocopy.

Reproduction in full or in part of this microform is governed by the Canadian Copyright Act, R.S.C. 1970, c. C-30, and subsequent amendments.

La qualité de cette microforme dépend grandement de la qualité de la thèse soumise au microfilmage. Nous avons tout fait pour assurer une qualité supérieure de reproduction.

S'il manque des pages, veuillez communiquer avec l'université qui a conféré le grade.

La qualité d'impression de certaines pages peut laisser à désirer, surtout si les pages originales ont été dactylographiées à l'aide d'un ruban usé ou si l'université nous a fait parvenir une photocopie de qualité inférieure.

La reproduction, même partielle, de cette microforme est soumise à la Loi canadienne sur le droit d'auteur, SRC 1970, c. C-30, et ses amendements subséquents.

Canadä

WAVE- AND WIND-DRIVEN FLOW ON THE CONTINENTAL SHELF

By

Zhigang Xu

Canadä

Name ___Zhiyang Xu, Zhigang Xu___

Dissertation Abstracts International is arranged by broad, general subject categories. Please select the one subject which most nearly describes the content of your dissertation. Enter the corresponding four-digit code in the spaces provided

___Oceanography___

Subject Categories

THE HUMANITIES AND SOCIAL SCIENCES

COMMUNICATIONS AND THE ARTS
Architecture	0729
Art History	0377
Cinema	0900
Dance	0378
Fine Arts	0357
Information Science	0723
Journalism	0391
Library Science	0399
Mass Communications	0708
Music	0413
Speech Communication	0459
Theater	0465

EDUCATION
General	0515
Administration	0514
Adult and Continuing	0516
Agricultural	0517
Art	0273
Bilingual and Multicultural	0282
Business	0688
Community College	0275
Curriculum and Instruction	0727
Early Childhood	0518
Elementary	0524
Finance	0277
Guidance and Counseling	0519
Health	0680
Higher	0745
History of	0520
Home Economics	0278
Industrial	0521
Language and Literature	0279
Mathematics	0280
Music	0522
Philosophy of	0998
Physical	0523

Psychology
Psychology	0525
Reading	0535
Religious	0527
Sciences	0714
Secondary	0533
Social Sciences	0534
Sociology of	0340
Special	0529
Teacher Training	0530
Technology	0710
Tests and Measurements	0288
Vocational	0747

LANGUAGE, LITERATURE AND LINGUISTICS
Language	
General	0679
Ancient	0289
Linguistics	0290
Modern	0291
Literature	
General	0401
Classical	0294
Comparative	0295
Medieval	0297
Modern	0298
African	0316
American	0591
Asian	0305
Canadian (English)	0352
Canadian (French)	0355
English	0593
Germanic	0311
Latin American	0312
Middle Eastern	0315
Romance	0313
Slavic and East European	0314

PHILOSOPHY, RELIGION AND THEOLOGY
Philosophy	0422
Religion	
General	0318
Biblical Studies	0321
Clergy	0319
History of	0320
Philosophy of	0322
Theology	0469

SOCIAL SCIENCES
American Studies	0323
Anthropology	
Archaeology	0324
Cultural	0326
Physical	0327
Business Administration	
General	0310
Accounting	0272
Banking	0770
Management	0454
Marketing	0338
Canadian Studies	0385
Economics	
General	0501
Agricultural	0503
Commerce Business	0505
Finance	0508
History	0509
Labor	0510
Theory	0511
Folklore	0358
Geography	0366
Gerontology	0351
History	
General	0578

Ancient	0579
Medieval	0581
Modern	0582
Black	0328
African	0331
Asia, Australia and Oceania	0332
Canadian	0334
European	0335
Latin American	0336
Middle Eastern	0333
United States	0337
History of Science	0585
Law	0398
Political Science	
General	0615
International Law and Relations	0616
Public Administration	0617
Recreation	0814
Social Work	0452
Sociology	
General	0626
Criminology and Penology	0627
Demography	0938
Ethnic and Racial Studies	0631
Individual and Family Studies	0628
Industrial and Labor Relations	0629
Public and Social Welfare	0630
Social Structure and Development	0700
Theory and Methods	0344
Transportation	0709
Urban and Regional Planning	0999
Women s Studies	0453

THE SCIENCES AND ENGINEERING

BIOLOGICAL SCIENCES
Agriculture	
General	0473
Agronomy	0285
Animal Culture and Nutrition	0475
Animal Pathology	0476
Food Science and Technology	0359
Forestry and Wildlife	0478
Plant Culture	0479
Plant Pathology	0480
Plant Physiology	0817
Range Management	0777
Wood Technology	0746
Biology	
General	0306
Anatomy	0287
Biostatistics	0308
Botany	0309
Cell	0379
Ecology	0329
Entomology	0353
Genetics	0369
Limnology	0793
Microbiology	0410
Molecular	0307
Neuroscience	0317
Oceanography	0416
Physiology	0433
Radiation	0821
Veterinary Science	0778
Zoology	0472
Biophysics	
General	0786
Medical	0760

EARTH SCIENCES
Biogeochemistry	0425
Geochemistry	0996

Geodesy	0370
Geology	0372
Geophysics	0373
Hydrology	0388
Mineralogy	0411
Paleobotany	0345
Paleoecology	0426
Paleontology	0418
Paleozoology	0985
Palynology	0427
Physical Geography	0368
Physical Oceanography	0415

HEALTH AND ENVIRONMENTAL SCIENCES
Environmental Sciences	0768
Health Sciences	
General	0566
Audiology	0300
Chemotherapy	0992
Dentistry	0567
Education	0350
Hospital Management	0769
Human Development	0758
Immunology	0982
Medicine and Surgery	0564
Mental Health	0347
Nursing	0569
Nutrition	0570
Obstetrics and Gynecology	0380
Occupational Health and Therapy	0354
Ophthalmology	0381
Pathology	0571
Pharmacology	0419
Pharmacy	0572
Physical Therapy	0382
Public Health	0573
Radiology	0574
Recreation	0575

Speech Pathology	0460
Toxicology	0383
Home Economics	0386

PHYSICAL SCIENCES

Pure Sciences
Chemistry	
General	0485
Agricultural	0749
Analytical	0486
Biochemistry	0487
Inorganic	0488
Nuclear	0738
Organic	0490
Pharmaceutical	0491
Physical	0494
Polymer	0495
Radiation	0754
Mathematics	0405
Physics	
General	0605
Acoustics	0986
Astronomy and Astrophysics	0606
Atmospheric Science	0608
Atomic	0748
Electronics and Electricity	0607
Elementary Particles and High Energy	0798
Fluid and Plasma	0759
Molecular	0609
Nuclear	0610
Optics	0752
Radiation	0756
Solid State	0611
Statistics	0463

Applied Sciences
Applied Mechanics	0346
Computer Science	0984

Engineering	
General	0537
Aerospace	0538
Agricultural	0539
Automotive	0540
Biomedical	0541
Chemical	0542
Civil	0543
Electronics and Electrical	0544
Heat and Thermodynamics	0348
Hydraulic	0545
Industrial	0546
Marine	0547
Materials Science	0794
Mechanical	0548
Metallurgy	0743
Mining	0551
Nuclear	0552
Packaging	0549
Petroleum	0765
Sanitary and Municipal	0554
System Science	0790
Geotechnology	0428
Operations Research	0796
Plastics Technology	0795
Textile Technology	0994

PSYCHOLOGY
General	0621
Behavioral	0384
Clinical	0622
Developmental	0620
Experimental	0623
Industrial	0624
Personality	0625
Physiological	0989
Psychobiology	0349
Psychometrics	0632
Social	0451

To my wife Fanny and son Harry

Contents

List of Tables

List of Figures

Abstract

An Eulerian description of mean wave forcing, under the effects of the Earth's rotation and fluid friction, is derived. A general set of equations for the mean flow that includes wave forces is established, and a linearized system is extracted for further study. The study of the linearized system focuses on the response of an Eulerian water column to wave forces, including a step function forcing and arbitrary forcing. The response to steady wave forcing yields a formula for wave-driven flow which unifies the early work of Longuet-Higgins (1957), Hasselmann (1970), and Madsen (1978). Generalization of the results obtained with monochromatic waves to random waves is briefly discussed. Implication of the wave-driven flow to classical shelf dynamics is discussed with an example. A pre-existing CASP data set was explored to test the theory of wave driven flow. The results from this preliminary exploration emphasize the need for an experiment specially designed for investigating flows driven by Coriolis-induced wave stress.

The second part of the thesis introduces a new method for the numerical modelling of the linearized three-dimensional equations for shelf circulation. The method makes full use of the local water column response to Heaviside step force in modelling the global response to arbitrary external forcing in a three-dimensional domain. It is shown that the method can save substantial computational time. This can be valuable in a problem involving repeated integration of the equations of motion, such as data assimilation. An optimum velocity splitting form is also provided for accelerating the convergence of the calculation. Also discussed is the advantage of the $\eta - Q$ grid, which is introduced during the development of the method.

List of Symbols

English Letters

A_n	decomposition of velocity, $q \sim A_n \cos \omega_n z$ in the discussion of the comparison of the transport method with other methods
$\mathcal{A}$	real part of $R_{1\eta}^{(1)}$
a	wave amplitude
a_n	coefficient in Fourier expansion of $\mathrm{SE}(z)$
$\mathcal{B}$	imaginary part of $R_{1\eta}^{(1)}$
$\mathrm{BW}(\beta z')$	distribution of q_1 within the bottom wave boundary layer $(z' = z + h)$
$\mathrm{BE}(z)$	bottom Ekman spiral induced by sea surface slope
b_n	an eigenvalue which sets timescale for decay of inertial oscillations
C_1, C_2, C_3	used in Chapter 5 as the coefficients of wind stress Stokes drift and sea surface slope in the regression model
$\hat{C}_1, \hat{C}_2, \hat{C}_3$	least squares estimates of C_1, C_2, C_3
C_d	drag coefficient used in converting wind velocities to wind stresses
$C(z)$	a steady vertical profile; it can signify $\mathrm{BE}(z)$, $\mathrm{SE}(z)$, or $\mathrm{WA}(z)$
c_n	coefficient of Fourier expansion of $\mathrm{BE}(z)$

D_d, D_s	depth integral of $DE(z)$ and $BE(z)$ respectively
DRSS	drop in RSS due to increase in number of predictors in the regression analysis
E	expectation operator
E_n	$\sum E_n$ is a series representation of D_d
e_{ij}	rate of strain tensor
er_1	truncation error for $\sum E_n$
er_2	truncation error for $\sum G_n$
$F(t)$	forcing due to wind, waves or sea surface slope
F_s, F_b	surface stress, bottom stress
$\mathcal{F}(\Omega_n)e^{i\Omega_n t}$	Fourier component of $\mathfrak{R}(t)$
$\mathcal{F}'(\Omega_n)e^{i\Omega_n t}$	Fourier component of $\mathfrak{R}_r(t)$
F_i	F-value for regression predictor of wind, wave and sea surface slope when $i = 1, 2, 3$, respectively
FW(z)	vertical distribution of $q_{ws}^{(3)}$
f	Coriolis parameter
G_n	$\sum G_n$ is a series representation of D_s
g	gravitational acceleration
$H(t)$	Heaviside step function
h	water depth
HS(t)	significant wave height
$\mathcal{H}$	a $3 \times n$ data matrix when used in the regression analysis
i	$i = \sqrt{-1}$; also used as subscript to index various quantities
I_τ, I_{st}, $I_{\nabla\eta}$	Heaviside step functions for wind, wave, and slope forces
j	$(= 0, 1, 2, ...)$ a time stepping index
k, k_x, k_y	the total wavenumber and its x and y components, $(k_x^2 + k_y^2 = k^2)$

$\vec{s}$	tangential direction of $\Pi(x,y,z) = 0$ at O
$S(\sigma)$	wave energy spectrum
$SE(z)$	wind-induced surface Ekman spiral
$\mathcal{S}$	another notation for surface Stokes drift, whose parenthetical zero denotes origin in time, as distinct from $q_{st}(0)$ whose parenthetical zero means the origin of vertical coordinate (see explanation in text, page 14).
$\mathcal{S}_r$	a Monte Carlo simulation of surface value Stokes drift time series
L_1, L_2, L_3	wind driven, wave driven, and slope driven linear systems
l, m	grid point indices
$PD(t)$	wave direction at the peak of wave spectrum
$\vec{n}$	normal direction of $\Pi(x,y,z) = 0$ at O
O	a reference point on the wave profile $\Pi(x,y,z) = 0$
P_{ns}	tangential stress on wave profile $\Pi(x,y,z) = 0$
P_{ij}	stress tensor
$\tilde{p}$	wave dynamic pressure
$<p>$	time mean pressure
Q	complex transport $(= \int_{-h}^{0} q\,dz)$
$Q_d(t; I_\tau)$	transport induced by unit wind force
$Q_s(t; I_{\nabla\eta})$	transport induced by unit slope force
$Q^{(k+1)}$	transport at $t = (k+1)\Delta t$
q	complex mean velocity $(=<u> +i<v>)$
$q_d(t, z; I_\tau)$	response of L_1 to unit wind force
$\dot{q}_d(t, z; I_\tau)$	response of L_1 to δ function wind force
$q_w(t, z; I_{st})$	response of L_2 to unit Stokes drift
$\dot{q}_w(t, z; I_{st})$	response of L_2 to δ function Stokes drift
$q_s(t, z; I_{\nabla\eta})$	response of L_3 to unit slope force

$\dot{q}_s(t, z; I_{\nabla\eta})$	response of L_3 to δ function slope force
q_{st}, $q_{st}(0)$, $q_{st}(-h)$	mean Stokes drift, its surface value, and bottom value
q_l, q_e,	Lagrangian and Eulerian mean velocity
q_{ds}, q_{ws}, q_{ss},	steady flow driven by wind, slope forces, and Stokes
$q_{ws}^{(1)}$, $q_{ws}^{(2)}$, $q_{ws}^{(3)}$	parts of q_{ws}
q_{wt}	transient response of a water column to a step function of wave forcing
$q^{(k+1)}$, q^{∞}	velocity at time $t = (k+1)\Delta t$ and as $t \to \infty$
q_0	complex observed velocity
q_{04}	observed velocity at $z = -4m$
$R(t; F)$, $R(t; 1)$	response (velocity, transport, etc) of water column to arbitrary forcing and step function unit force
$\dot{R}(t; 1)$	time derivative of $R(t; 1)$; signifies response to δ function
$R_F^{(k)}$	represents $R(t = k\Delta t; F)$
$R_{1\tau}^{(1)}$, $R_{1\eta}^{(1)}$	response to a unit τ and a unit $\nabla\eta$ in a single time step
RSS	residual square sum
$\Re$	real part of complex quantity
$r_n(t; F)$	nth Fourier component of $R(t; F)$; it signifies the response of nth eigen-mode to an arbitrary force
$r_{nF}^{(0)}$, $r_{n1}^{(1)}$, $r_{nF}^{(k)}$	represents $r_n(t = 0, F)$, $r_n(t = \Delta t, F)$, $r_n(t = k\Delta t, F)$
s_n	coefficient of Fourier expansion of WA(z)
t	time
u, v, w	x-, y- and z- velocity components
u_i	represents u, v, w when i=1, 2, 3
$<u>$, $<v>$, $<w>$	time mean velocity components
$\tilde{u}$, $\tilde{v}$, $\tilde{w}$	wave orbital velocity components
u', v', w'	turbulent velocity components

u_1, w_1	the first order velocity component
	(i.e., wave orbital velocity $\tilde{u}, \tilde{v}$)
u_2, w_2	the second order (mean flow) velocity components
$- <\tilde{u}_i\tilde{u}_j>$	kinematic wave Reynolds' stresses
u_{1invis}, u_{1vis}	the inviscid and viscid parts of u_1
$WA(z)$	vertical profile of wave-induced flow
x, y, z	right hand Cartesian coordinates
z'	vertical coordinate relative to seabed ($z' = z + h$)

Greek Letters

α	$(1 + i)/\delta_e$
β	$= 1/\delta_w$
γ_n	$= \frac{\omega_n h}{\sqrt{2}}\left(\frac{\delta_e}{h}\right)$
∇	$= \partial/\partial x + i\partial/\partial y$
∇^*	$= \partial/\partial x - i\partial/\partial y$
$\delta(t)$	Dirac delta function
δ_e	Ekman depth ($= \sqrt{2\nu/f}$)
δ_{st}	Stokes depth ($= 1/(2k)$)
δ_w	wave boundary layer thickness ($= \sqrt{2\nu/\sigma}$)
$\delta\eta_1, \delta\eta_2, \delta\eta_3$	used in Figure (6.3) to represent the difference
$\delta u_1, \cdots, \delta u_5$	between results of Heaps' method and the transport
$\delta v_1, \cdots, \delta v_5$	method
$\nabla\eta$	sea surface slope
$\nabla\eta^\infty$	sea surface slope in Heaps' basin when $t \to 0$
ε	($= ka$) a small parameter in the perturbation expansion
	for the weakly nonlinear wave problem
$\epsilon(x, y, z)$	density anomaly

η	instantaneous sea surface elevation $(=<\eta>+\tilde{\eta})$. It also stands for the mean sea surface elevation in the text concerning exclusively the slowly varying motion.
$\tilde{\eta}$	sea surface fluctuation due to surface waves
$<\eta>$	mean sea level.
η^{∞}	sea surface elevation in Heaps' basin when $t \rightarrow \infty$.
θ	wave direction with respect to the x-axis
κ	linear bottom friction coefficient
Λ	derived vertical scale of surface waves $(= k/\sqrt{1 - (f/\sigma)^2})$
μ, ν	dynamic and kinematic viscosities (used for both laminar and turbulent flows)
ξ_n	$\frac{\sin 2\omega_n h}{2\omega_n h}$ a "slip" parameter; $\xi_n \rightarrow 0$ as $\kappa \rightarrow \infty$, corresponding to a non-slip case·
Π	$[= z - a\cos(kx - \sigma t)]$ $\Pi = 0$ describes a wave profile
σ	wave frequency
ρ_a	air density
ρ	sea water density
$\tilde{\tau} = \tilde{\tau}_x + i\tilde{\tau}_y$	virtual wave stress at the mean sea surface
$\tau = \tau_x + i\tau_y$	wind stress
τ_x^b, τ_y^b	bottom stresses in x- and y- directions
τ_{xz}, τ_{yz}	internal frictional stress in x- and y-directions on a plane normal to z-axis
$\phi_n(z)$	Fourier component of $C(z)$
ϕ	wave phase
$\phi(\Omega_n)$	phase of $F(\Omega_n)$
$\phi'(\Omega_n)$	phase of $F'(\Omega_n)$

$\psi(z)$ vertical distribution of wave stress within the thin bottom wave boundary layer

$\Psi(z)$ $[= F_s\Psi_s(z) + F_b\Psi_b(z)]$ a specified velocity profile

$\Psi_s(z)$ a specified velocity which is confined near the surface

$\Psi_b(z)$ a specified velocity which is confined near the bottom

λ_n shorthand for $e^{-b_n\Delta t}$, used in the recursion schemes of evaluating time convolutions

ω_n eigenvalues for the Ekman dynamic problem

λ complex cross-correlation function between winds and waves

Miscellaneous

ℓ eigenvalue of the Ekman dynamic problem with arbitrary eddy viscosity profile

$<\quad>$ a time-average over a few wave periods

$*$ convolution in time

Acknowledgements

I would like to thank my supervisor, Dr. Tony Bowen, for his guidance, for his encouragement to publish papers, and for giving me the freedom to do my own research. My thanks also go to Drs. Keith Thompson, Dan Wright, and Bill Hyde for serving on my thesis committee. Their valuable suggestions and criticisms made this thesis stronger. I would also like to thank my external examiner, Dr. Paul LeBlond from the University of British Columbia for his high evaluation of this thesis. His words made me feel all the suffering that I have gone through in the course of my Ph. D journey worthwhile!

Dr. Carl Anderson is acknowledged for introducing me to Dr. Fred Dobson and Mr. Bash Toulaney at BIO (Bedford Institute of Oceanography, Canada), who graciously provided me with the CASP wave data set. Dr. Barry Ruddick is thanked for teaching me one and a half years in fluid dynamics and ocean dynamics, and for his easy accessibility. Dr. Dan Kelley is thanked for scientific discussions from time to time and for setting up his Gri graphics package at BIO for me.

Thanks also to Mr. Michael Dowd, Ms. Karen Fisher and Dr. David Walsh for their English editing of this thesis. Dr. David Walsh is also thanked for playing badminton with me, and for teaching me American slang, especially off-colour expressions. Comrade Joško Bobanović is thanked for chatting with me about communism and capitalism, Chairman Mao and President Tito, and wine and women. Thanks to Mr. Yinshuo (Poppy) Shen and Mr. Lingqi Zhang for their friendship and for their appreciation of my work.

Special thanks go to Dr. John Loder at BIO for providing me with a contract during the process of the thesis reviewing/revising. The contract gave me decent financial support and a new research environment. His flexibility in allowing me to switch back and forth between Dalhousie and BIO is also greatly appreciated.

I am deeply grateful to my wife, Yanfang (Fanny) Chen, for her sacrifice, understanding, and full support. My boy, Harry, also helped me in his own way. When I got home from school, his greeting, stories about his school, etc., made all my tensions disappear quickly.

Chapter 1

Introduction

1.1 Preface

Two topics are covered by this thesis: the inclusion of a mean wave forcing in the linearized shallow water equations and the presentation of a new numerical method to solve the equations. The wave force is related to the concept of Stokes drift. The numerical method results from implementing an outstanding idea proposed by Welander in 1957. Each topic is self contained, but the two are linked: the former studies the response of an Eulerian water column to the local external forces; the latter provides a way of "assembling" the column-wise motion into a 3-D dynamic picture. Detailed introductions to these topics are given below, followed by an outline of the thesis.

1.2 Stokes drift

Stokes (1847) established a theory for wave-induced mean flow in a non-rotating frame. It predicts that for a periodic surface wave field there is an associated mean flow in the direction of wave propagation. Since this mean flow can be responsible for a net material transport of sediments, oil slicks, etc., the concept, which came to be known as Stokes drift, has been widely applied in the real ocean. Not until
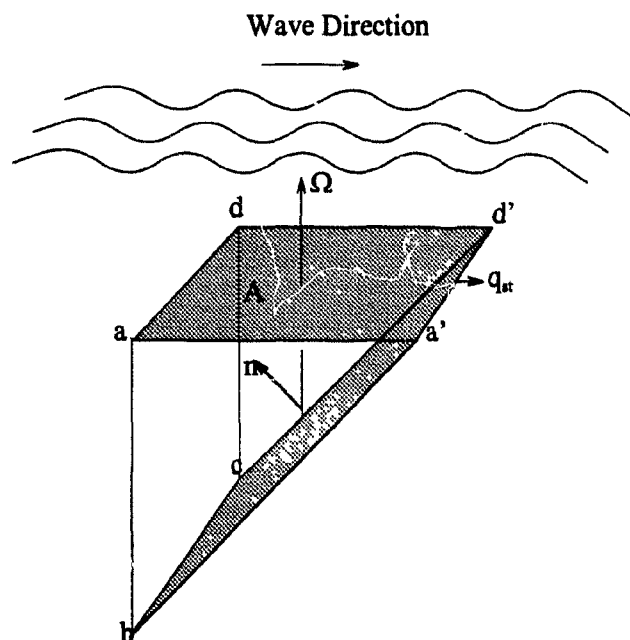
Figure 1.1: Diagram illustrating Ursell's argument. Given a steady Lagrangian mean flow, denoted by q_{st}, the area projection, A, of a circuit would increase without bound, as would the number of the captured planetary-vorticity filaments, Ω. This would lead to an infinitely large relative circulation around the circuit $ba'd'cb$ which initially coincided with $badc$. The end result is then an infinitely large velocity along the side $d'a'$ whose length is finite.

1950 did Ursell question the application of Stokes' theory to the rotating ocean. He argued, from the viewpoint of absolute circulation conservation, that it is impossible for a steady wave field to produce a steady Lagrangian mean flow (Fig. 1.1). Pollard (1970) then examined the wave problem in Lagrangian coordinates including Coriolis force showing that each water particle experiences an exactly circular orbit so that there is no net material transport, confirming Ursell's theory.

Hasselmann (1970) also retained the Coriolis force in calculating the wave-induced

Reynolds' stress tensor and found that, when the earth's rotation is taken into account, the horizontal component of the wave orbital velocity is no longer in quadrature with its vertical counterpart. As a result a mean shear component in the Reynolds' stress tensor arises. The associated body force exerted by the waves is $-\mathbf{f} \times \mathbf{q}_{st}$, where $\mathbf{f}$ is the Coriolis vector and $\mathbf{q}_{st}$ is the Stokes drift velocity. The steady response of a laterally homogeneous ocean to this body force is an Eulerian current $\mathbf{q}_e$ which is equal and opposite to the Stokes drift, resulting in the zero Lagrangian mean required by Ursell's theory.

An interesting result is that a high frequency surface gravity wave field produces shear stresses in the water column due to the earth's rotation. As will be shown later, for a simple wave train the Coriolis-induced wave stress at the surface can be expressed as $\rho a^2 \sigma f / 2$ in deep water where ρ is the density of sea water, a is the wave amplitude, σ is the wave frequency, and f is the Coriolis parameter. Supposing $a = \sqrt{2}m$, $\sigma = 1s^{-1}$ (corresponding to about a 6 second wave period), $f = 10^{-4}s^{-1}$, and $\rho = 10^3 kgm^{-3}$, then the stress is $0.1Pa$, which is of the order of a typical wind stress. For large swells, the shear stress can be much larger. Unlike Longuet-Higgins' wave radiation stress (1960, 1964) whose existence depends on a horizontal gradient of the wave energy, this type of stress exists wherever surface waves are present. However, it has not to date been included in the usual equations describing shelf dynamics.

For a non-rotating frame, Longuet-Higgins (1953, 1960) showed that the presence of thin viscous wave boundary layers at the surface and at the bottom can strongly influence the mass transport in the interior region, regardless of how small the viscosity. This influence can be expressed in terms of two boundary conditions: a steady bottom streaming, and a surface virtual tangential stress. Predictions using the formula for viscous wave mass transport obtained by Longuet-Higgins yield good agreement with the wave tank data, while Stokes drift theory does not.

Thus Stokes' drift theory is markedly modified by rotation and viscosity effects. In a realistic ocean, one should therefore consider both these effects in addressing the

wave-induced flow problem. Madsen (1978), followed by Weber (1983a,b) and Jenkins (1986, 1987a,b), combined the Coriolis and viscous effects in calculating the wave mass transport in deep water and successfully removed the so-called Longuet-Higgins paradox in deep water. This paradox, which was noted first by Huang (1970), arises simply because the virtual tangential stress remains unbalanced in a non-rotating infinitely deep ocean.

In the models of Madsen (1978) and Weber (1983a,b), the eddy viscosity was assumed to be constant and waves monochromatic. Jenkins (1987a,b, 1989) developed models for vertically varying eddy viscosity and for the random wave case. Recently, Weber and Melsom (1993a, b) considered the effects of growing/breaking waves on the mass transport.

However, no one seems to have extended the work of Madsen, Weber and Jenkins to shallower water where surface waves may influence the whole water column. For example, swells of about 20s period can influence the whole water column to depths of about 200m (Grant *et al*, 1984). During periods of large swell, it seems unlikely that any dynamic model whose aim is to forecast or hindcast the real flow can confidently neglect the wave stress. One of the purposes of this thesis is therefore to present a simple Eulerian model for wind- and wave-driven flow in water of finite depth. Such a model should be of value in interpreting observed flow on a shelf.

1.3 Welander's idea

Welander's (1957) idea concerns the numerical solution of the following set of linearized equations

$$
\left.
\begin{array}{l}
\frac{\partial u}{\partial t} - fv = -g\frac{\partial \eta}{\partial x} + \frac{\partial}{\partial z}\left(\nu\frac{\partial u}{\partial z}\right) \\
\frac{\partial v}{\partial t} + fu = -g\frac{\partial \eta}{\partial y} + \frac{\partial}{\partial z}\left(\nu\frac{\partial v}{\partial z}\right) \\
\frac{\partial \eta}{\partial t} + \frac{\partial}{\partial x}\int_{-h}^{0} u\,dz + \frac{\partial}{\partial y}\int_{-h}^{0} v\,dz = 0
\end{array}
\right\}
\tag{1.1}
$$

where $x - y - z$ forms a right handed Cartesian coordinate system, t is time, u and v are the velocity components in the $x-$ and $y-$directions respectively, h is the water

depth, η is the sea surface elevation, f is the Coriolis parameter, ν is the eddy viscosity, and g is the acceleration due to the gravity. This system of equations has often been used as a mathematical model for physical oceanography problems such as tidal flow, storm surge prediction, and shelf circulation. However, even for very simple basins, few complete analytical solutions are known. Although the set of Eqs. (1.1) has been greatly simplified from the full Navier-Stokes equations, it still includes a mixture of Ekman and long wave dynamics. Therefore it is necessary to take a numerical approach to obtain general solutions.

However, before integrating the equations numerically, we may be able to extract the Ekman dynamics analytically. This is the idea proposed by Welander (1957). Specifically, he suggested that the two momentum equations can be solved for a complex velocity $q = u + iv$ in terms of a known wind stress, τ, and an unknown sea surface slope, $\nabla \eta$,

$$q = q(t, z; \nabla \eta, \tau). \tag{1.2}$$

As will be seen later, Eq. (1.2) can be written in the form of a pair of time convolutions, one with the wind force, and the other with the surface slope. In practice, the wind stress is given. If the slope force were also given, then knowledge of the velocity field would be complete. To determine $\nabla \eta(t)$, Welander suggested two approaches (Table 1.1). The first approach (the bottom stress approach) is to take the derivative of q with respect to z and evaluate it at the sea bed to get an analytical expression for the bottom stress. The bottom stress can then be substituted into the depth averaged equations to numerically solve for the sea surface elevation, η, and the depth averaged velocity components, $\bar{u}$ and $\bar{v}$. The second approach (the transport approach) integrates q over the water column to get a transport. The transport can then be substituted into the continuity equation to numerically solve for η. Both are variations of the convolution method. The difference between the two approaches lies in the way they supply the local force $\nabla \eta(t)$ for the convolution.

Jelesnianski (1970) implemented Welander's first suggestion, the bottom stress approach, and developed a model for storm surge prediction. Forristall (1974, 1977,

Table 1.1: This table summarizes Welander's two suggestions for solving linearized shallow water equations. $q_d(t, z; I_\tau)$ and $q_s(t, z; I_{\nabla\eta})$ are two complex velocities induced by unit constant wind stress, I_τ, and unit sea surface slope, $I_{\nabla\eta}$. A unit vector here is defined as a vector whose length is one unit and whose angle is arbitrary. The dots on q_s and q_d indicate time derivatives.

$$\left. \begin{array}{l} \frac{\partial u}{\partial t} - fv = -g\frac{\partial \eta}{\partial x} + \nu\frac{\partial^2 u}{\partial z^2} \\[2mm] \frac{\partial v}{\partial t} + fu = -g\frac{\partial \eta}{\partial y} + \nu\frac{\partial^2 v}{\partial z^2} \end{array} \right\} \implies \left\{ \begin{array}{l} q = \nabla\eta * \dot{q}_s(t, z; I_{\nabla\eta}) \\[2mm] \quad + \tau * \dot{q}_d(t, z; I_\tau) \end{array} \right.$$

Jelesnianski, 1970

Bottom stress approach

$$\left. \begin{array}{l} \frac{\partial \eta}{\partial t} + \frac{\partial h\bar{u}}{\partial x} + \frac{\partial h\bar{v}}{\partial y} = 0 \\[2mm] \frac{\partial \bar{u}}{\partial t} - f\bar{v} = -g\frac{\partial \eta}{\partial x} + \frac{\tau_x^s - \tau_x^b}{h} \\[2mm] \frac{\partial \bar{v}}{\partial t} + f\bar{u} = -g\frac{\partial \eta}{\partial y} + \frac{\tau_y^s - \tau_y^b}{h} \end{array} \right\} \quad \overset{\nabla\eta}{\underset{(\tau_x^b,\tau_y^b)}{\rightleftarrows}} \quad \left\{ \begin{array}{l} (\tau_x^b, \tau_y^b) = \nabla\eta * \left.\frac{\partial \dot{q}_s}{\partial z}\right|_{z=-h} \\[2mm] \quad + \tau * \left.\frac{\partial \dot{q}_d}{\partial z}\right|_{z=-h} \end{array} \right.$$

	Welander's first
	suggestion

This study

Transport approach

$$\frac{\partial \eta}{\partial t} + \frac{\partial h\bar{u}}{\partial x} + \frac{\partial h\bar{v}}{\partial y} = 0 \quad \overset{\nabla\eta}{\underset{(h\bar{u},h\bar{v})}{\rightleftarrows}} \quad \left\{ \begin{array}{l} (h\bar{u}, h\bar{v}) = \nabla\eta * \int_{-h}^0 \dot{q}_s dz \\[2mm] \quad + \tau * \int_{-h}^0 \dot{q}_d dz \end{array} \right.$$

Welander's
second suggestion

1980) applied Jelesnianski's method to model storm-generated currents and later extended the method to the case of two layers of different (but constant within each layer) eddy viscosity. Davies (1987, 1988) took this method one step further, using the bottom stress derived from a linear depth-dependent model to provide closure for a non-linear depth-averaged model. One difficulty with the bottom stress approach is the extremely slow convergence of the bottom stress series. As a result, approximate formulae have been used to replace this bottom stress series (Hearn, 1988; Hunter, 1989). Such approximations, due to underestimation of the correct bottom stress, tend to produce the undamped inertial oscillations reported by Davies (1987) and Hunter and Hearn (1988) .

Welander was interested in implementing his second idea, the transport approach, and planned to perform some numerical experiments for the North Sea. By 1961, however, he acknowledged the difficulty of the implementation due to the complexity of the integrodifferential equation. This difficulty was also recognized by others (Platzman, 1963; Simons, 1980; Murty, 1984).

However, Welander's second suggestion has certain advantages: only one equation (the continuity equation) needs to be integrated numerically; the analytical part only involves the transport, which implies that fewer modes will be needed (since higher modes have little contribution to the transport). It is desirable to implement the method, as it can result in a substantial decrease in the computational workload. This is valuable for problems involving many iterations of the solutions to the 3-D linearized equations of motion, such as data assimilation. This study implements Welander's second approach, resulting in a new method for numerical modelling of 3-D circulations in shallow seas.

1.4 Thesis outline

This thesis is structured as follows.

- Chapter 2 derives both the Coriolis- and viscosity-induced wave stresses for arbitrary water depth and arbitrary wave direction.

- Chapter 3 establishes a set of general equations which includes the mean wave force, and extracts a set of linearized sub-systems for use in the following chapters.

- Chapter 4 studies in detail how a water column responds to the local external wave force.

- Chapter 5 uses a pre-existing data set, the CASP (Canadian Atlantic Storm Program, 1985-1986) data set to test the theory established in Chapter 4 against data.

- Chapter 6 moves on to the second aspect of the thesis: presenting the new method for numerically modelling the linearized 3-D motion in shallow seas.

- Chapter 7 summarizes the thesis.

Chapter 2

Primary Wave Motion with Coriolis Effects and Secondary Wave Stress

2.1 Introduction

This chapter derive₋ both the Coriolis-induced and viscosity-induced wave stresses for arbitrary water depth and arbitrary wave direction. A succinct and rigorous derivation of Longuet-Higgins' virtual wave stress is presented here. It is shown that the virtual stress is a projection on the surface slope of two viscous normal stresses acting on the vertical and horizontal planes.

Hasselmann (1970) derived the Coriolis-induced wave stress without resorting to any specific wave solution. His derivation is general, but also makes the generating mechanism of the stress less evident. In the following, a finite water depth wave solution in a rotating system is provided, from which one can see the generating mechanism of the stress more clearly and can immediately determine the stress formula in terms of the wave parameters.

In the wave mass transport problem, the Lagrangian description is often favored

(Ünlüata and Mei, 1970; Madsen, 1978; Weber, 1983a,b; Jenkins, 1986, 1987). The choice of the Lagrangian description brings in an evident convenience, *i.e.*, turning the fluctuating free surface into a fixed plane, which is desirable for those models designed to yield the detailed structure of the surface boundary layer. However the choice complicates the equations of motion and makes the algebra lengthy. In conventional models for wind-driven shelf circulation, the Eulerian description is over-w' elmingly used. One of the purposes of this thesis is to explore the consequence of introducing wave forcing into the commonly used equations for wind-driven circulation. Therefore it will be convenient to adopt the Eulerian description here. After obtaining results from the Eulerian model, for the purpose of comparison with the previous results in the Lagrangian description, one can employ a simple relationship of $q_l = q_e + q_{st}$, where q_l is the Lagrangian mean, q_e the Eulerian mean and q_{st} the Stokes drift (e.g. Longuet-Higgins, 1969a). For a general dynamic link between the two descriptions, reference is made to Andrews and McIntyre (1978). Weber (1990) also gave a comparison of the two approaches for the specific case of wave mass transport in a deep rotating ocean.

2.2 Inviscid primary wave motion in the interior region and the Coriolis-induced wave stress

For the first order wave motion, a frictionless model is a reasonable approximation for the interior region away from the viscous boundary layer. The linearized equations of motion in a Cartesian frame rotating with angular frequency of $f/2$ are

$$\frac{\partial \tilde{u}}{\partial t} - f\tilde{v} = -\frac{1}{\rho}\frac{\partial \tilde{p}}{\partial x} \tag{2.1}$$

$$\frac{\partial \tilde{v}}{\partial t} + f\tilde{u} = 0 \tag{2.2}$$

$$\frac{\partial \tilde{w}}{\partial t} + g = -\frac{1}{\rho}\frac{\partial \tilde{p}}{\partial z} \tag{2.3}$$

$$\frac{\partial \tilde{u}}{\partial x} + \frac{\partial \tilde{w}}{\partial z} = 0 \tag{2.4}$$
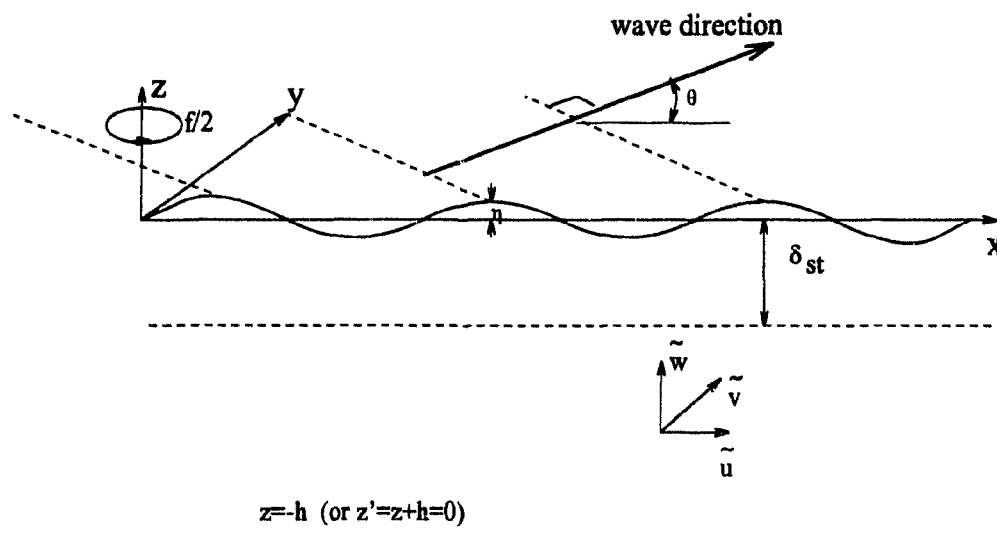
Figure 2.1: Eulerian coordinates for the wave problem in a rotating ocean of constant depth. In the solution for $\tilde{u}$, $\tilde{v}$, $\tilde{w}$, $\tilde{p}$ and $\tilde{\eta}$, the wave propagation direction θ is assumed to be zero for simplicity initially, and afterwards this simplification relaxed.

subject to

$$\tilde{w} = 0 \qquad \text{at } z = -h \tag{2.5}$$

$$\tilde{p} = 0 \qquad \text{at } z = 0 \tag{2.6}$$

where the x-axis is taken to be the direction of wave propagation, the y-axis is parallel with wave crests, z is taken to be vertically upwards measured from the mean sea surface (Fig. 2.1), and the tilde sign signifies the variables related with wave motion.

Seeking a plane wave solution to the above model, one finds that

$$\tilde{u} = \frac{\Lambda a \sigma}{k} \frac{\cosh(\Lambda h + \Lambda z)}{\sinh \Lambda h} \cos(kx - \sigma t) \tag{2.7}$$

$$\tilde{v} = \left(\frac{f}{\sigma}\right) \frac{\Lambda a \sigma}{k} \frac{\cosh(\Lambda h + \Lambda z)}{\sinh \Lambda h} \sin(kx - \sigma t) \tag{2.8}$$

$$\tilde{w} = a\sigma\frac{\sinh(\Lambda h + \Lambda z)}{\sinh \Lambda h}\sin(kx - \sigma t) \qquad (2.9)$$

$$\tilde{p} = \rho g a\frac{\cosh(\Lambda h + \Lambda z)}{\cosh \Lambda h}\cos(kx - \sigma t) - \rho g z \qquad (2.10)$$

$$\tilde{\eta} = a\cos(kx - \sigma t) \qquad (2.11)$$

in which k is the wavenumber, $\Lambda = k/\sqrt{1 - (f/\sigma)^2}$ and $\sigma^2 = g\Lambda\tanh\Lambda h$. In Weber's (1990) paper, which gives a comparison of the Eulerian and the Lagrangian approaches for the wave drift problem in a rotating ocean, an Eulerian deep water wave solution is presented. The solution shown above is more general, in which the deep water solution is obtained in the limit when $h \to \infty$. Substitution of realistic numbers for σ and f will make σ^2/f^2, which appears in the expression of Λ, of order $O(10^{-8})$. Therefore, in the following discussion, Λ will be approximated with k.

The significance of the rotating frame to the wave solution is that it introduces a crest parallel wave orbital velocity component, $\tilde{v}$. This component is in phase with its vertical counterpart, $\tilde{w}$. A net wave-induced Reynolds stress then arises from averaging over a wave cycle,

$$-\rho < \tilde{v}\tilde{w} >= -\rho a^2 f\sigma\frac{\sinh 2k(h + z)}{4\sinh^2(kh)}, \qquad (2.12)$$

where the angle bracket denotes time averaging over a wave period. For the hyperbolic functions in Eqs. (2.7) to (2.10), z is defined from $z = 0$ to $z = -h$ instead of from $z = \tilde{\eta}$ to $z = -h$. This involves an assumption that the wave solutions can be analytically extended to the mean sea surface when $\tilde{\eta} < 0$, which is a usual assumption in linear wave theory (e.g., Phillips, 1977, Eqs. 3.1.10 — 11; Hasselmann, 1971, page 192; Weber, 1993a, Eq. 20). Consequently, the derived stress of Eq. (2.12) is also defined from the mean sea level $z = 0$ to the sea bed $z = -h$.

The boundary condition (2.5) implies a flat sea bottom. However, the solutions remain valid for slowly varying topography where the depth changes only slightly over a wavelength of the waves. Eq. (2.12) can therefore be applied to large scale motions, where the topography varies in scales of kilometers, and the depth h can be regarded as $h(x, y)$.

An estimate of the size of this stress may be made by considering the deep water case. In deep water, the stress becomes

$$\rho < \tilde{v}\tilde{w} > = \rho \frac{a^2 f \sigma}{2} e^{2kz}. \tag{2.13}$$

With $f = 10^{-4} s^{-1}$, $\rho = 10^3 kg\ m^{-3}$, $\sigma = 1 s^{-1}$ (about 6 second period), and $a = \sqrt{2}m$ (corresponding only to moderate waves) then the stress has a value of $0.1 Pa$ at the surface. This is comparable in size to a typical wind stress.

Since a surface wave decays vertically, as its name suggests, one can calculate an associated body force by taking a derivative of Eq. (2.12) with respect to the vertical coordinate z. The body force is then

$$
\begin{aligned}
-\rho \frac{\partial < \tilde{v}\tilde{w} >}{\partial z} &= -\rho \frac{a^2 f \sigma}{\delta_{st}} \frac{\cosh 2k(h+z)}{4 \sinh^2(kh)} \\
&= -f \rho q_{st} \tag{2.14}
\end{aligned}
$$

where

$$\delta_{st} = 1/(2k) \tag{2.15}$$

and is known as the Stokes depth (Fig. 1.1). The Stokes velocity, q_{st}, is given by

$$
\begin{aligned}
q_{st} &= \sigma a^2 k \frac{\cosh 2k(h+z)}{2 \sinh^2(kh)} \tag{2.16} \\
&= q_{st}(0) \frac{\cosh 2k(h+z)}{\cosh 2kh} \tag{2.17}
\end{aligned}
$$

where

$$q_{st}(0) = \sigma a^2 k \frac{\cosh 2kh}{2 \sinh^2(kh)} \tag{2.18}$$

represents the surface value of the Stokes drift.

In Eq. (2.17), the depth dependent Stokes drift has been expressed as its surface value times a depth distribution function. It will be shown that the flow driven by wave force can also be expressed in terms of $q_{st}(0)$, where $q_{st}(0)$ can be a time series. In this case, the parenthetical zero might lead to a confusion with a constant value at

the initial time. For this reason, another notation for the surface value of the Stokes drift,

$$\mathfrak{S} = q_{st}(t; z = 0) \tag{2.19}$$

is introduced. In the following discussion, both $q_{st}(0)$ and $\mathfrak{S}$ will be used as appropriate.

2.3 Viscous wave boundary layers

In a non-rotating frame, Longuet-Higgins (1953, 1960) showed that the two thin wave boundary layers have fundamental effects on the wave mass transport in the interior region no matter how small the viscosity. The effects can be expressed as two boundary conditions just beneath a thin free surface boundary layer and just above a thin bottom boundary layer. (These wave boundary layers are of order of millimeter thick in practice, e.g., Russell and Osorio, 1958.) Written in an Eulerian sense, Longuet-Higgins' boundary conditions are

$$\nu \frac{\partial q}{\partial z} = 2\nu k \tanh 2kh q_{st}(0) \qquad \text{at } z = 0 - \delta_w \approx 0 \tag{2.20}$$

$$q = \frac{3}{2} q_{st}(-h) \qquad \text{at } z = -h + \delta_w \approx -h \tag{2.21}$$

where $q_{st}(-h)$ stands for the bottom Stokes drift. The boundary layer thickness $\delta_w = \sqrt{2\nu/\sigma}$, where ν is kinematic viscosity, and σ is wave frequency. Equation (2.20) has been termed wave-induced virtual tangential stress (kinematic), and Eq. (2.21) represents bottom streaming. In the following, the virtual stress will be rederived before it is extended to the rotating frame. The bottom streaming condition will be shown as a part of solutions to the wave driven flow in Chapter 4 (cf. Eqs. 4.13 and 4.21).

2.3.1 Virtual wave stress on the free surface

The free surface boundary condition has drawn considerable discussion (e.g., Phillips, 1977; Longuet-Higgins, 1969b; Huang, 1970; Ünlüata and Mei, 1970; and Weber,

1983a) because of its important role in the transfer of wave energy to the mean flow. However, while it seems sensible there should be a stress, the details of the mechanism are far from obvious. The complexity of the mathematical derivation given by Longuet-Higgins obscures the physics of the generating mechanism. Phillips (1977) offered an explanation from the point of view of wave energy dissipation into the surrounding water. The extension of this energy approach to the rotating system is presented in Appendix B to this chapter. Presented in this section is a succinct and rigorous derivation of Longuet-Higgins' virtual wave stress. It reveals that the virtual stress can be derived by considering the projections on the surface slope of two viscous normal stresses acting on the two axial planes respectively.

Let

$$\Pi = z - a\cos(kx - \sigma t) \tag{2.22}$$

then the free surface is described by

$$\Pi \equiv 0. \tag{2.23}$$

The outward unit normal vector at a point O on the free surface (Fig. 2.2) is

$$\vec{n} = [n_x, \ n_z] = \frac{\nabla\Pi}{|\nabla\Pi|}$$

$$\approx [ka\sin\phi, \ 1 - \frac{1}{2}(ka)^2\sin^2\phi] \qquad (\text{omit } O((ka)^3)) \tag{2.24}$$

where ϕ denotes $kx - \sigma t$. The tangential direction $\vec{s}$ at the point O is

$$\vec{s} = [n_z, \ -n_x]$$

$$= [1 - \frac{1}{2}(ka)^2\sin^2\phi, \ -ka\sin\phi]. \tag{2.25}$$

The tangential stress, P_{ns}, at the point O on the free surface is calculated as follows

$$P_{ns} = n_i P_{ij} s_j \qquad\qquad i = x, z \quad j = x, z$$

$$\approx P_{zx} + ka\sin\phi[P_{xx} - P_{zz}] - 2(ka)^2\sin^2\phi P_{xz} \qquad (\ O((ka)^3)), \tag{2.26}$$

where P_{ij} is a second order symmetric stress tensor (e.g., Batchelor, 1967). On the free surface P_{ns} vanishes, thus from Eq. (2.26)

$$P_{zx} + ka\sin\phi[P_{xx} - P_{zz}] - 2(ka)^2\sin^2\phi P_{xz} = 0. \qquad (2.27)$$

The relationship between a viscous stress tensor and the gradients of velocity are

$$P_{xx} = -p + 2\mu\frac{\partial u}{\partial x} \qquad (2.28)$$

$$P_{zx} = \mu(\frac{\partial u}{\partial z} + \frac{\partial w}{\partial x}) = P_{xz} \qquad (2.29)$$

$$P_{zz} = -p + 2\mu\frac{\partial w}{\partial z}. \qquad (2.30)$$

Assume that

$$u = \varepsilon u_1 + \varepsilon^2 u_2 + \dots \qquad (2.31)$$

$$w = \varepsilon w_1 + \varepsilon^2 w_2 + \dots \qquad (2.32)$$

in which ε is a small parameter. The first order u_1, w_1 correspond to high frequency periodic surface wave motion, with the second and higher orders representing much lower frequency motion. In the problem of wave driven flow, it is common to take the wave slope as the small parameter (e.g., Phillips, 1967, page 24), i.e.,

$$\varepsilon = ka. \qquad (2.33)$$

Accordingly,

$$P_{xx} = -p + (ka)\,2\mu\frac{\partial u_1}{\partial x} + (ka)^2\,2\mu\frac{\partial u_2}{\partial x} + \dots \qquad (2.34)$$

$$P_{xz} = (ka)\,\mu\left(\frac{\partial u_1}{\partial z} + \frac{\partial w_1}{\partial x}\right) + (ka)^2\,\mu\frac{\partial u_2}{\partial z} + \dots$$

$$= P_{zx} \qquad (2.35)$$

$$P_{zz} = -p + (ka)\,2\mu\frac{\partial w_1}{\partial z} + (ka)^2\,\mu\frac{\partial w_2}{\partial z} + \dots \qquad (2.36)$$

where $\partial w_2/\partial x$ has been dropped from P_{zx} because the horizontal scale over which the second order motion varies is much larger than the water depth in the ocean.

Substitution of Eqs. (2.34), (2.35) and (2.36) into Eq. (2.27) yields

$$(ka)\,\mu\left(\frac{\partial u_1}{\partial z}+\frac{\partial w_1}{\partial x}\right)$$

$$+(ka)^2\left[2\mu\sin\phi\left(\frac{\partial u_1}{\partial x}-\frac{\partial w_1}{\partial z}\right)+\mu\frac{\partial u_2}{\partial z}\right]+...=0. \qquad (2.37)$$

For the above equation to hold, the coefficients of each power of (ka) must be equal to zero, giving

$$\mu\left(\frac{\partial u_1}{\partial z}+\frac{\partial w_1}{\partial x}\right) \;=\; 0 \qquad (2.38)$$

$$\left[2\mu\sin\phi\left(\frac{\partial u_1}{\partial x}-\frac{\partial w_1}{\partial z}\right)+\mu\frac{\partial u_2}{\partial z}\right] \;=\; 0 \qquad (2.39)$$

$$......$$

Time averaging Eq. (2.39) yields

$$\mu\left\langle\frac{\partial u_2}{\partial z}\right\rangle \;=\; -2\mu\left\langle\sin\phi\left(\frac{\partial u_1}{\partial x}-\frac{\partial w_1}{\partial z}\right)\right\rangle, \qquad (2.40)$$

while averaging Eq. (2.31) yields

$$<u> \;=\; (ka)^2 <u_2> +O((ka)^3). \qquad (2.41)$$

The combination of Eqs. (2.40) and (2.41) then results in

$$\mu\frac{\partial<u>}{\partial z} \;=\; -(ka)^2\left\langle 2\mu\sin\phi\left(\frac{\partial u_1}{\partial x}-\frac{\partial w_1}{\partial z}\right)\right\rangle \qquad (2.42)$$

where terms of $O((ka)^3)$ have been dropped. This equation reveals the essence of the virtual tangential stress. It is the projection on the surface slope of two viscous normal stresses acting on the two axis planes respectively (Fig. 2.2).

The next question concerns how to calculate the virtual tangential stress if only provided with the inviscid wave solution. This can be done as follows. First, note that

$$\frac{\partial u_1}{\partial x}-\frac{\partial w_1}{\partial z}=2\frac{\partial u_1}{\partial x} \qquad (2.43)$$
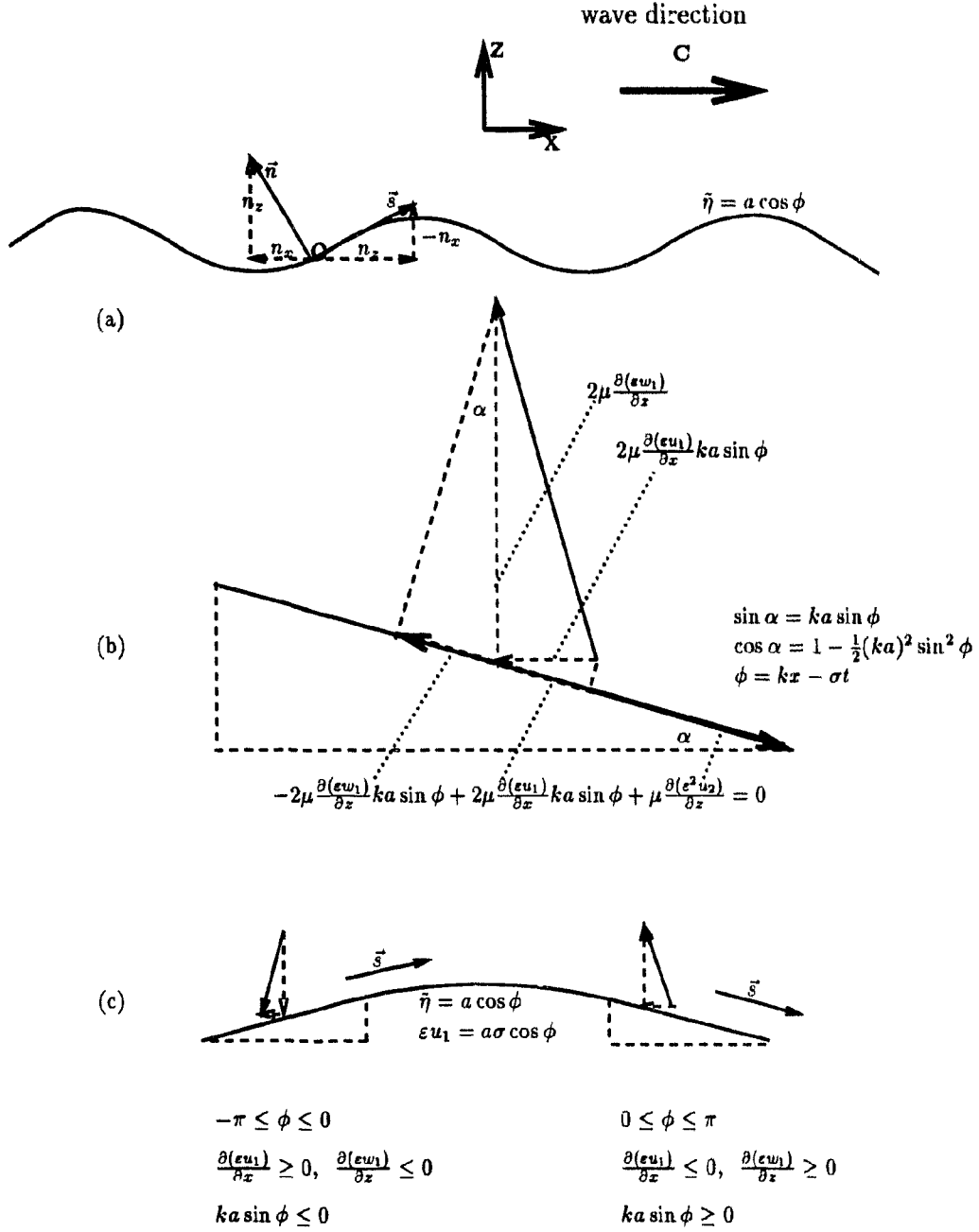
Figure 2.2: (a) Normal and tangential directions on the free surface; (b) Projections on the slope of two viscous normal stresses $2\mu\frac{\partial u_1}{\partial x}ka\sin\theta$ and $2\mu\frac{\partial w_1}{\partial z}$ acting on $x-$ and $z-$planes respectively; (c) The projections are always opposite to the tangential direction, when averaged over a wave cycle they contribute a second order tangential stress, $\mu\frac{\partial(\epsilon^2 u_2)}{\partial z}$, as is required by zero total tangential stress on the surface. In the figure, $\epsilon = ka$ and they have been used interchangeably.

because of the incompres.'bility of the fluid. Second, define two components in u_1 near the free surface. One is the inviscid solution, say $u_{1\,invis}$, and the other is viscid solution, say $u_{1\,vis}$. Although details about $u_{1\,vis}$ are not known, one thing about it is certain, $u_{1\,vis} = O(k/\beta)u_{1\,invis}$, ($\beta = \delta_w^{-1} = \sqrt{\sigma/(2\nu)}$ is the thickness of the surface viscous boundary layer). This follows since on the free surface the shear stress due to the inviscid motion must be balanced by that due to the viscid motion. Because of the high frequency of the first order motion, the thickness of the viscous boundary layer is much smaller than the wave length, i.e.,

$$\frac{k}{\beta} \ll 1. \tag{2.44}$$

Thus one can calculate the virtual stress using only the inviscid solution

$$
\begin{aligned}
\frac{\partial u_1}{\partial x} - \frac{\partial w_1}{\partial z} &= 2\frac{\partial u_1}{\partial x} \\
&= 2\frac{\partial u_{1\,invis}}{\partial x}\left[1 + O(\frac{k}{\beta})\right].
\end{aligned}
\tag{2.45}
$$

Substitution of Eq. (2.45) into Eq. (2.42) yields

$$\mu\frac{\partial <u>}{\partial z} = -4\mu(ka)^2\left\langle \sin\phi\frac{\partial u_{1\,invis}}{\partial x}\right\rangle \qquad (\text{omit } O((ka)^2\tfrac{k}{\beta})). \tag{2.46}$$

The inviscid solution to the surface gravity wave motion in non-rotating shallow water is (e.g., Phillips, 1977)

$$
\begin{aligned}
u_{invis} &= (ka)\frac{g}{\sigma}\frac{\cosh(kh+kz)}{\cosh kh}\cos\phi \\
&= (ka)u_{1\,invis}.
\end{aligned}
\tag{2.47}
$$

Furthermore substituting

$$u_{1\,invis} = \frac{g}{\sigma}\frac{\cosh(kh+kz)}{\cosh kh}\cos\phi \tag{2.48}$$

into Eq. (2.46) results in

$$\tilde{\tau}_x = \nu\frac{\partial <u>}{\partial z}\bigg|_{z=0} = 2\nu(ka)^2\sigma\coth kh \tag{2.49}$$

where the dynamic stress has been converted to a kinematic one (for convenience in later use) and the dispersion relationship $\sigma^2 = gk\tanh(kh)$ has been used. Upon using Eq. (2.16), the above formula for the virtual wave stress is equivalent to Eq. (2.20).

When the earth's rotation is taken into account, there will be a velocity component parallel to the wave crest as is shown in Section 2.2. Consequently the tensor P_{ij} will become three dimensional ($i = x, y, z$, $j = x, y, z$). However if the wave profile is unchanged along the direction of the crest as is assumed in Section 2.2, the unit normal direction of the free surface is

$$\vec{n} = [ka\sin\phi, \ 0, \ 1 - \frac{1}{2}(ka)^2\sin^2\phi] \tag{2.50}$$

and the unit tangential direction is

$$\vec{s} = [1 - \frac{1}{2}(ka)^2\sin^2\phi, \ 0, \ -ka\sin\phi]. \tag{2.51}$$

Since both n_y and s_y are zero, neither P_{iy} nor P_{yj} can make contributions to the tangential stress on the surface, whose formula is

$$P_{ns} = n_i P_{ij} s_j \qquad (i = x, y, z, \ j = x, y, z). \tag{2.52}$$

Thus Eq. (2.46) remains formally valid. Substituting Eq. (2.7) into Eq. (2.46) yields the same value for the virtual stress as is given by Eq. (2.49).

It should be noted that the above derivation of the virtual stress does not demand any particular type of viscosity or its depth structure. The "viscosity", ν, introduced into the derivation in the relations between the stress and the velocity gradient, Eqs. (2.28), (2.29) and (2.30) holds regardless of whether flow is laminar or turbulent. Thus the virtual stress should be applicable to both flows. The only difference will be in the value of the virtual stress. As Longuet-Higgins (1969b) states, *"... if the laminar motion breaks down, as it probably will, the damping of the short waves may be greatly increased, leading to a corresponding increase in the virtual wave stress."*

An estimate of the size of the virtual tangential stress can be made by using the fact that the amplitudes of sea waves are given by

$$\frac{1}{2}a^2 = S(\sigma)d\sigma \tag{2.53}$$

in which $S(\sigma)$ is a wave energy spectrum. For the deep water case, $\coth kh$ in Eq. (2.49) tends to one, and substitution of Eq. (2.53) into Eq. (2.49), using the deep water dispersion relationship, results in

$$\tilde{\tau}_x = \frac{4\nu}{g^2} \int_0^\infty \sigma^5 S(\sigma)d\sigma. \tag{2.54}$$

Therefore, the virtual stress is the fifth moment of the energy spectrum, and the estimate of the virtual stress is entirely determined by the choices of ν and the form of the spectrum $S(\sigma)$. The following two references give examples for the estimation of virtual stress.

Longuet-Higgins (1969b) chose ν as the molecular viscosity and the spectrum as

$$S(\sigma) = 1.2 \times 10^{-2} g^2 \sigma^{-5} \qquad (\sigma_{min} < \sigma < \sigma_{max}) \tag{2.55}$$

where the upper limit frequency σ_{max} relates to the wind speed. He obtained

$$\tilde{\tau}_x = 4.8 \times 10^{-2} \nu \sigma_{max} \tag{2.56}$$

when $\sigma_{max} \gg \sigma_{min}$. Based on Cox's (1958) wind tunnel data, he showed that the ratio of the virtual wave stress to the wind stress decreases from 13% to 3% for wind speed increases from $3.18 ms^{-1}$ to $12.02 ms^{-1}$. As pointed out by Longuet-Higgins, this result assumes laminar motion; when laminar motion breaks down, the proportion of the virtual wave stress should be higher.

Madsen (1978) used the Pierson-Moskowitz (1964) spectrum and a wind velocity related eddy viscosity to estimate the size of the surface velocity induced by the virtual wave stress in deep water. The size of the surface flow driven by the virtual stress he found, is on the same order as that driven purely by the wind.

2.3.2 Wave stress due to bottom friction

Generation of bottom streaming (Longuet-Higgins, 1953) in a non-rotating frame was explained by Longuet-Higgins (1958). Due to the existence of bottom friction, the two wave orbital velocities, $\tilde{u}$ and $\tilde{w}$, are slightly in phase, resulting in a net Reynolds stress, $< \tilde{u}\tilde{w} >$; this stress in turn drives the bottom streaming (also see Phillips 1977). Longuet-Higgins (1958) also showed that the magnitude of the bottom streaming is not dependent on the viscosity structure inside the wave bottom friction layer provided that the viscosity is constant in time. A more general approach in which the eddy viscosity varies both with time and distance from the bottom was proposed by Trowbridge and Madsen (1984a, b).

The bottom streaming condition with rotation and viscous effects included has not been addressed previously, mostly because attention to the rotating case has been focused on infinitely deep water. In a rotating frame, there will be another bottom friction layer which is of order $O(\delta_e)$, $\delta_e = \sqrt{2\nu/f}$. Since the wave bottom friction layer is much thinner than the Ekman layer due to $\sigma \gg f$, the Ekman veering effect within this thin layer will be insignificant. In other words, it would be expected that the introduction of the Coriolis force would have little effect on the wave stress within the thin wave boundary. The following detailed analysis confirms this expectation.

To examine the bottom wave stress in a rotating coordinate frame, one needs a solution for the primary wave motion of the real fluid near the bottom. To simplify the problem, Longuet-Higgins' (1953) approach will be followed and a constant viscosity will be assumed. However, if both the Coriolis force and the vertical frictional force are retained in the momentum equations, the problem is still formidable. From the inviscid solution, it is known that the wave crest parallel velocity component, $\tilde{v}$, is proportional to f/σ. Hence the Coriolis term in the x-momentum equation can be dropped since it is of negligible order $O(f^2/\sigma^2)$. These simplifications allow use of

the following equations first

$$
\left.
\begin{array}{rcl}
\frac{\partial \tilde{u}}{\partial t} & = & -\frac{1}{\rho}\frac{\partial \tilde{p}}{\partial x} + \nu \frac{\partial^2 \tilde{u}}{\partial z^2} \\[2mm]
\frac{\partial \tilde{w}}{\partial t} + g & = & -\frac{1}{\rho}\frac{\partial \tilde{p}}{\partial z} + \nu \frac{\partial^2 \tilde{w}}{\partial z^2} \\[2mm]
\frac{\partial \tilde{u}}{\partial x} + \frac{\partial \tilde{w}}{\partial z} & = & 0
\end{array}
\right\}
\tag{2.57}
$$

and then separately consider the solution for the $\tilde{v}$ component,

$$
\frac{\partial \tilde{v}}{\partial t} + f\tilde{u} = \nu \frac{\partial^2 \tilde{v}}{\partial z^2}.
\tag{2.58}
$$

The solution of Eq. (2.57), under the non-slip bottom condition and the matching condition with the inviscid solution in the interior region, is straightforward (Phillips 1977), yielding

$$
\tilde{u} = a\sigma \frac{\cosh kz'}{\sinh kh}\cos(kx - \sigma t) - a\sigma \frac{e^{-\beta z'}}{\sinh kh}\cos(kx - \sigma t + \beta z')
\tag{2.59}
$$

$$
\begin{aligned}
\tilde{w} = {} & a\sigma \frac{\sinh kz'}{\sinh kh}\sin(kx - \sigma t) \\
& + \frac{a\sigma}{2}\left(\frac{k}{\beta}\right)\frac{1}{\sinh kh}\left[e^{-\beta z'}\cos(kx - \sigma t + \beta z') + e^{-\beta z'}\sin(kx - \sigma t + \beta z') \right. \\
& \left. - \cos(kx - \sigma t) - \sin(kx - \sigma t) \right].
\end{aligned}
\tag{2.60}
$$

The solution for $\tilde{v}$ in Eq. (2.58) is obtained as

$$
\begin{aligned}
\tilde{v} = {} & \left(\frac{f}{\sigma}\right)a\sigma \frac{\cosh kz'}{\sinh kh}\sin(kx - \sigma t) \\
& - \left(\frac{f}{\sigma}\right)a\sigma \frac{e^{-\beta z'}}{\sinh kh}\left[\sin(kx - \sigma t + \beta z') - \frac{1}{2}\beta z'\cos(kx - \sigma t + \beta z') \right. \\
& \left. + \frac{1}{2}\beta z'\sin(kx - \sigma t + \beta z') \right]
\end{aligned}
\tag{2.61}
$$

where the notation

$$
z' = z + h
\tag{2.62}
$$

$$
\beta = \sqrt{\frac{\sigma}{2\nu}}
\tag{2.63}
$$

has been used and the terms of order $O(k^2/\beta^2)$ neglected. From Eqs. (2.59) to (2.61), the wave Reynolds stresses (the kinematic ones) in the $x-$ and $y-$ directions are

$$< \tilde{u}\tilde{w} > = \left(\frac{k}{\beta}\right) \frac{(a\sigma)^2}{4\sinh^2 kh} \left[2\beta z' e^{-\beta z'}\sin\beta z' + 2e^{-\beta z'}\cos\beta z' - 1 - e^{-2\beta z'}\right] (2.64)$$

$$< \tilde{v}\tilde{w} > = \left(\frac{f}{\sigma}\right) \frac{(a\sigma)^2}{4\sinh^2 kh} \sinh 2kz'$$
$$- \left(\frac{f}{\sigma}\right) \frac{(a\sigma)^2}{4\sinh^2 kh} e^{-\beta z'}\sinh kz' \left[2\cos\beta z' + \beta z'\sin\beta z' + \beta z'\cos\beta z'\right]$$
$$+ \left(\frac{f}{\sigma}\right)\left(\frac{k}{\beta}\right)\frac{(a\sigma)^2}{4\sinh^2 kh}\left[2e^{-\beta z'}\cos\beta z' - 1 - e^{-2\beta z'}\right.$$
$$\left. +\beta z' e^{-\beta z'}\sin\beta z'\right].\qquad (2.65)$$

The ratio of k to β can be expressed as

$$\frac{k}{\beta} = \frac{\sqrt{2\nu}}{g}\sigma^{3/2}\coth kh \qquad (2.66)$$

where the dispersion relationship $\sigma^2 = gk\tanh kh$ for the surface wave has been used. Typically σ is of order $1\ s^{-1}$ and the water depth h is not so shallow that $\coth kh$ is much larger than 1. The ratio of k/β then depends mainly on the choice of viscosity ν. Typical values of ν for water ranges from $10^{-6}m^2s^{-1}$ for molecular viscosity, to $10^{-2}m^2s^{-1}$ for turbulent viscosity. Accordingly, $k/\beta = O(10^{-4}) \sim O(10^{-2})$. Thus the ratio is a small number even for the turbulent conditions.

Equation (2.64) is the same as that given by Phillips (1977). What is added by the earth's rotation to the wave stress near the bottom is a stress perpendicular to the wave propagating direction, $< \tilde{v}\tilde{w} >$, as is described by Eq. (2.65). However, within the bottom wave boundary layer, since

$$\sinh kz' \approx kz' = \frac{k}{\beta}\beta z', \qquad (2.67)$$

all three terms on RHS of Eq. (2.65) are of order

$$O\left(\frac{f}{\sigma}\frac{k}{\beta}\right). \qquad (2.68)$$

This means that $< \tilde{v}\tilde{w} >$ can be entirely neglected compared with $< \tilde{u}\tilde{w} >$. Therefore, the earth's rotation does little to change the near-bottom stress distribution compared to that in a non-rotating system (Longuet-Higgins 1953, 1958; Phillips 1977). Outside the wave boundary layer, when the term of $O\left(\frac{f}{\sigma}\frac{k}{\beta}\right)$ is neglected, Eq. (2.65) becomes

$$< \tilde{v}\tilde{w} > = \frac{f}{\sigma}\frac{(a\sigma)^2}{4\sinh^2 kh}\sinh 2kz'$$

(2.69)

which is the same as the interior stress given by Eq. (2.12), as should be the case.

2.4 Summary

From the above discussion, a picture of the vertical distribution of wave forcing can be gained. On the free surface, there is a wave-induced virtual tangential stress in the direction of wave propagation. In the interior region, there is a Coriolis-induced wave stress, whose distribution is concentrated mainly within a Stokes depth and is directed $\pi/2$ to the right (left) of the wave propagation direction in the northern (southern) hemisphere. At the bottom there is a wave stress in the same direction as the wave propagation, arising from the phase shift of orbital velocities in the bottom wave boundary layer.

In the course of validating Longuet-Higgins' virtual tangential stress in the rotating system, a succinct and rigorous rederivation of the stress was found. The virtual tangential stress is composed of the projections on the surface slope of the two viscous normal stresses acting on $x-$ and $z-$ planes respectively.

A complex wave-induced body force can now be written as

$$-\frac{\partial}{\partial z}[< \tilde{u}\tilde{w} > + i < \tilde{v}\tilde{w} >] = -q_{st}(0)\left[\frac{\psi(z)}{\cosh 2kh} + if\frac{\cosh 2k(h+z)}{\cosh 2kh}\right]$$

(2.70)

where Eqs. (2.64) and (2.69) have been used, $i = \sqrt{-1}$, and function $\psi(z)$ is

$$\psi(z) = \frac{\sigma}{2\beta}\frac{\partial}{\partial z}\left(2\beta z'e^{-\beta z'}\sin\beta z' + 2e^{-\beta z'}\cos\beta z' - 1 - e^{-2\beta z'}\right)$$

(2.71)

which describes the vertical distribution of the part of wave stress introduced by bottom friction, and is responsible for the bottom streaming of Eq. (2.21) as will be shown in Chapter 4 (cf. Eqs. 4.13 and 4.21).

In the above, it has been assumed for simplicity that the wave propagation direction coincides with positive x—direction, and q_{st} has been described by Eq. (2.16). If the wave direction is at an arbitrary angle θ with respect to the x—axis (Fig. 2.1), then a directional factor $e^{i\theta}$ should be introduced to the Stokes drift expression (see Appendix A to this chapter), i.e.,

$$q_{st} = \sigma a^2 k \frac{\cosh 2k(h+z)}{2\sinh^2(kh)} e^{i\theta}, \tag{2.72}$$

and

$$q_{st}(0) = \sigma a^2 k \frac{\cosh 2kh}{2\sinh^2(kh)} e^{i\theta}, \tag{2.73}$$

in which k is now the wave number in the direction of θ. The virtual wave stress (kinematic) still keeps the same form as Eq. (2.20)

$$\tilde{\tau} = 2\nu k \tanh(2kh) q_{st}(0) \tag{2.74}$$

since the direction factor $e^{i\theta}$ is now absorbed by $q_{st}(0)$.

2.5 Appendix A: Case of wave propagation at arbitrary angles relative to the x-axis

For simplicity, all the derivations presented above assume that the plane wave propagating direction is coincident with the x-axis. With a little more algebra, this restriction can be relaxed. Eqs. (2.1) to (2.6) should first be generalized to allow for the pressure gradient term in the y-direction,

$$\frac{\partial \tilde{u}}{\partial t} - f\tilde{v} = -\frac{\partial \tilde{p}}{\partial x} \tag{2.75}$$

$$\frac{\partial \tilde{v}}{\partial t} + f\tilde{u} = -\frac{\partial \tilde{p}}{\partial y} \tag{2.76}$$

$$\frac{\partial \tilde{w}}{\partial t} + g = -\frac{\partial \tilde{w}}{\partial z} \tag{2.77}$$

$$\frac{\partial \tilde{u}}{\partial x} + \frac{\partial \tilde{v}}{\partial y} + \frac{\partial \tilde{w}}{\partial z} = 0 \tag{2.78}$$

with the same boundary conditions as Eqs. (2.5) and (2.6). Then, seeking the plane wave solution of the form of $\sim e^{i(k_x x + k_y y - \sigma t)}$ where k_x and k_y are the wave number vector components in the x- and the y-directions respectively, one finds that

$$
\begin{aligned}
\tilde{u} = a\sigma \frac{\cosh(\Lambda h + \Lambda z)}{\sinh(\Lambda h)} &[\cos\theta \cos(k_x x + k_y y - \sigma t) \\
&- \frac{f}{\sigma}\sin\theta \sin(k_x x + k_y y - \sigma t)]
\end{aligned} \tag{2.79}
$$

$$
\begin{aligned}
\tilde{v} = a\sigma \frac{\cosh(\Lambda h + \Lambda z)}{\sinh(\Lambda h)} &[\sin\theta \cos(k_x x + k_y y - \sigma t) \\
&+ \frac{f}{\sigma}\cos\theta \sin(k_x x + k_y y - \sigma t)]
\end{aligned} \tag{2.80}
$$

$$\tilde{w} = a\sigma \frac{\sinh(\Lambda h + \Lambda z)}{\sinh(\Lambda h)} \sin(k_x x + k_y y - \sigma t) \tag{2.81}$$

$$\tilde{p} = \rho g a \frac{\cosh(\Lambda h + \Lambda z)}{\cosh(\Lambda h)} \cos(k_x x + k_y y - \sigma t) - \rho g z \tag{2.82}$$

$$\tilde{\eta} = a \cos(k_x x + k_y y - \sigma t) \tag{2.83}$$

where

$$
\begin{aligned}
\Lambda &= \sqrt{\frac{k_x^2 + k_y^2}{(1 - \frac{f^2}{\sigma^2})}} \\
&\approx \sqrt{k_x^2 + k_y^2} = k
\end{aligned} \tag{2.84}
$$

$$\sigma^2 = g\Lambda \tanh(\Lambda h) \tag{2.85}$$

$$\theta = \cos^{-1} \frac{k_x}{\sqrt{k_x^2 + k_y^2}}. \tag{2.86}$$

θ is the wave propagation direction with respect to x-axis and k is the wave number in the direction of θ.

Now, the two horizontal orbital velocity components both have parts in phase with the vertical orbital velocity component. If averaged over the wave period, then

the product of the in-phase components will have non-zero value:

$$< \tilde{u}\tilde{w} > = -a^2 f\sigma \frac{\sinh 2k(h+z)}{4\sinh^2(kh)} \sin\theta \tag{2.87}$$

$$< \tilde{v}\tilde{w} > = a^2 f\sigma \frac{\sinh 2k(h+z)}{4\sinh^2(kh)} \cos\theta. \tag{2.88}$$

Written on a complex plane, they can be merged as

$$< \tilde{u}\tilde{w} > +i < \tilde{v}\tilde{w} > = i f a^2 \sigma \frac{\sinh 2k(h+z)}{4\sinh^2(kh)} e^{i\theta}. \tag{2.89}$$

The associated body force is

$$\frac{\partial}{\partial z}(< \tilde{u}\tilde{w} > +i < \tilde{v}\tilde{w} >) = i f a^2 \sigma k \frac{\cosh 2k(h+z)}{2\sinh^2(kh)} e^{i\theta}$$

$$= i f q_{st} \tag{2.90}$$

where q_{st} is the Stokes drift

$$q_{st} = a^2 \sigma k \frac{\cosh 2k(h+z)}{2\sinh^2(kh)} e^{i\theta}. \tag{2.91}$$

2.6 Appendix B: Wave energy dissipation and virtual tangential stress in the rotating system

This appendix extends Phillips' wave energy dissipation approach to examine Longuet-Higgins virtual tangential stress in the rotating system. Since the viscous effects near the boundary are of particularly concern here, vertical shear (kinematic) stresses, $\partial\tau_{xz}/\partial z$ and $\partial\tau_{yz}/\partial z$ are introduced into the x- and y-momentum equation as

$$\frac{\partial \tilde{u}}{\partial t} - f\tilde{v} = -g\frac{\partial \tilde{\eta}}{\partial x} + \frac{\partial \tau_{xz}}{\partial z} \tag{2.92}$$

$$\frac{\partial \tilde{v}}{\partial t} + f\tilde{u} = -g\frac{\partial \tilde{\eta}}{\partial y} + \frac{\partial \tau_{yz}}{\partial z}. \tag{2.93}$$

Integrating the above equation from $z = 0$ to $z = \tilde{\eta}$ and then averaging results in

$$\frac{\partial < \tilde{u}\tilde{\eta} >}{\partial t} - < \tilde{u}\tilde{w} > -f < \tilde{v}\tilde{\eta} > = - < \tau_{xz} > \qquad \text{at } z = 0 \tag{2.94}$$

$$\frac{\partial < \tilde{v}\tilde{\eta} >}{\partial t} - < \tilde{v}\tilde{w} > +f < \tilde{u}\tilde{\eta} > = - < \tau_{yz} > \qquad \text{at } z = 0 \tag{2.95}$$

where the following have been used:

•

$$< \int_0^{\tilde{\eta}} \frac{\partial \tilde{u}}{\partial t} dz > \; \approx \; < \tilde{\eta} \frac{\partial \tilde{u}}{\partial t} > \Big|_{z=0}$$

$$= \; \frac{\partial < \tilde{u}\tilde{\eta} >}{\partial t} - < \tilde{u}\frac{\partial \tilde{\eta}}{\partial t} > \qquad z = 0$$

$$= \; \frac{\partial < \tilde{u}\tilde{\eta} >}{\partial t} - < \tilde{u}\tilde{w} > \qquad z = 0. \qquad (2.96)$$

Similarly,

$$< \int_0^{\tilde{\eta}} \frac{\partial \tilde{v}}{\partial t} dz > \; \approx \; \frac{\partial < \tilde{v}\tilde{\eta} >}{\partial t} - < \tilde{v}\tilde{w} >, \qquad z = 0. \qquad (2.97)$$

•

$$< \int_0^{\tilde{\eta}} f\tilde{v} dz > \; \approx \; f < \tilde{v}\tilde{\eta} > \qquad \text{at } z = 0 \qquad (2.98)$$

$$< \int_0^{\tilde{\eta}} f\tilde{u} dz > \; \approx \; f < \tilde{u}\tilde{\eta} > \qquad \text{at } z = 0. \qquad (2.99)$$

• There is no horizontal variation[1] in wave amplitude so that $< \frac{1}{2}g\partial\tilde{\eta}^2/\partial x > = 0$ and $< \frac{1}{2}g\partial\tilde{\eta}^2/\partial y > = 0$

• $\tau_{xz} = 0$ at the real surface ($z = \tilde{\eta}$).

From Eqs. (2.79) to (2.83), one can verify that

$$f < \tilde{u}\tilde{\eta} > - < \tilde{w}\tilde{v} > \; = \; 0 \qquad z = 0 \qquad (2.100)$$

$$f < \tilde{v}\tilde{\eta} > + < \tilde{w}\tilde{u} > \; = \; 0 \qquad z = 0. \qquad (2.101)$$

Thus Eqs. (2.94) and (2.95) are reduced to

$$\frac{\partial < \tilde{u}\tilde{\eta} >}{\partial t} \; = \; - < \tau_{xz} > \qquad z = 0 \qquad (2.102)$$

$$\frac{\partial < \tilde{v}\tilde{\eta} >}{\partial t} \; = \; - < \tau_{yz} > \qquad z = 0. \qquad (2.103)$$

---

[1]This assumption is made to simplify the discussion. The classical wave radiation stress (Longuet-Higgins and Steward, 1964) will take care of the term $< 1/2g\partial\tilde{\eta}^2/\partial x >$ and $< 1/2g\partial\tilde{\eta}^2/\partial y >$, if there is horizontal gradient in the wave amplitude.

From Eqs. (2.79) to (2.83), one can calculate the total wave energy per unit area below the plane $z = 0$, denoted as E, to be

$$E = (2k)^{-1}\rho a^2 \sigma^2 \coth kh \tag{2.104}$$

where the high order terms of $O(f^2/\sigma^2)$ have been neglected. From Eqs. (2.79) to (2.83), one can also verify that

$$< \tilde{u}\tilde{\eta} > |_{z=0} = \frac{k}{\rho\sigma}E\cos\theta \tag{2.105}$$

$$< \tilde{v}\tilde{\eta} > |_{z=0} = \frac{k}{\rho\sigma}E\sin\theta \tag{2.106}$$

whereby

$$\frac{\partial < \tilde{u}\tilde{\eta} >}{\partial t}\Big|_{z=0} = \frac{k}{\rho\sigma}\frac{\partial E}{\partial t}\cos\theta \tag{2.107}$$

$$\frac{\partial < \tilde{v}\tilde{\eta} >}{\partial t}\Big|_{z=0} = \frac{k}{\rho\sigma}\frac{\partial E}{\partial t}\sin\theta. \tag{2.108}$$

For the plane wave in question the energy dissipation rate per unit area is given by

$$\frac{\partial E}{\partial t} = -2\mu\int_{-h}^{0} e_{ij}e_{ji}dz \tag{2.109}$$

(e.g., Phillips, 1967, eqs. (2.3.4) and (3.4.13)) where e_{ij} is a symmetric tensor

$$e_{ij} = \frac{1}{2}\left(\frac{\partial \tilde{u}_i}{\partial x_j} + \frac{\partial \tilde{v}_j}{\partial x_i}\right) \tag{2.110}$$

where the correspondence of $\tilde{u}_i$ to $\tilde{u}$, $\tilde{v}$ or $\tilde{w}$ and x_i to x, y or z when $i = 1, 2, 3$ is conventional. Substituting Eq. (2.79) to Eq. (2.81) into the above expression yields

$$\frac{\partial E}{\partial t} = -2\mu a^2\sigma^2 k \coth kh. \tag{2.111}$$

Thus, combination of Eqs. (2.102), (2.103), (2.107), (2.108), and (2.111) results in

$$< \tau_{xz} > = -\frac{\partial < \tilde{u}\tilde{\eta} >}{\partial t} = -\frac{k}{\rho\sigma}\frac{\partial E}{\partial t}\cos\theta$$

$$= 2\mu\sigma k^2 a^2\cos\theta\coth kh \equiv \tilde{\tau}_x, \qquad z = 0 \tag{2.112}$$

$$< \tau_{yz} > = -\frac{\partial < \tilde{v}\tilde{\eta} >}{\partial t} = -\frac{k}{\rho\sigma}\frac{\partial E}{\partial t}\sin\theta$$

$$= 2\mu\sigma k^2 a^2\sin\theta\coth kh \equiv \tilde{\tau}_y, \qquad z = 0 \tag{2.113}$$

where notations $\tilde{\tau}_x$ and $\tilde{\tau}_y$ signify that these mean stresses are related to waves. A second order motion then is set up on $z = 0$ to balance these shear stresses, i.e.,

$$\nu\frac{\partial <u>}{\partial z} \;=\; 2\nu\sigma k^2 a^2 \cos\theta \coth kh \qquad z = 0 \qquad\qquad (2.114)$$

$$\nu\frac{\partial <v>}{\partial z} \;=\; 2\nu\sigma k^2 a^2 \sin\theta \coth kh \qquad z = 0 \qquad\qquad (2.115)$$

or written in the complex plane as

$$\tilde{\tau} \;=\; \tau_{xz} + i\tau_{yz} = 2\nu\sigma k^2 a^2 e^{i\theta} \coth kh \qquad\qquad (2.116)$$

$$\;=\; 2\nu k \tanh(2kh) q_{st}(0) \qquad\qquad \text{at } z = 0. \qquad\qquad (2.117)$$

Chapter 3

Governing Equations With Mean Wave Forcing

3.1 Introduction

The mean effects of short surface gravity waves on the flow have been accounted for in the equations of motion either in a depth averaged 2D sense or in a 3D sense. The depth averaged approach appears in textbooks (e.g., Phillips 1977; LeBlond and Mysak 1978), and the depth dependent approach can be found in research papers (e.g., Hasselmann 1971, Svendsen 1989). However, in these treatments the Coriolis induced wave stresses are not included. This chapter therefore will first derive a set of equations in three dimensions which includes wave forces. A linearized set of equations with assumed horizontal homogeneity in wave forcing is then introduced to obtain a simple Eulerian model which includes Coriolis-induced wave forcing and the virtual wave stress in addition to the traditional wind stress. Finally, a relationship between the responses of an Eulerian water column to the step function (in time) forcing and to arbitrary forcing is presented.

3.2 General Eulerian governing equations accounting for forcing by short surface gravity waves

In an x-y-z Cartesian frame rotating with angular frequency $f/2$, the general equations governing geophysical flow are (e.g., Pedlosky 1979, Section 1.4 and 1.6; Csanady, 1982, Section 1.2)

$$\left. \begin{array}{l} \frac{\partial u}{\partial t} + \frac{\partial(uu)}{\partial x} + \frac{\partial(uv)}{\partial y} + \frac{\partial(uw)}{\partial z} - fv = -\frac{1}{\rho}\frac{\partial p}{\partial x} \\[4pt] \frac{\partial v}{\partial t} + \frac{\partial(uv)}{\partial x} + \frac{\partial(vv)}{\partial y} + \frac{\partial(vw)}{\partial z} + fu = -\frac{1}{\rho}\frac{\partial p}{\partial y} \\[4pt] \frac{\partial w}{\partial t} + \frac{\partial(uw)}{\partial x} + \frac{\partial(vw)}{\partial y} + \frac{\partial(ww)}{\partial z} + g = -\frac{1}{\rho}\frac{\partial p}{\partial z} \\[4pt] \frac{\partial u}{\partial x} + \frac{\partial v}{\partial y} + \frac{\partial w}{\partial z} = 0 \end{array} \right\} \tag{3.1}$$

where the molecular viscosity has been neglected. In a highly turbulent environment, like the ocean, the Reynolds' stresses will dominate over the molecular viscosity as a dissipative mechanism. When short surface gravity waves are present, velocity can be partitioned into three parts,

$$u_i = <u_i> + \tilde{u}_i + u_i' \tag{3.2}$$

where the correspondence of u_i to u, v or w when $i = 1, 2, 3$ is conventional. The diagonal bracket indicates a slowly varying component, the tilde sign a wave component, and the prime a turbulent component. The diagonal bracket also represents time-averaging over a duration much longer than both wave group and turbulent time scales, but still significantly shorter than time scales associated with slow motions such as tides and wind-driven circulations. Such an averaging period is assumed to average out both the waves and the turbulent components, i.e.,

$$<\tilde{u}_i> = <u_i'> = 0. \tag{3.3}$$

The three components are assumed to be uncorrelated (e.g. Longuet-Higgins and Stewart 1960, 1961; DeVriend and Stive 1987; Svendsen 1989), so that

$$<u_i u_j> = <u_i><u_j> + <\tilde{u}_i\tilde{u}_j> + <u_i'u_j'> . \tag{3.4}$$

This concept of velocity decomposition and time averaging may be justified by the presence of frequency gaps between the short surface gravity waves and long time scale motions as shown in Fig. (3.1), cited from LeBlond and Mysak (1978).

For long time scale motions, surface waves and turbulence are merely fluctuations and of major interest are their time averaged effects. Turbulence brings fluctuations to the velocities, while surface waves bring fluctuations not only to velocities but also to the free surface. Therefore if one simply applies time averaging to the Eqs. (3.1) (in the way the Reynolds stresses are generally obtained) then no information about the free surface will be picked up. If one integrates Eq. (3.1) from the sea bottom to the free surface in order to pick up information from the surface, and then applies time averaging on the depth-integrated equations (in the way the radiation stresses are derived, Longuet-Higgins and Stewart,1960; Longuet-Higgins,1964), then the vertical structure of the currents will be lost.

To resolve this dilemma, the water column needs to be divided into two layers: a thin top wave boundary layer over a main interior layer. In the interior layer, time-averaging can be directly applied to Eq. (3.1) since there are no surface fluctuations to contend with. For the top wave layer, vertical integration of Eqs. (3.1) from the bottom of the layer (or the top of the interior layer) to the free surface will be first carried out, followed by time averaging the integrated equations to derive the boundary condition for the main layer by matching the fluxes of mass and momentum across the interface between the two layers.
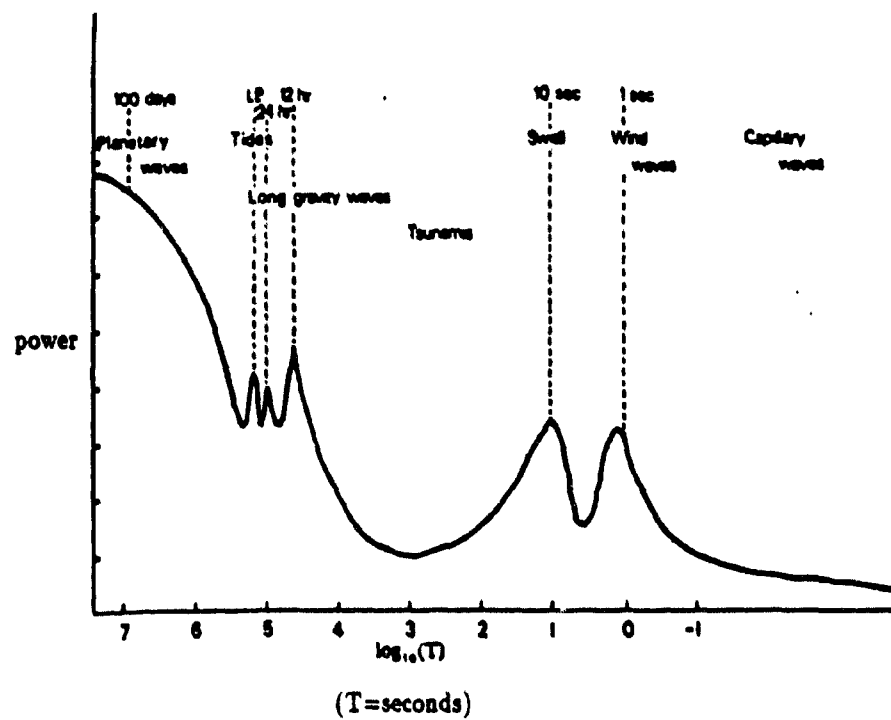
Figure 3.1: This figure, (from LeBlond and Mysak 1978), indicates there may be frequency gaps between the sea waves (swells and wind waves) and long time scale motions (tides and wind-driven flows etc.).

3.2.1 Governing equations for water motion in the interior region

In the fluid interior, beneath the surface boundary layer, direct application of the time-averaging of Eq. (3.1) yields

$$
\begin{aligned}
\frac{D<u>}{Dt} - f <v> + \frac{1}{\rho}\frac{\partial<p>}{\partial x} &= \frac{\partial}{\partial x}\left(\nu_h\frac{\partial<u>}{\partial x}\right) + \frac{\partial}{\partial y}\left(\nu_h\frac{\partial<u>}{\partial y}\right) + \frac{\partial}{\partial z}\left(\nu\frac{\partial<u>}{\partial z}\right) \\
&\quad - \frac{\partial<\tilde{u}\tilde{u}>}{\partial x} - \frac{\partial<\tilde{u}\tilde{v}>}{\partial y} - \frac{\partial<\tilde{u}\tilde{w}>}{\partial z} \\[2mm]
\frac{D<v>}{Dt} + f <u> + \frac{1}{\rho}\frac{\partial<p>}{\partial y} &= \frac{\partial}{\partial x}\left(\nu_h\frac{\partial<v>}{\partial x}\right) + \frac{\partial}{\partial y}\left(\nu_h\frac{\partial<v>}{\partial y}\right) + \frac{\partial}{\partial z}\left(\nu\frac{\partial<v>}{\partial z}\right) \\
&\quad - \frac{\partial<\tilde{v}\tilde{u}>}{\partial x} - \frac{\partial<\tilde{v}\tilde{v}>}{\partial y} - \frac{\partial<\tilde{v}\tilde{w}>}{\partial z} \\[2mm]
\frac{1}{\rho}\frac{\partial<p>}{\partial z} &= -g - \frac{\partial<\tilde{w}\tilde{u}>}{\partial x} - \frac{\partial<\tilde{w}\tilde{v}>}{\partial y} - \frac{\partial<\tilde{w}^2>}{\partial z} \\[2mm]
\frac{\partial<u>}{\partial x} + \frac{\partial<v>}{\partial y} + \frac{\partial<w>}{\partial z} &= 0.
\end{aligned}
\tag{3.5}
$$

A turbulence closure scheme (e.g., Pedlosky, 1979) has been used whereby the horizontal eddy viscosity ν_h and the vertical eddy viscosity ν link the turbulent stresses $< u_i'u_j' >$ to gradients in the mean flow.

Comparison with the usual shallow water equations (e.g, Pedlosky, eqs. 4.5.6) shows that the waves bring in extra perturbation stresses,

$$
\begin{bmatrix}
< \tilde{u}\tilde{u} > & < \tilde{u}\tilde{v} > & < \tilde{u}\tilde{w} > \\
< \tilde{v}\tilde{u} > & < \tilde{v}\tilde{v} > & < \tilde{v}\tilde{w} > \\
< \tilde{w}\tilde{u} > & < \tilde{w}\tilde{v} > & < \tilde{w}\tilde{w} >
\end{bmatrix}.
$$

In previous work on shelf circulation, the wave stresses are not considered. In the previous work on the surf zone dynamics, these wave stresses are partially included with $< \tilde{u}\tilde{w} >$ and $< \tilde{v}\tilde{w} >$ being ignored because they are understood to be zero (e.g. Svendsen 1989). However, the proceeding chapter has shown that when the earth's rotation is taken into account the wave orbital velocity components $\tilde{v}$ and $\tilde{w}$ are no longer in quadrature. Nor are $\tilde{u}$ and $\tilde{w}$ in quadrature if the wave direction is not coincident with the x-axis. As can be seen from Eqs. (3.5), it is the spatial

gradients of the wave stress that drive the flow. Therefore, stresses $< \tilde{u}\tilde{u} >$, $< \tilde{u}\tilde{v} >$ and $< \tilde{v}\tilde{v} >$ only play a role where there is a significant horizontal gradient in the wave field. That is why most of the previous research on wave driven flow has been confined to the surf zone where the wave breaking process results in large horizontal gradients in wave energy and momentum fluxes. In contrast, the spatial derivatives of $< \tilde{u}\tilde{w} >$ and $< \tilde{v}\tilde{w} >$ are principally vertical. As their name suggests, surface waves always have vertical variations, with wave activity being maximum on the surface and decaying downwards. This implies that the stresses $< \tilde{u}\tilde{w} >$ and $< \tilde{v}\tilde{w} >$ may be significant wherever there are surface waves.

3.2.2 The surface wave boundary layer defined from mean sea level to the free surface

Integrating the second equation of Eqs. (3.1), from mean sea level, $z =< \eta >$, to the free surface, $z = \eta \equiv < \eta > +\tilde{\eta}$ (where $< \eta >$ is the mean sea level and $\tilde{\eta}$ is the sea surface perturbation due to the short surface waves) and then time-averaging give

$$\left\langle \int_{<\eta>}^{\eta} \left\{ \frac{\partial v}{\partial t} + \frac{\partial uv}{\partial x} + \frac{\partial vv}{\partial y} + fu \right\} dz \right\rangle$$
$$= -\frac{1}{\rho} \left\langle \int_{<\eta>}^{\eta} \frac{\partial p}{\partial y} dz \right\rangle - < vw > |_{<\eta>}^{\eta} \qquad (3.6)$$

where it is assumed (as in linear or weakly non-linear wave theory) that the field can be extended analytically when η is less than $< \eta >$ (e.g., Longuet-Higgins, 1964; Hasselmann, 1971) .

Neglecting the third order terms for the LHS of Eq. (3.6) leads to

$$\left\langle \int_{<\eta>}^{\eta} \left\{ \frac{\partial v}{\partial t} + \frac{\partial uv}{\partial x} + \frac{\partial vv}{\partial y} + fu \right\} dz \right\rangle$$
$$= \frac{\partial < \tilde{v}\tilde{\eta} >}{\partial t} - < \tilde{v}\tilde{w} > |_{z=\eta} + f < \tilde{u}\tilde{\eta} > \qquad (3.7)$$

where, for the first integration, Eq. (2.97) has been used, and the last integration has been approximated by $f < \tilde{u}\tilde{\eta} >$. Using the third Eq. (3.1), one can write the first

term on the RHS of Eq. (3.6) as

$$\frac{1}{\rho}\left\langle \int_{<\eta>}^{\eta} \frac{\partial p}{\partial y} dz \right\rangle = g\left\langle \int_{<\eta>}^{\eta} \frac{\partial \tilde{\eta}}{\partial y} dz \right\rangle + \left\langle \int_{<\eta>}^{\eta} \frac{\partial}{\partial y} \int_{z}^{\eta} \frac{Dw}{Dt} dz' dz \right\rangle. \tag{3.8}$$

If the double integral term is neglected since it amounts only to a third order correction, then the pressure gradient term in Eq. (3.6) becomes

$$\frac{1}{\rho}\left\langle \int_{<\eta>}^{\eta} \frac{\partial p}{\partial y} dz \right\rangle = \frac{g}{2}\frac{\partial <\tilde{\eta}^2>}{\partial y}. \tag{3.9}$$

The second term on the RHS of Eq. (3.6) needs careful examination. First, because of Eq. (3.4),

$$<vw> |_{<\eta>}^{\eta} = [<v><w> + <\tilde{v}\tilde{w}> + <v'w'>]_{<\eta>}^{\eta}. \tag{3.10}$$

The difference between the value of $<v><w>$ at the top and the bottom of the wave slab is almost zero because the slow motion components change little within the wave slab. Recognizing that $- <v'w'>$ is the kinematic Reynolds stress τ_{yz}, which should be equal to the wind stress at the free surface, τ_y, one can express the above relation as

$$<vw> |_{<\eta>}^{\eta} = <\tilde{w}\tilde{v}> |_{<\eta>}^{\eta} + <v'w'> |_{<\eta>}^{\eta}$$
$$= <\tilde{w}\tilde{v}> |_{<\eta>}^{\eta} - \tau_y + \tau_{yz}|_{z=<\eta>}. \tag{3.11}$$

Substituting Eqs. (3.7), (3.9) and (3.11) into Eq. (3.6) gives the time averaged momentum balance for the whole wave slab

$$\tau_{yz}|_{z=<\eta>} = \left(\tau_y - \frac{\partial <\tilde{v}\tilde{\eta}>}{\partial t}\right) - \frac{g}{2}\frac{\partial <\tilde{\eta}^2>}{\partial x}$$
$$- <\tilde{v}\tilde{w}> |_{z=<\eta>} + f<\tilde{u}\tilde{\eta}>. \tag{3.12}$$

With Eqs. (2.100) and (2.112), the above expression can be reduced to

$$\tau_{yz}|_{z=<\eta>} = (\tau_y + \tilde{\tau}_y) - \frac{g}{2}\frac{\partial <\tilde{\eta}^2>}{\partial y}. \tag{3.13}$$

Similarly,

$$\tau_{xz} = (\tau_x + \tilde{\tau}_x) - \frac{g}{2}\frac{\partial <\tilde{\eta}^2>}{\partial x} \qquad \text{at } z = <\eta>. \tag{3.14}$$

As the shear stress condition at the mean sea level has been derived, the pressure condition needs to be derived as well. Integrating the third equation of Eqs. (3.1) from $z =< \eta >$ to η, time averaging, and neglecting third order corrections, results in

$$< p > = -\rho < \tilde{w}^2 > \qquad \text{at } z =< \eta >. \tag{3.15}$$

In obtaining the above equation, the atmospheric pressure has been set to zero, and the integration of the first term on LHS of the third equation of Eqs. (3.1) has been approximated as follows,

$$\left\langle \int_{<\eta>}^{\eta} \frac{\partial w}{\partial t} dz \right\rangle \approx \left\langle \tilde{\eta} \frac{\partial \tilde{w}}{\partial t} \right\rangle$$
$$= \frac{\partial < \tilde{\eta}\tilde{w} >}{\partial t} - \left\langle \tilde{w} \frac{\partial \tilde{\eta}}{\partial t} \right\rangle$$
$$= - < \tilde{w}^2 >, \tag{3.16}$$

where the quadrature relation between $\tilde{w}$ and $\tilde{\eta}$ has been used.

Integrating the fourth equation of Eqs. (3.1) from $z =< \eta >$ to $z = \eta$, one obtains the mass flux condition at $z =< \eta >$

$$< w > = \frac{\partial < \eta >}{\partial t} + < u > \frac{\partial < \eta >}{\partial x} + < v > \frac{\partial < \eta >}{\partial y}$$
$$+ \frac{\partial < \tilde{u}\tilde{\eta} >}{\partial x} + \frac{\partial < \tilde{v}\tilde{\eta} >}{\partial y}. \tag{3.17}$$

The results of this section show that the presence of the surface wave boundary layer modifies the shear stress, pressure, and mass flux at mean sea level.

3.3 The linearized system with horizontally homogeneous wave forcing

The derivation of Eqs. (3.5), (3.13), (3.14), (3.15) and (3.17) is useful in its own right because all the wave forces are completely included. Of course, the introduction of

wave forces greatly complicates the dynamics of the mean flow. It not only adds new source terms in the governing equations, but also changes the boundary conditions, especially at the surface. The objective of this thesis is not to provide a general solution to the whole set of equations. Instead, it aims to derive and study a simple linear Eulerian model for shelf dynamics which includes the wave force whose existence does not rely on horizontal gradients in wave energy.

Assumptions are needed to derive this simple model. The two main simplifications are the use of linearized equations of motion and horizontal homogeneity in the wave forcing. The linearization assumption greatly reduces the complexity of the equations, but still retains the first order dynamic features due to the the fact that the Rossby number in large scale motion (~ 100 km or larger) is often $\ll 1$. The assumption of horizontal homogeneity of wave forcing is not essential, but helps to isolate the influence of Coriolis-induced wave stress. Because of the linear superimposition principle, the effects due to wave horizontal inhomogeneity like mean sea level setup and set-down (Bowen and Inman, 1968) can be added to the results obtained in this thesis if desired. Further simplifications are homogeneous density and constant eddy viscosity (consistent with the way that the wave force is derived in the proceeding chapter), and neglecting horizontal friction. The constant density assumption will exclude baroclinic motions. While it would be interesting to address the effects of surface waves on the motion of stratified water, as a first attempt to introduce the mean wave forcing into shelf circulation dynamics, this thesis is focused on the barotropic motions.

With the above assumptions, Eqs. (3.5) can be simplified as

$$\frac{\partial < u >}{\partial t} - f < v > = -g\frac{\partial \eta}{\partial x} + \nu\frac{\partial^2 < u >}{\partial z^2} - \frac{\partial < \tilde{u}\tilde{w} >}{\partial z} \qquad (3.18)$$

$$\frac{\partial < v >}{\partial t} + f < u > = -g\frac{\partial \eta}{\partial y} + \nu\frac{\partial^2 < v >}{\partial z^2} - \frac{\partial < \tilde{v}\tilde{w} >}{\partial z} \qquad (3.19)$$

$$\frac{\partial < u >}{\partial x} + \frac{\partial < v >}{\partial y} + \frac{\partial < w >}{\partial z} = 0 \qquad (3.20)$$

and the surface conditions of Eqs. (3.14) and (3.13) are reduced to

$$\nu\frac{\partial <u>}{\partial z} = \tau_x + \tilde{\tau}_x \qquad z = 0 \qquad (3.21)$$

$$\nu\frac{\partial <v>}{\partial z} = \tau_y + \tilde{\tau}_y \qquad z = 0. \qquad (3.22)$$

The wave stress due to the bottom friction derived in the preceding chapter (cf., Eq. 2.64) resolves the very thin ($O(mm)$ thick, Russell and Osorio 1958) wave boundary layer. Thus a consistent choice of the bottom condition for the mean flow should be of the non-slip type

$$<u> = 0 \qquad \text{at } z = -h \qquad (3.23)$$

$$<v> = 0 \qquad \text{at } z = -h. \qquad (3.24)$$

The combination of the non-slip bottom condition and the constant eddy viscosity is rather crude assumption. Generally, the eddy viscosity decreases towards the real sea bed. As a first order approximation, however, this crude assumption is used here, the important point being Longuet Higgins' (1958) argument that the magnitude of the bottom streaming is not dependent on the viscosity structure inside the wave bottom friction layer.

Introducing a complex velocity $q = <u> + i <v>$, a complex transport $Q = \int_{-h}^{0} q\,dz$, and the gradient operator $\nabla = \partial/\partial x + i\partial/\partial y$, $\nabla^* = \partial/\partial x - i\partial/\partial y$, the above linearized equations can be written in a more concise and convenient form

$$\frac{\partial q}{\partial t} + ifq = -g\,\nabla\eta + \nu\frac{\partial^2 q}{\partial z^2} - q_{st}(0)\left[\frac{\psi(z)}{\cosh 2kh} + if\frac{\cosh 2k(h+z)}{\cosh 2kh}\right] \qquad (3.25)$$

$$\frac{\partial \eta}{\partial t} + \Re\{\nabla^* Q\} = 0. \qquad (3.26)$$

Here the wave force expression of Eq. (2.70) has been used, the continuity equation has been written in an integral form, and $\Re$ means the real part of a complex variable. On the complex plane, the surface and bottom conditions take the form

$$\nu\frac{\partial q}{\partial z} = \tau + \tilde{\tau} \qquad z = 0 \qquad (3.27)$$

$$q = 0 \qquad z = -h \qquad (3.28)$$

where $\tau = \tau_x + i\tau_y$ is the complex wind stress and $\tilde{\tau} = \tilde{\tau}_x + i\tilde{\tau}_y$ is the complex virtual wave stress.

Compared with the usual linearized shelf dynamic equations, the above linearized system (Eqs. 3.18 to 3.24, or Eqs. 3.25 to 3.28) differs due the addition of wave forcing, which manifests itself both as a body force in the momentum equation and as a surface force at the sea surface boundary. The momentum equations can then be regarded as being driven by three forces: wind stress, wave forces, and the pressure gradient. Unlike the wind stress and the wave forces which are imposed externally, the pressure gradient is not a real external force, since the sea surface elevation is, in part, the global response of the system to an external force. However when analyzing the momentum equations, or looking at the water motion column-wise (vertical Eulerian column), it is beneficial to treat it as a local external force. Chapter 4 will study the response of a local water column to the wave forcing.

3.4 Relationship between the responses of the linearized system to step and arbitrary forcing

In studying the response of a local water column (in an Eulerian sense) to arbitrary local external forces, it is beneficial to analyze the response of the system to step functions (in time) of the external forces. The system response to an arbitrary force can then be ascertained by means of a time convolution. For example, the response of the system to an arbitrary wind force can be determined by the following procedures.

- First, seek the fluid response to a Heaviside step function of unit wind force, which is denoted as I_τ and defined as

$$I_\tau(t) \;=\; \begin{cases} 1 & t \geq 0 \\ 0 & t < 0. \end{cases} \qquad (3.29)$$

A property of the Heaviside step function is

$$\frac{\partial I_\tau}{\partial t} \;=\; \delta(t) \qquad (3.30)$$

in which $\delta(t)$ is the Dirac delta function. Denote q_d as the wind driven flow, whose response to the step function is described by

$$
\left.
\begin{aligned}
&\frac{\partial q_d}{\partial t} + if q_d - \nu \frac{\partial^2 q_d}{\partial z^2} = 0 \\
&\nu \frac{\partial q_d}{\partial z}\Big|_{z=0} = I_\tau \\
&q_d\big|_{z=-h} = 0 \\
&q_d\big|_{t=0} = 0
\end{aligned}
\right\}.
\tag{3.31}
$$

Using notation L_1 to denote the above linear system, the relationship between input and output can be written as

$$
L_1[I_\tau] = q_d(t, z; I_\tau),
\tag{3.32}
$$

where $q_d(t, z; I_\tau)$ indicates explicitly that this flow is driven by a unit step wind force. Using property of Eq. (3.30), it follows that

$$
L_1[\delta(t)] = \frac{\partial q_d(t, z; I_\tau)}{\partial t} \equiv \dot{q}_d(t, z; I_\tau)
\tag{3.33}
$$

(the dot denotes the time derivative). Thus $\dot{q}_d$ is the so-called Green's function, and could be obtained in a more direct way. The treatment of presenting the Green's function as a second step after the solution of q_d, which follows Welander (1957), may be of more physical appeal since q_d has a more direct physical interpretation than $\dot{q}_d$.

- Second, seek the response to the arbitrary forcing $\tau(t)$. Since

$$
\tau(t) = \int_0^t \tau(t')\delta(t - t')dt'
\tag{3.34}
$$

then

$$
\begin{aligned}
L_1[\tau(t)] &= \int_0^t \tau(t')L_1[\delta(t - t')]\,dt' \\
&= \tau(t) * \dot{q}_d(t, z; I_\tau).
\end{aligned}
\tag{3.35}
$$

The same procedure can be applied to the wave-driven flow. Defining q_w as the response to the wave force, the response to unit step surface Stokes drift, denoted by

I_{st}, is governed by

$$\left.\begin{array}{l} \frac{\partial q_w}{\partial t} + ifq_w - \nu\frac{\partial^2 q_w}{\partial z^2} = -I_{st}\left[\frac{\psi(z)}{\cosh 2kh} + if\frac{\cosh 2k(h+z)}{\cosh 2kh}\right] \\ \nu\frac{\partial q_w}{\partial z}\Big|_{z=0} = I_{st}2\nu k\tanh(2kh) \\ q_w\big|_{z=-h} = 0 \\ q_w\big|_{t=0} = 0 \end{array}\right\}. \qquad (3.36)$$

Using L_2 to denote the above linear system, then the input and output relations can be expressed simply as

$$L_2\left[I_{st}\right] = q_w(t; I_{st}). \qquad (3.37)$$

When the Stokes drift is varying with time, then the response of L_2 is

$$L_2\left[\mathcal{St}(t)\right] = \mathcal{St}(t) * \dot{q}_w(t, z; I_{st}) \qquad (3.38)$$

where n tation $\mathcal{St}(t)$ stands for the time varying surface value of the Stokes drift (cf. page 14 for this notation).

Similarly, denote q_s as the response to the slope force. The response to the unit step slope force, denoted $I_{\nabla\eta}$, obeys

$$\left.\begin{array}{l} \frac{\partial q_s}{\partial t} + ifq_s - \nu\frac{\partial^2 q_s}{\partial z^2} = -gI_{\nabla\eta} \\ \nu\frac{\partial q_s}{\partial z}\Big|_{z=0} = 0 \\ q_s\big|_{z=-h} = 0 \\ q_s\big|_{t=0} = 0 \end{array}\right\}, \qquad (3.39)$$

or can be expressed by

$$L_3[I_{\nabla\eta}] = q_s(t, z; I_{\nabla\eta}) \qquad (3.40)$$

where L_3 is short for the pressure gradient driven linear system. Then the response to the arbitrary slope force is

$$L_3[\nabla\eta(t)] = \nabla\eta(t) * \dot{q}_s(t, z; I_{\nabla\eta}). \qquad (3.41)$$

Equations (3.35), (3.38) and (3.41) all have the form of

$$F * \dot{R} \tag{3.42}$$

where F signifies the force and R the step function response. An alternative form will also be useful in later discussions. Using partial integration

$$
\begin{aligned}
F * \dot{R} &\equiv \int_0^t F(t') \frac{\partial R(t-t')}{\partial t} dt' \\
&= F(0)R(t) + \int_0^t R(t-t') \frac{\partial F(t')}{\partial t'} dt'
\end{aligned}
\tag{3.43}
$$

where $R(0) = 0$ has been used, as demanded by the initial conditions (cf., the fourth equations of Eqs. 3.31, 3.36, and 3.39). The case of a suddenly imposed force has been explicitly taken care of by the first term on the RHS. The above two terms may be further merged as a single term by using the relationship between the δ—function and Heaviside function, as is shown below. Since

$$
\begin{aligned}
F(0)R(t) &+ \int_0^t R(t-t') \frac{\partial F(t')}{\partial t'} dt' \\
&= \int_0^t R(t-t') \left[F(t')\delta(t') + \frac{\partial F(t')}{\partial t'} \right] dt' \\
&= \int_0^t R(t-t') \frac{\partial [F(t')H(t')]}{\partial t'} dt'
\end{aligned}
\tag{3.44}
$$

where $H(t)$ denotes the Heaviside step function, then Eq. (3.42) becomes

$$
F(t) * \frac{\partial R(t)}{\partial t} = \frac{\partial [F(t)H(t)]}{\partial t} * R(t)
\tag{3.45}
$$

in which $H(t)$ is there in case $F(t)$ is suddenly setup at the start. Thus Eqs. (3.35), (3.38) and (3.41) can be also written as

$$
L_1[\tau(t)] = \frac{\partial [\tau(t)H(t)]}{\partial t} * q_d(t, z; I_\tau),
\tag{3.46}
$$

$$
L_2[\mathcal{R}(t)] = \frac{\partial [\mathcal{R}(t)H(t)]}{\partial t} * q_w(t, z; I_{sl}),
\tag{3.47}
$$

$$
L_3[\nabla \eta(t)] = \frac{\partial [\nabla \eta(t)H(t)]}{\partial t} * q_s(t, z; I_{\nabla \eta}).
\tag{3.48}
$$

3.5 Summary

Equations (3.5), (3.13), (3.14), (3.15) and (3.17) form a general set of governing equations for shallow water motion which includes wave forces in a 3D sense. Equations (3.25), (3.26), (3.27), (3.28) represent the linearized system, which includes, in addition to the wind stress, the Coriolis induced and frictional wave boundary layer induced wave stress. The linear system is then decomposed into three linear subsystems, L_1, L_2, L_3, driven by winds, waves, and pressure gradients, respectively. The response of each sub-system to the Heaviside step function is important in the sense that the response to an arbitrary force can then be determined by means of a time convolution, as is shown by Eq. (3.42) (to which Eq. (3.45) is a useful alternative form).

Chapter 4

Wind- and Wave-driven Flow in Water of Arbitrary Depth

4.1 Introduction

As has been noted in Chapter 3, when the pressure gradient is regarded as a local force, the momentum equation can be dealt with separately from the continuity equation and water motion can be viewed column-wise. The response of the water column (in an Eulerian sense) to wind forcing and pressure gradients is familiar as Ekman dynamics. This chapter explores the response to wave forcing in arbitrary water depth. Specifically, Eqs. (3.25), (3.27) and (3.28) will be solved. Solutions for the other two responses will also be presented, but discussions will focus on the response to wave forcing.

4.2 Steady flows

By dropping the time derivative term in Eqs. (3.25), the steady response of a water column to constant winds, waves and pressure gradients is described by

$$ifq = -g\,\nabla\eta + \nu\frac{\partial^2 q}{\partial z^2} - q_{st}(0)\left[\frac{\psi(z)}{\cosh 2kh} + if\frac{\cosh 2k(h+z)}{\cosh 2kh}\right] \qquad (4.1)$$

$$\nu \frac{\partial q}{\partial z} = \tau + \tilde{\tau} \qquad z = 0 \tag{4.2}$$

$$q = 0 \qquad z = -h. \tag{4.3}$$

The solution to these equations can be expressed as the sum of a classical wind driven surface Ekman flow, q_{ds}, the wave driven flow, q_{ws}, and the pressure gradient induced bottom Ekman flow, q_{ss}, (which includes the interior geostrophic flow, but varies with the vertical coordinate mainly near the bottom)

$$q = q_{ds} + q_{ws} + q_{ss} \tag{4.4}$$

(where the letters d, w, and s in the first subscript positions stand for (wind) drift, wave-driven, and slope-driven, and the letters of s's in the second subscript positions stand for the steady flow). The expressions for q_{ds} and q_{ss} are given by

$$q_{ds} = \frac{\tau}{f\delta_e} SE(z) \tag{4.5}$$

$$q_{ss} = i\frac{g \nabla \eta}{f} BE(z) \tag{4.6}$$

where SE stands for the Surface Ekman layer

$$SE(z) = \sqrt{2}e^{-i\pi/4}\frac{\sinh \alpha(h+z)}{\cosh \alpha h} \tag{4.7}$$

and BE is the Bottom Ekman layer,

$$BE(z) = 1 - \frac{\cosh \alpha z}{\cosh \alpha h} \tag{4.8}$$

in which

$$\delta_e = \sqrt{\frac{2\nu}{f}} \tag{4.9}$$

$$\alpha = \frac{1+i}{\delta_e}. \tag{4.10}$$

The solution for the wave driven steady flow q_{ws} is complicated, and it is useful to decompose it as

$$q_{ws} = q_{ws}^{(1)} + q_{ws}^{(2)} + q_{ws}^{(3)} \tag{4.11}$$

where

$$q_{ws}^{(1)} = \frac{\tilde{\tau}}{f\delta_e}SE(z) \tag{4.12}$$

$$q_{ws}^{(2)} = q_{st}(-h)\left[\frac{3}{2}\frac{\cosh \alpha z}{\cosh \alpha h} + BW(\beta z')\right] \tag{4.13}$$

$$q_{ws}^{(3)} = q_{st}(0)FW(z) \tag{4.14}$$

and

$$FW(z) = \frac{e^{-i\pi}}{1 + \frac{i}{2}\left(\frac{\delta_e}{\delta_{st}}\right)^2}\left\{\frac{\cosh 2k(h+z)}{\cosh(2kh)} - \frac{\cosh(\alpha z)}{\cosh(2kh)\cosh(\alpha h)}\right.$$
$$\left. -\frac{1}{2}\left(\frac{\delta_e}{\delta_{st}}\right)\tanh(2kh)SE(z)\right\} \tag{4.15}$$

$$BW(\beta z') = e^{-2\beta z'} - 2(\beta z' + 2)e^{-\beta z'}\cos\beta z' - 2(\beta z' - 1)e^{-\beta z'}\sin\beta z', \tag{4.16}$$

where $z' = z + h$. In Eq. (4.11), the first part, $q_{ws}^{(1)}$, is the surface Ekman flow driven by the virtual tangential wave stress (similar to flow driven by the wind stress). The second part, $q_{ws}^{(2)}$, is driven by wave stress within the wave boundary layer. It includes two terms: the first term is bottom streaming modified by the earth's rotation (cf. Eq. 2.21), and the second term $BW(\beta z')$ is insignificant outside of the wave boundary layer but this term makes the bottom streaming at the top of the wave boundary layer sharply reduce to zero down at the real bottom. As Fig. (4.1.a) shows, the introduction of the earth's rotation tends to restrict the flow to the two Ekman layers.

$q_{ws}^{(3)}$ is the flow that is driven by Coriolis-induced wave stress. It has three terms: the first term describes the Eulerian return flow which would completely compensate the Stokes drift in an inviscid fluid but is now modified by the ratio of δ_e/δ_{st} (Fig. 4.1.b); the second term accounts for the effect of bottom friction; and the third term results from a requirement of zero stress at the sea surface. The wind stress and the virtual stress have been taken care of by q_{ds} and $q_{ws}^{(1)}$.

There are two vertical scales associated with the wave-driven flow. One is the Ekman depth, $\delta_e = \sqrt{2\nu/f}$, imposed internally by friction and the Coriolis parameter. The other is the Stokes depth, $\delta_{st} = 1/(2k)$, which is imposed externally by the surface wave field. The nature of the total wave driven steady flow, q_{ws}, critically depends on the ratio of δ_e/δ_{st}. When the ratio is infinitely large (the non-rotating case), q_{ws} approaches zero. When the ratio approaches zero (the inviscid case), q_{ws} becomes a return flow, which is an Eulerian flow of the same magnitude as the Stokes drift but with the opposite sign. Figure (4.1.c) shows the vertical structure of flow driven by both Coriolis- and viscosity-induced wave stresses, and Fig. (4.1.d) is a 3-D sketch. Figure (4.2) shows the vertical profiles of q_{ws} for various values of δ_e/h and δ_{st}/h.

The three part summation of Eq. (4.11) can be re-expressed as

$$
q_{ws} = q_{st}(0)\left[\frac{\sqrt{2}}{2}\frac{\delta_e}{\delta_{st}}e^{-i\frac{\pi}{4}}\frac{\sinh\alpha(h+z)}{\cosh\alpha h}\tanh 2kh\right.
$$
$$
\left. +\frac{1}{2\cosh 2kh}\left(3\frac{\cosh\alpha z}{\cosh\alpha h}+\mathrm{BW}(\beta z')\right)+\mathrm{FW}(z)\right] \qquad (4.17)
$$

where the virtual wave stress $\tilde{\tau}$ has been expressed in term of the surface value of Stokes drift $q_{st}(0)$ (cf. Eq. 2.74). This formula explicitly shows that the size of the Stokes drift is a good indication of the size of this wave-driven Eulerian flow. Letting $\mathrm{WA}(z)$ denote the vertical distribution inside the square parenthesis, then the formula can be stated concisely as

$$
q_{ws} = q_{st}(0)\mathrm{WA}(z). \qquad (4.18)
$$

4.3 Some limiting cases for the wave-driven steady flow q_{ws}

A discussion of limiting cases for steady wave-driven flow, q_{ws}, is given below.

- When $f \to 0$ and h is finite, then $\delta_e \to \infty$, $\alpha \to 0$, and

$$
q_{ws}^{(1)} + q_{ws}^{(2)} \to \left[\frac{\tilde{\tau}}{\nu}(h+z)+\frac{3}{2}q_{st}(-h)\right] \qquad (4.19)
$$
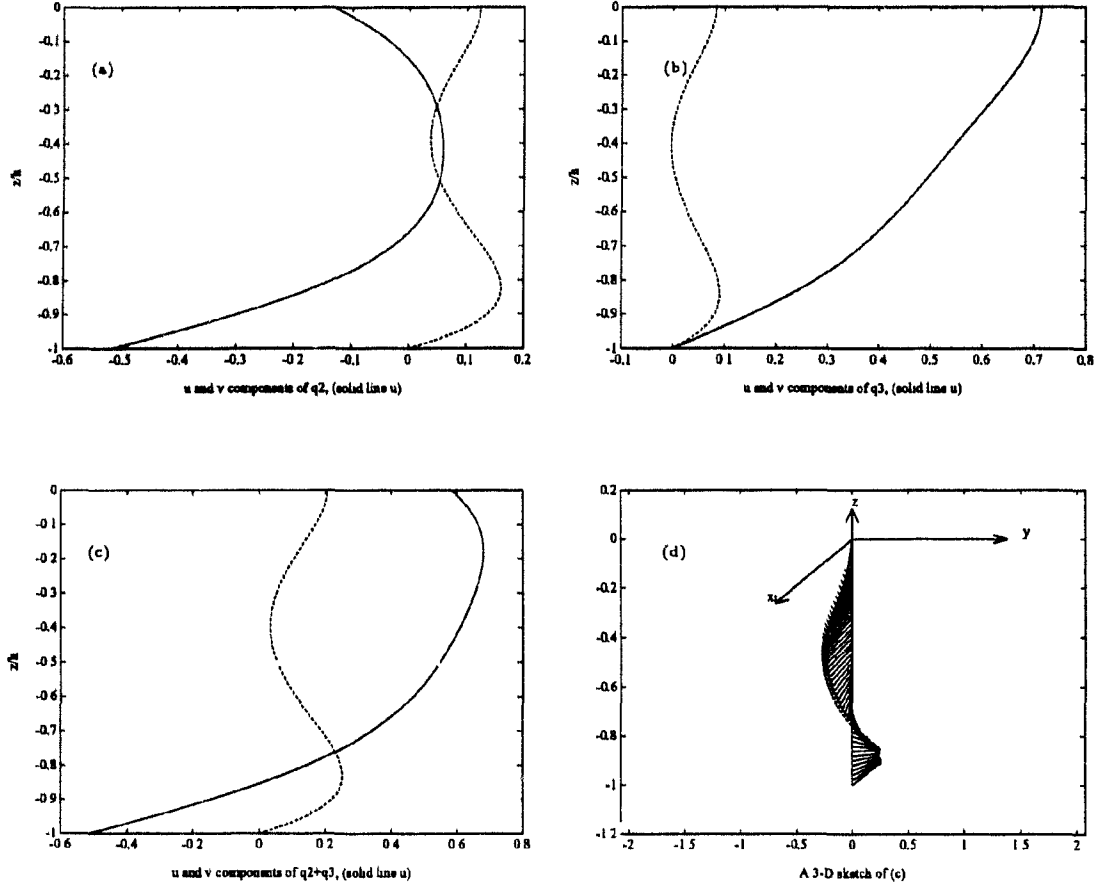
Figure 4.1: The vertical structure of wave-driven steady flow, scaled by $a^2\sigma/\delta_{st}$. (a) Flow driven by viscous-induced wave stress, $q_{ws}^{(1)} + q_{ws}^{(2)}$. (b) Flow driven by Coriolis-induced wave stress, $q_{ws}^{(3)}$. (c) Flow driven by both Coriolis- and viscous-induced wave stress, $q_{ws}^{(1)} + q_{ws}^{(2)} + q_{ws}^{(3)}$. (d) the 3-D sketch of (c). The parameters are $h = 50m$, $\delta_e/h = 0.23$, $\delta_{st}/h = 0.65$, $\theta = \pi$ for a wave propagating in the minus x direction. $\mathrm{BW}(\beta z')$ is not plotted because it is too thin. (The value of Stokes drift velocity at the bottom is -0.34, which, makes the value of the bottom streaming $-3/2 \times 0.34 = -0.51$.)
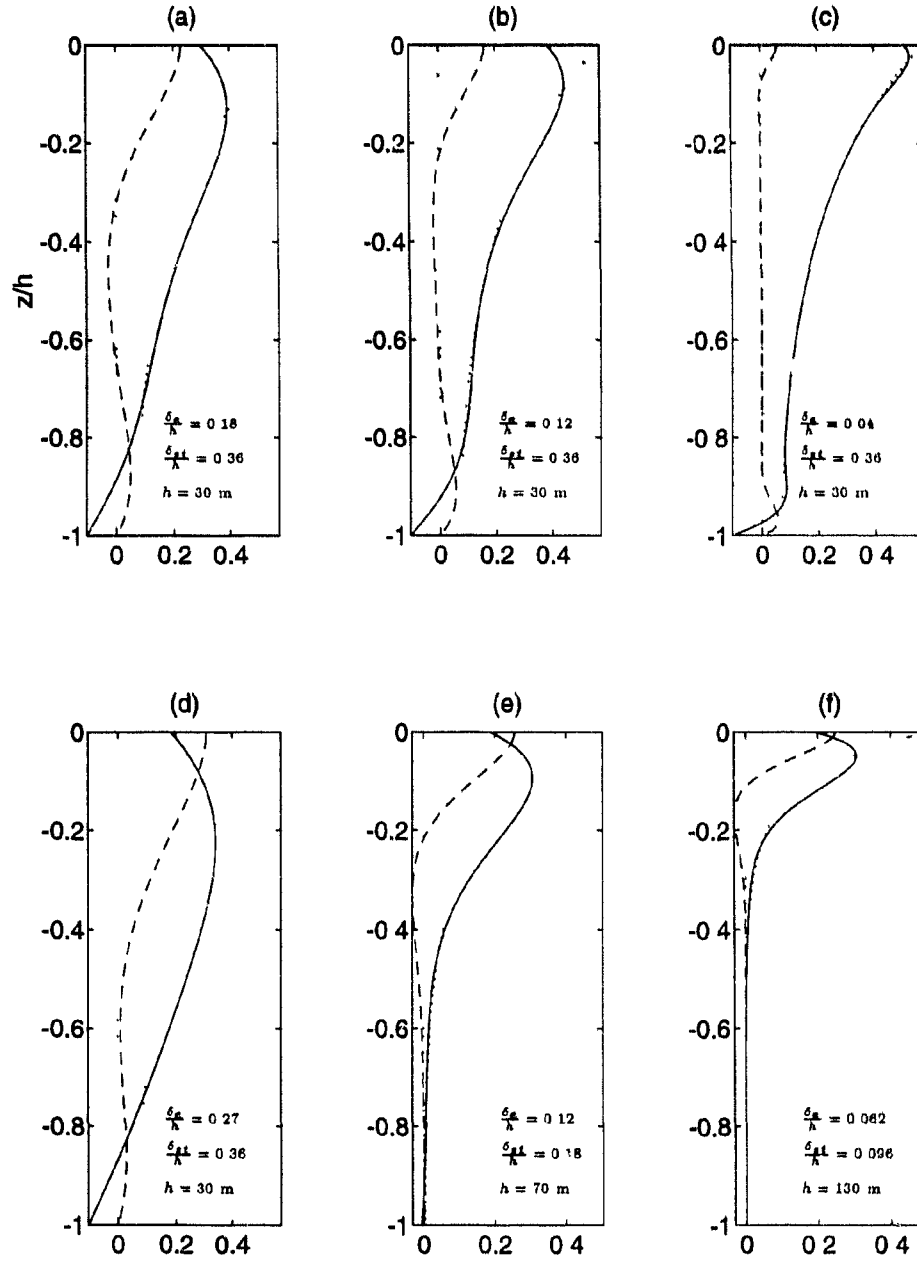
Figure 4.2: The structure of the wave driven flow as function of the two ratios, δ_r/h and δ_{st}/h. The solid line is the $u-$ component, the dashed line is the $v-$component. The inviscid solution (mirror image of the Stokes drift) is shown by the dotted line.

$$FW(z) \quad \rightarrow \quad 0. \tag{4.20}$$

Thus

$$q_{ws} = \left[\frac{\tilde{\tau}}{\nu}(h+z) + \frac{3}{2}q_{st}(-h) \right] \tag{4.21}$$

which, if added to the Stokes drift, recovers Longuet-Higgins' mass transport theory for a non-rotational viscid fluid.

Longuet-Higgins first obtained the virtual tangential stress. The results were then questioned by Huang (1970). He pointed out that Longuet-Higgins formula of Eq. (4.21) gives an infinite wave mass transport when a deep water limit is taken. This is the so-called Longuet-Higgins paradox. Ünlüata and Mei (1970) then re-examined the wave mass transport problem using a Lagrangian approach. Their result showed that Longuet-Higgins' result is indeed correct, given its underlying assumption that a steady state for the mass transport has been reached. The paradox arises because in a non-rotating deep water system, the virtual surface wave stress remains unbalanced. Madsen (1978) then introduced the Coriolis force into the model to balance the virtual wave stress and successfully resolved Longuet-Higgins' paradox.

- The limit $f \rightarrow 0$ and $h \rightarrow \infty$ is an unrealistic case. This is equivalent to demanding that a steady state is achieved in infinitely deep water as was originally demanded by Huang (1970).

- When $f \neq 0$ and $\nu \rightarrow 0$, then $\delta_e \rightarrow 0$, $\alpha \rightarrow \infty$, and

$$q_{ws}^{(1)} + q_{ws}^{(2)} \quad \rightarrow \quad 0 \tag{4.22}$$

$$FW(z) \quad \rightarrow \quad \frac{\cosh 2k(h+z)}{4\sinh^2(kh)}. \tag{4.23}$$

Thus

$$q_{ws} = -q_{st} \tag{4.24}$$

which recovers Ursell's (1950) and Hasselmann's (1970) theory. The theory states that in a rotating inviscid ocean the Lagrangian mean flow must vanish. By adding Stokes drift velocity to the above Eulerian velocity, the required zero Lagrangian mean is obtained. Thus, Eq. (4.17) provides a unified formula for the wave driven flow in arbitrary water depth, encompassing Longuet-Higgins' viscid but non-rotational theory and Ursell and Hasselmann's inviscid but rotational theory.

Equation (4.24) suggests a mechanism for the generation of wave-induced return flow. Traditionally the following explanation of the wave-induced return flow is given. A surface wave field produces a steady Stokes drift, when the drift hits a physical wall, water piles up and a pressure gradient is generated which drives a return flow in the opposite direction to the wave propagation to compensate for the Stokes drift (Fig. 4.3.a). This mechanism depends on the existence of a physical wall and it is hard to picture in a region far from lateral boundaries. The Coriolis-induced wave force offers an alternative mechanism for generating the compensating return flow. As is indicated by Eq. (4.24), the Coriolis force generated return flow is a depth dependent mirror image of the Stokes drift, while a pressure force generated return flow would be depth independent (Fig. 4.3.b).

Equation (4.24) then predicts there will be a mean return flow component in a velocity time series recorded by any mooring current meter where there are surface waves. Any attempt to explain the observed current without considering the surface wave effects may lead to wrong conclusions. A possible example of this will be discussed later.

- When $h \rightarrow \infty$

$$FW(z) \rightarrow \frac{1}{2 + i\left(\frac{\delta_e}{\delta_{st}}\right)^2}\left[e^{2kz} - \frac{\sqrt{2}}{2}e^{\left(-i\frac{\pi}{4}\right)}\left(\frac{\delta_e}{\delta_{st}}\right)e^{\alpha z}\right] \qquad (4.25)$$

$$q_{ws}^{(1)} \rightarrow \frac{\tilde{\tau}}{\rho f \delta_e}\sqrt{2}e^{-i\frac{\pi}{4}}e^{\alpha z} \qquad (4.26)$$
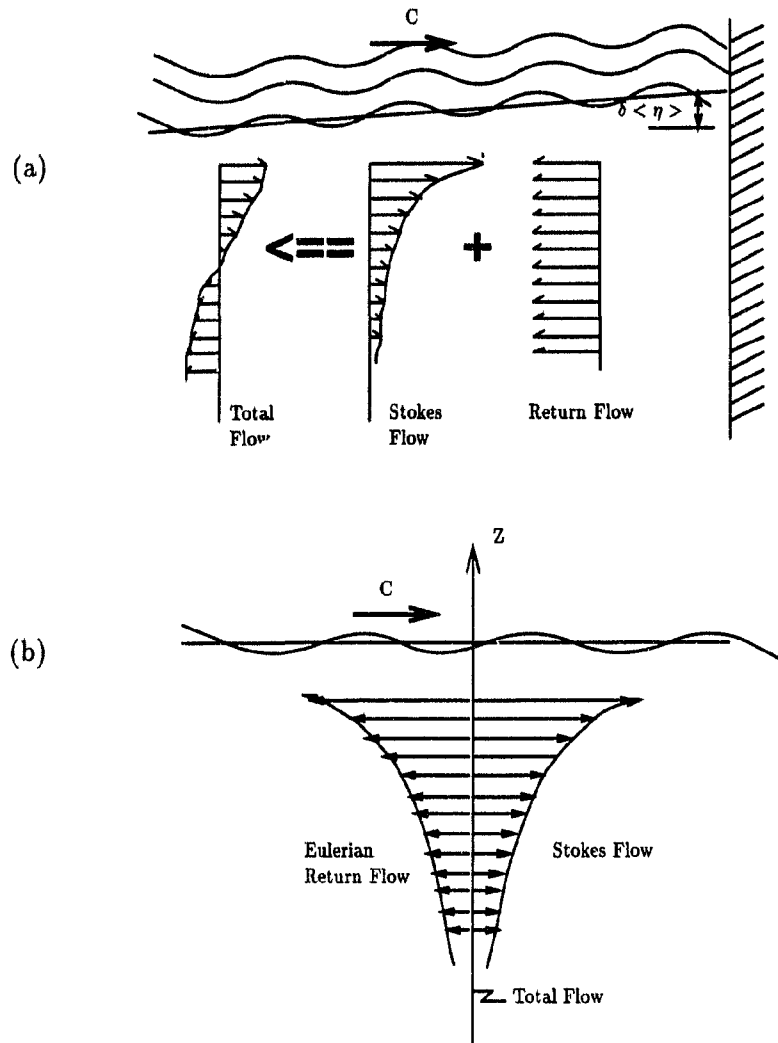
Figure 4.3: (a) The traditional explanation for wave-induced return flow. (a) A physical wall blocking the wave-induced Stokes drift is a necessity for generating return flow; (b) An alternative explanation for wave-induced return flow. Return flow can be generated without lateral boundary, and the vertical distribution is a mirror image of the Stokes flow (for the case of no friction).

$$q_{ws}^{(2)} \rightarrow 0 \tag{4.27}$$

$$q_{ws} = \frac{a^2 e^{i\theta}\sigma}{\delta_{st}}e^{-i\pi}\left[\frac{e^{2kz} - \frac{\sqrt{2}}{2}e^{\left(-i\frac{\pi}{4}\right)}\left(\frac{\delta_e}{\delta_{st}}\right)e^{\alpha z}}{2 + i\left(\frac{\delta_e}{\delta_{st}}\right)^2}\right] + \frac{\tilde{\tau}}{\rho f \delta_e}\sqrt{2}e^{-i\frac{\pi}{4}}e^{\alpha z} \tag{4.28}$$

which, if added to the Stokes drift, recovers Madsen's (1978) deep water solution in Lagrangian form.

4.4 Unsteady flows

Unsteady flows driven by winds, waves, and pressure gradients are now investigated. The discussion will focus mainly on flows driven by waves. Considered first is the transient solution to a suddenly imposed steady wave force, then, the response to arbitrary time varying wave force. The solutions for the wind- and slope-induced unsteady flows are also given.

4.4.1 Transient solution for a suddenly imposed steady wave forcing

Denote q_{wt} as the transient response to a suddenly imposed steady wave forcing. The total response is then the sum of q_{wt} and the steady solution q_{ws}, which has already been obtained as in Eq. (4.17). The transient response is governed by

$$\nu\frac{\partial^2 q_{wt}}{\partial z^2} - if q_{wt} - \frac{\partial q_{wt}}{\partial t} = 0 \tag{4.29}$$

$$q_{wt} = 0 \qquad z = -h \tag{4.30}$$

$$\nu\frac{\partial q_{wt}}{\partial z} = 0 \qquad z = 0 \tag{4.31}$$

$$q_{wt} = -q_{ws} \qquad t = 0 \text{ and } -h < z < 0. \tag{4.32}$$

This is an eigenvalue problem with

$$\cos(\omega_n z) \qquad (n = 0, 1, 2, 3, ...) \tag{4.33}$$

$$\omega_n = \frac{2n + 1}{2h}\pi \tag{4.34}$$

as its eigenfunctions and eigenvalues respectively. (Note the eigen-mode counts from $n = 0$ throughout the thesis.) The transient solution is found to be

$$q_{wt} = -q_{st}(0) \sum_{n=0}^{\infty} s_n e^{-(\gamma_n^2 + i)ft} \cos(\omega_n z) \qquad (4.35)$$

where γ_n is given by

$$\gamma_n = \omega_n \sqrt{\frac{\nu}{f}} \qquad (4.36)$$

$$= \frac{1}{\sqrt{2}} \left(\frac{2n+1}{2} \pi \right) \left(\frac{\delta_e}{h} \right), \qquad (4.37)$$

and

$$s_n = \frac{2}{h} \int_{-h}^{0} WA(z) \cos(\omega_n z) dz \qquad (4.38)$$

where the initial condition of Eq. (4.32) has been used and $WA(z)$ is given by Eq. (4.18).

The total solution is the sum of the steady solution and the transient solution, i.e.

$$q_w = q_{st}(0) \left[WA(z) - \sum_{n=0}^{\infty} s_n e^{-(\gamma_n^2 + i)ft} \cos(\omega_n z) \right]. \qquad (4.39)$$

By replacing $q_{st}(0)$ in the above expression by its unit Heaviside step force, I_{st}, the response

$$q_w(t, z; I_{st}) = I_{st} \left[WA(z) - \sum_{n=0}^{\infty} s_n e^{-(\gamma_n^2 + i)ft} \cos(\omega_n z) \right], \qquad (4.40)$$

is obtained, which will be useful in discussing the flow driven by an arbitrary time varying wave field.

Figure (4.4) shows different views of the temporal development of flow driven by a steady wave field. Panels (a) and (b) of Fig. (4.4) show the development of vertical profiles of u and v. The profiles start from zero in the interior region, gradually accelerate, oscillate at the inertial frequency and finally settle down to the steady responses (shown by the most dense lines) on a momentum diffusion time scale of $(h/\delta_e)^2$. The final non-zero value of u at the bottom is the bottom streaming just

above the thin wave bottom boundary layer (which is not plotted because it is too thin). Panels (c) and (d) of Fig. (4.4) are time series of the surface values of u and v. Panel (e) of Fig. (4.3) is hodograph of u against v at different depths.

When $h \rightarrow \infty$, Eqs. (4.35) and (4.38) are replaced by

$$q_{wt} = -q_{st}(0) \int_0^\infty s(\omega) e^{-(if+\omega^2 \nu)t} \cos(\omega z) d\omega \qquad (4.41)$$

and

$$s(\omega) = \frac{2}{\pi} \int_{-\infty}^0 \mathrm{WA}(z) \cos(\omega z) dz. \qquad (4.42)$$

The deep water transient solution may be rewritten as

$$q_{wt} = -q_{st}(0) e^{-ift} \int_{-\infty}^\infty \mathrm{WA}(z - z') \frac{e^{-\frac{z'^2}{4\nu t}}}{\sqrt{4\pi \nu t}} dz' \qquad (4.43)$$

since

$$\int_0^\infty s(\omega) \cos(\omega z) d\omega = -\mathrm{WA}(z) \qquad (4.44)$$

$$\int_0^\infty e^{-\omega^2 \nu t} \cos(\omega z) d\omega = \frac{1}{2} \sqrt{\frac{\pi}{\nu t}} e^{-\frac{z^2}{4\nu t}}. \qquad (4.45)$$

The total solution for deep water is then

$$q_w = q_{st}(0) \left[\mathrm{WA}(z) - e^{-ift} \int_{-\infty}^\infty \mathrm{WA}(z - z') \frac{e^{-\frac{z'^2}{4\nu t}}}{\sqrt{4\pi \nu t}} dz' \right]. \qquad (4.46)$$

When ν approaches zero,

$$\lim_{\nu \to 0} \frac{e^{-\frac{z^2}{4\nu t}}}{\sqrt{4\pi \nu t}} = \delta(z), \qquad (4.47)$$

where $\delta(z)$ is the Dirac delta function, and $q_{st}(0)\mathrm{WA}(z)$ approaches $-q_{st}(z)$ as described by Eq. (4.24). Therefore Eq. (4.46) becomes

$$q_w(z) = [-q_{st}(z) + e^{-ift} q_{st}(z)] \qquad (4.48)$$

which recovers Hasselmann's (1970) inertial oscillation solution in an inviscid deep ocean. Hasselmann proposed the Coriolis-induced wave force as a new generation mechanism, as an alternative to those of tidal generation and wind generation, for the inertial oscillations often observed in the open ocean.
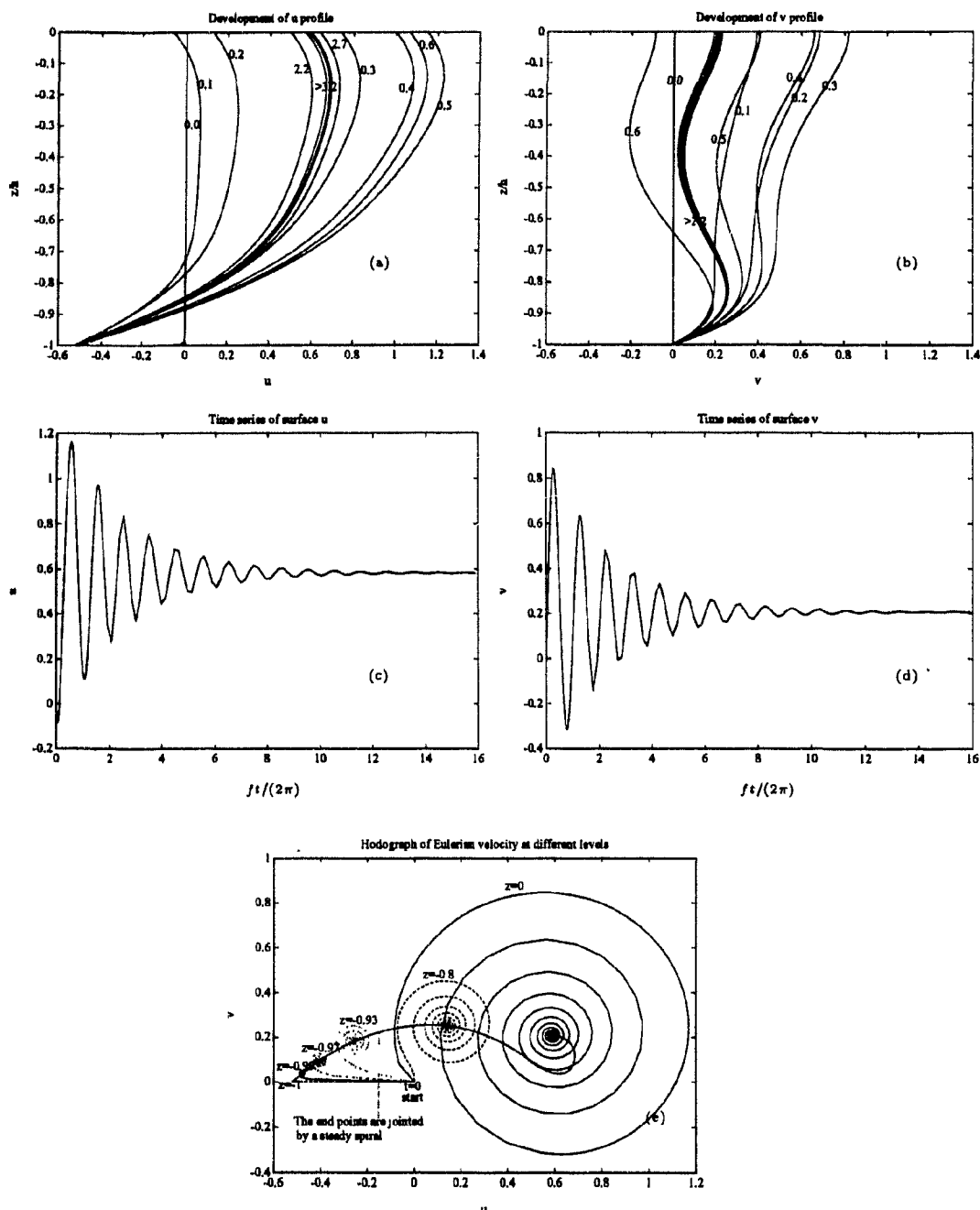
Figure 4.4: Different views on the flow development driven by a steady wave ($\delta_e/h = 0.23$, $\delta_{st}/h = 0.65$, $\theta = \pi$). The numbers beside the curves in (a) and (b) are the values of $ft/(2\pi)$. The velocity is scaled by the strength of Stokes drift, $a^2\sigma/\delta_{st}$ (for detailed description see text).

4.4.2 Solution for general unsteady wave forcing

In the above, the surface value Stokes drift remains constant after it is introduced at the initial time. Relaxing this assumption and assuming that $\mathfrak{R}(t) = q_{st}(t, z)|_{z=0}$ can vary as an arbitrary function of time (note that notation $\mathfrak{R}$ is used, cf. the explanation on page 14). Using the relation presented by Eq. (3.38), the response to the time varying Stokes drift is

$$q = \int_0^t \mathfrak{R}(t') \frac{\partial q_w(t - t'; I_{st})}{\partial t} dt' \tag{4.49}$$

which can be written as

$$q = \int_0^t \frac{\partial [\mathfrak{R}(t') H(t')]}{\partial t'} q_w(t - t'; I_{st}) dt' \tag{4.50}$$

by using of Eq. (3.45), where $q_w(t, I_{st})$ has been given by Eq. (4.40).

For a suddenly imposed unidirectional wave afterwards subjected to decay due to both internal friction and bottom friction,

$$\mathfrak{R}(t) = e^{-(4\nu k^2 + \nu\beta k/ \sinh 2kh)t} a^2 e^{i\theta} \tag{4.51}$$

(this energy dissipation rate can be worked out by substitution of Eqs. 2.59 and 2.60 into Eq. 2.109 and retaining the leading terms in the interior and bottom regions respectively, also see Phillips, 1977, page 52-53). Thus

$$\frac{\partial [\mathfrak{R}(t) H(t)]}{\partial t} = a^2 e^{i\theta} \left[\delta(t) - (4\nu k^2 + \frac{\nu\beta k}{\sinh 2kh}) H(t) \right] e^{-(4\nu k^2 + \nu\beta k/ \sinh 2kh)t}. \tag{4.52}$$

The time varying form of the wave energy given in Eq. (4.51) is valid for wave decay due to a molecular viscosity or a constant eddy viscosity. When waves are breaking, the form of $\mathfrak{R}(t)$ is uncertain, and the problem of defining a proper form is beyond the scope of this chapter. Weber and Melson (1993a) have recently addressed this problem. Their idea is that, although the form of $\mathfrak{R}(t)$ for breaking waves is difficult to obtain, the wave heights before and after breaking and the time duration for the breaking may be known from experiments. Thus one can calculate $\Delta\mathfrak{R}(t)/\Delta t$

as an approximation for $\partial \mathfrak{R}(t)/\partial t$. As we can see from Eq. (4.50), it is the time derivative of $\mathfrak{R}(t)$ not $\mathfrak{R}(t)$ itself that determines the time varying wave-driven flow.

The above analysis is for a monochromatic and unidirectional wave field. However, since the model is linear, responses for different wave frequencies can be summed when the wave field is random. All that is required is to replace a^2 in Eq. (4.17) by

$$2(\rho g)^{-1} S(\sigma, \theta) d\sigma d\theta,$$

where $S(\sigma, \theta)$ is the wave energy directional spectrum, and then integrate Eq. (4.17) over a suitable range of frequencies and directions. The results described by Eqs. (4.39), (4.46) and (4.49) will formally remain the same.

4.4.3 Unsteady flows driven by the sum of three arbitrary forces

In the same manner in which the wave step force response, $q_w(t, z; I_{st})$, is determined, the wind step force response, $q_d(t, z; I_\tau)$, and the slope step force response, $q_s(t, z; I_{\nabla\eta})$, can be obtained as

$$q_d(t, z; I_\tau) = \frac{I_\tau}{f\delta_e} \left[SE(z) - \sum_{n=0}^{\infty} a_n e^{-(\gamma_n^2 + i)ft} \cos(\omega_n z) \right] \tag{4.53}$$

$$q_s(t, z; I_{\nabla\eta}) = i \frac{g I_{\nabla\eta}}{f} \left[BE(z) - \sum_{n=0}^{\infty} c_n e^{-(\gamma_n^2 + i)ft} \cos(\omega_n z) \right] \tag{4.54}$$

where $SE(z)$, $BE(z)$, ω_n and γ_n are the same as those given by Eqs. (4.7), (4.8), (4.34), and (4.36). a_n and c_n are the coefficients of Fourier expansions of $SE(z)$ and $BE(z)$

$$a_n = \frac{2}{h} \int_{-h}^{0} SE(z) \cos(\omega_n z) dz \tag{4.55}$$

$$c_n = \frac{2}{h} \int_{-h}^{0} BE(z) \cos(\omega_n z) dz, \tag{4.56}$$

and their detailed expressions will be provided in Chapter 6.

Flows driven by arbitrary winds, waves and slopes are then described by

$$q(t, z) = \tau(t) * \dot{q}_d(t, z; I_\tau) + \mathfrak{R}(t) * \dot{q}_w(t, z; I_{st}) + \nabla\eta(t) * \dot{q}_s(t, z; I_{\nabla\eta}). \tag{4.57}$$

4.5   Comments on the need to include wave stress

In many coastal wind-driven circulation experiments the Coriolis term in the along-shore momentum equation is found to be dynamically large but uncorrelated with the other first order terms (Allen and Smith, 1981; Pettigrew, 1981; Lentz and Winant, 1986; Masse, 1988; Lee, et al., 1989) . The data listed in Table (4.1) cited from Lentz and Winant may illustrate this imbalance.

The cause of the force imbalance has been attributed to instrumental noise (Lentz and Winant, 1986) and to small scale alongshore pressure gradients (Pettigrew, 1981), but basically remains a puzzle. The Coriolis-induced wave stress may offer a partial explanation for the imbalance. Generally, near the coast there is a shoreward propagating wave component. According to Eq. (4.24), there will be an Eulerian return flow in the water column induced by this wave component. The recorded current will certainly include this return flow, while the external forcing (the surface wave field) would not normally be considered in these experiments. Thus an apparent imbalance arises. A wave of 10 second period and $1.26m$ amplitude is sufficient to account for the uncorrelated term $f\{u\} = 5 \times 10^{-5} m^2 s^{-2}$ in Table (4.1).[1] This suggests a need for studies of shelf dynamics to include wave forcing, which has to date usually been neglected.

The wave forcing has an interesting dependence on bottom topography. This is seen in two ways. One is that the function $\sinh kh$ (or the like) appears explicitly in the wave forcing. Another is due to the wave shoaling and refraction processes that a train of waves will experience, resulting from the wave group velocity and phase velocity being functions of water depth. Both of these processes will result in a change in wave heights. The wave heights directly affect the size of wave forcing

---

[1]Table (4.1) corresponds to the mooring line at water depth of 60 m in Lentz and Winant experiment. There were 5 to 8 current meters, depending on the different times of deployment, about evenly spaced along the line. The top few current meters were deployed at 5, 7, and 13m depth. For the above chosen 10 second wave, the Stokes depth is 12m. Thus the top few current meters should sense the wave-induced Eulerian return flow. Note that listed in Table (4.1) are the depth integrated values. The depth integrated Stokes drift of the chosen wave is $f \times a^2 \sigma/2 = 5 \times 10^{-4} m^2/s^2$, when the above chosen values of the wave amplitude and wave frequency and $f = 10^{-4}$ are substituted in.

Table 4.1: Alongshore momentum imbalance in a coastal experiment (Lentz and Winant 1986). The notation { } represents depth integration, and F represents the divergence of the longshore component of the horizontal Reynolds' stress.

Terms	$(10^{-5}m^2s^{-2})$
$\{v\}_t$	5
$\{uv\}_x, \{v^2\}_y$	1
$f\{u\}$	≤ 5
$gh\eta_y$	5
$\left\{\int_z^{\eta'} \frac{g}{\rho_0} \frac{\partial \rho}{\partial y} dz'\right\}$	1
τ^s	5
τ^b	5
$\{F\}$	0.2

as can be seen above. The refraction process also results in a tendency for the wave front to become parallel with depth contours. In contrast, the wind forcing is totally independent of the sea bottom topography. Further exploration of this unique feature of wave forcing is not presented here, but would be interesting.

4.6 Summary and discussion

Wave forcing has been examined for the case of a rotating viscous fluid of finite depth. A simple Eulerian model is presented to accommodate wave forcing in addition to wind forcing. The model yields a general formula for the wind- and wave-driven flow for both steady and unsteady forcing, for arbitrary but constant water depth and for arbitrary wave direction. The solution for wave-driven steady flow recovers Longuet-Higgins' (1953) wave mass transport theory in the limit $f \to 0$, and recovers Ursell's (1950) and Hasselmann's (1970) zero mean theory when the limit $\nu \to 0$ is taken. In the deep water limit, it becomes the Eulerian counterpart of Madsen's Lagrangian solution in deep water.

The effect of surface waves on the mean flow is twofold. One is a wave-induced body force distributed mainly within a Stokes depth from the surface. It arises from

the earth's rotation. The second one is the wave-induced virtual shear stress at the sea surface and wave-induced streaming at the bottom. It is due to fluid viscosity. By adopting an Eulerian viewpoint, these two wave effects can incorporated into a classical geophysical fluid dynamic problem as demonstrated by this chapter.

The size of the wave-driven flow close to the sea surface is typically comparable to that driven by winds. For large swells, the wave-driven flow can be very significant. With inclusion of the wave stress, some problems confronting us such as alongshore momentum imbalance found in many coastal experiments of wind driven circulation may be resolved.

The solutions obtained here are local solutions in the same sense that the Ekman transport due to the wind is a local result. In deeper water, the inviscid solution in which the Stokes drift is exactly balanced by an upwave Eulerian current (Fig. 4.3b), provides a reasonable first approximation for the solution including viscosity. However, the inclusion of the viscous terms leads to a net transport in both downwave and along-crest directions. In infinitely deep water, the fluxes (only in along-crest direction) are small compared to typical Ekman transports (Weber and Melson, 1993b). However, in finite depth the transports associated with the bottom boundary layer become increasingly important (Fig. 4.1), giving significant depth integrated flows in the wave direction and to the right of the wave direction (in the Northern hemisphere). A full regional solution then needs a mass balance condition imposed by appropriate boundary conditions. There is then the possibility of strong local flows associated, for example, with large swell propagating over complex shallow topography, analogous to the rip-currents in nearshore circulation patterns.

Chapter 5

An Exploration of the CASP Data

5.1 Introduction

Since 1970, when Hasselmann proposed the concept of the Coriolis-induced wave stress, research in this area has remained theoretical. There are few field observations suitable for testing the theory. The CASP (Canadian Atlantic Storm Program) data set includes both high frequency surface wave observations and low frequency current observations on the Scotian Shelf for the winter of 1985–86. The main purpose of this experiment was to understand how sea level and currents on the shelf respond to the synoptic and mesoscale forcing by wind storms. Wave observations were included in the experiment for the study of wave generation by winds, not to identify the current generation by waves. However, some of the observational wave data may be suitable for testing wave generated currents. This chapter, therefore, explores the CASP data set for evidence of the effects suggested by the theory of Chapters 2 and 4.

5.2 The CASP experiment and mooring array

During the winter of 1985 and 1986, observations of sea surface elevation, currents, bottom pressure, and water properties, as well as the wind were made on the Scotian Shelf as part of CASP. Figs. (5.1), and (5.2), from Lively (1988) indicate 11 stations

at which currents and bottom pressure gauges were deployed. There were also observations of surface waves by 9 wave buoys deployed in the vicinity of Stations 1, 2, 6 and 7. Three of the wave buoys were directional Datawell WAVEC buoys, recording wave heights and directions, while the others were non-directional Datawell waveriders, recording only wave heights. The buoys recorded the wave data at a sampling frequency of 1.28 Hz for the first 30 minutes of each hour. During the last 30 min of each hour, estimates of wave energy spectra and surface slope-heave cross-spectra were automatically computed and telemetered to the Bedford Institute of Oceanography. A detailed description of the CASP experiment can be found in Anderson and Smith (1989). For the wave observations and the wave modelling, reference is made to Dobson and Toulany (1989).

5.3 Methods for the exploration

According to the theory presented in Chapter 4, the currents observed at fixed mooring lines are driven by winds, waves, and pressure gradients. As has been shown by Eq. (4.57), the flow within a water column driven by these three forces is

$$q(t,z) = \tau * \dot{q}_d(t,z; I_{st}) + \mathfrak{R} * \dot{q}_w(t,z,; I_{st}) + \nabla\eta * \dot{q}_s(t,z; I_{\nabla\eta}). \qquad (5.1)$$

In the above, $\dot{q}_d$, $\dot{q}_w$ and $\dot{q}_s$ are the response kernels. The eddy viscosity is an unknown parameter in these kernels. If the value of the eddy viscosity were known, then the kernels would be determined. If the forces are supplied, then the velocity can be calculated.

How does one get a proper value for the eddy viscosity? A usual practice in numerical modelling is to simply guess a value for the eddy viscosity and run the model. A comparison of the model output with observations is then used to adjust the guessed value and the model is run again. This process continues until a satisfactory value of the viscosity is found. This chapter, instead, uses a statistical model for estimating a best fitting value of eddy viscosity. The statistical model is as follows

$$q(t,z) = C_1(z)\tau(t) + C_2(z)\mathfrak{R}(t) + C_3(z)\nabla\eta(t) + \varepsilon(t) \qquad (5.2)$$

41 km
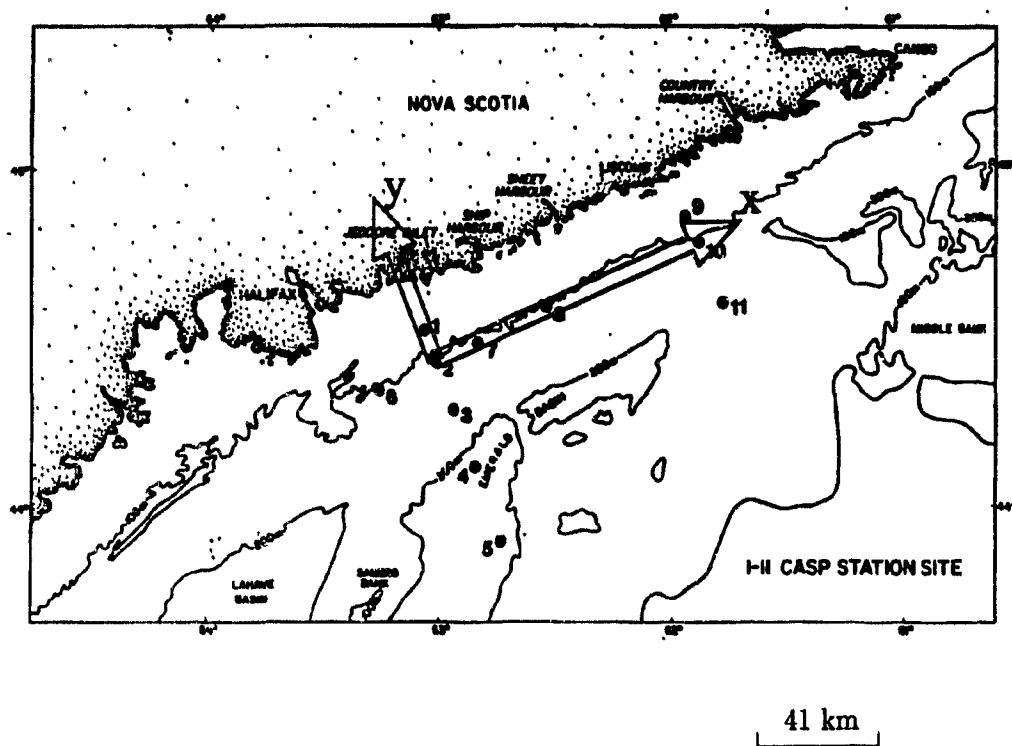
Figure 5.1: CASP station locations (modified from Lively 1988). The alongshore direction, which is 67.75° from north, is defined as the x-axis and the cross-shore as the y-axis.
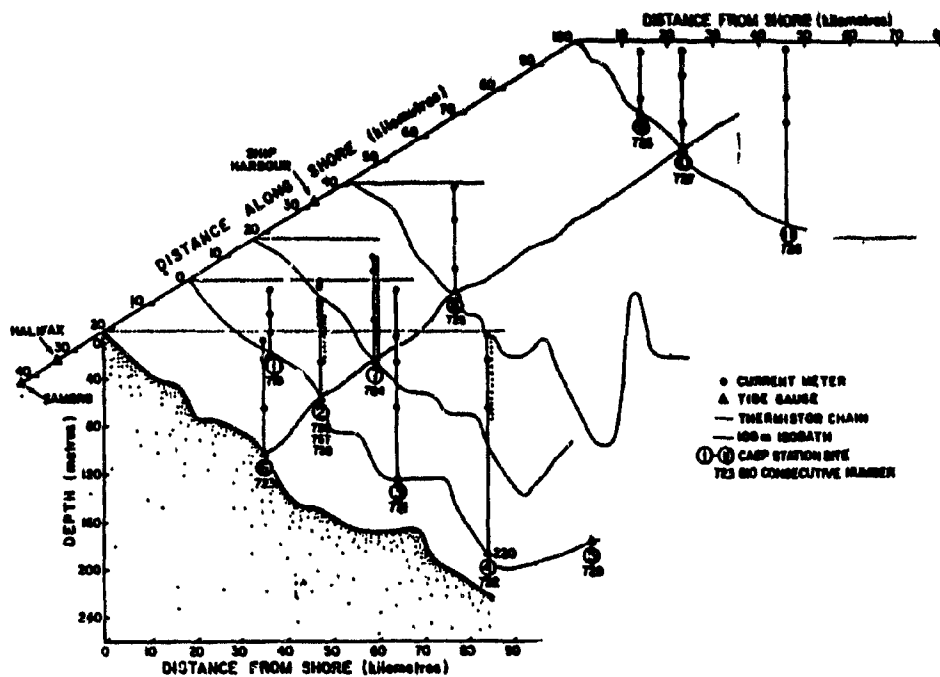
Figure 5.2: A 3-D sketch of the CASP instrument deployment (from Lively 1988)

where $\varepsilon(t)$ represents noise and other possible signals that a simple linear model may not be able to resolve, and C_1, C_2, and C_3 are complex valued coefficients to be determined from the data. As will be shown, the angle of C_1 can yield an estimate of the eddy viscosity. The regression model can also provide a hypothesis testing to check if these coefficients are significantly different from zero.

The connection between the statistical model and the numerical model is made as follows. Following Appendix A to this chapter, Eq. (5.1) can be rewritten as

$$
\begin{aligned}
q &= \left\{ \frac{\text{SE}(z)}{f\delta_e}\tau(t) + \frac{1}{f\delta_e}\frac{\partial\tau(t)}{\partial t} * \sum_n a_n \cos(\omega_n z)e^{-b_n t} + \frac{\tau(0)}{f\delta_e}\sum_n a_n \cos(\omega_n z)e^{-b_n t} \right\} \\
&+ \left\{ \text{WA}(z)\mathcal{S}(t) + \frac{\partial\mathcal{S}(t)}{\partial t} * \sum_n s_n \cos(\omega_n z)e^{-b_n t} + \mathcal{S}(0)\sum_n s_n \cos(\omega_n z)e^{-b_n t} \right\} \\
&+ \left\{ i\frac{g\text{BE}(z)}{f}\nabla\eta(t) + i\frac{g}{f}\frac{\partial\nabla\eta(t)}{\partial t} * \sum_n c_n \cos(\omega_n z)e^{-b_n t} \right. \\
&\qquad\qquad\qquad \left. + i\frac{g\nabla\eta(0)}{f}\sum_n c_n \cos(\omega_n z)e^{-b_n t} \right\}.
\end{aligned}
\tag{5.3}
$$

The terms on the RHS are grouped in terms of forces. Each group is comprised of three terms: the first term is the response to present time force, the second term is the response to past time forces, and the third term accounts for the effects of the initial force. Obviously, the third term will become trivial when t becomes sufficiently large. The second term describes the importance of the time rate of change of the forcing in the present time response. The first term is the steady response, since this is the response one would obtain if the time derivative terms from the governing equations were initially dropped.

The regression model of Eq. (5.2) thus represents the steady response of the numerical model. For this reason, the statistical model is also a steady model. According to Eq. (5.3), the regression coefficients, C_1, C_2 and C_3 should represent $\text{SE}(z)/f\delta_e$, $\text{WA}(z)$ and $ig\text{BE}(z)/f$ respectively. The appropriateness of a steady regression model depends on size of the effect of the time rate of change of the forcing. Thus, a low-pass filtered forcing can be expected to have a smaller effect of its past values on the present response. For now, let it be assumed that the steady regression model is

appropriate. (Later, the results of a numerical model will show the effect of neglecting the second term in each of the curve brackets on RHS of Eq. 5.3, cf. page 93, and Figs. 5.15, 5.16, 5.17.)

The approach is as follows. First, the regression model is applied to the observed data to estimate the eddy viscosity, and significance tests are performed on the chosen predictors. Then, the estimated eddy viscosity is input into the numerical model to simulate the observed flow. Initially however, we need to prepare the time series of both the forcing functions and the response from the observations.

5.4 Time series preparation

5.4.1 The wave force $\mathcal{S}(t)$

During CASP, hourly wave spectra were automatically computed and telemetered by the wave buoys. From the hourly spectra, time series for various wave parameters of interest can be calculated. The surface Stokes value $\mathcal{S}(t)$ has been defined by Eq. (2.18). Here let it be denoted by $\mathcal{S}(t)$, i.e.,

$$\mathcal{S}(t) = a^2\sigma k e^{i\theta}\frac{\cosh 2kh}{2\sinh^2(kh)}. \tag{5.4}$$

To calculate $\mathcal{S}$, the wave parameters a, θ, and σ are needed.

Define half of the significant wave height $\mathrm{HS}(t)$ as the wave amplitude, i.e.,

$$a(t) = \frac{\mathrm{HS}(t)}{2} = \sqrt{\frac{2}{\pi}\int_0^\infty S(\sigma)d\sigma} \quad \left(=\sqrt{\frac{2}{\pi}}\text{Variance of the waves}\right). \tag{5.5}$$

(Earle and Bishop, 1979) where $S(\sigma)$ is the wave energy spectrum of the waves. Further, define the peak wave direction (peak here refers to the peak of the curve of the wave spectra versus wave direction), as the wave direction $\theta(t)$. Finally choose a single wave frequency of 0.1 Hz. for σ. Choosing a fixed frequency simplifies the situation since the formula for the wave-driven flow derived in the preceding chapter is for a monochromatic wave, and observations show that 0.1Hz is representative of the swells

in the region (Fig. 5.3). Thus, the observed wave field is approximated by a single representative wave whose frequency $\sigma = 2\pi/10$, amplitude and direction change through time. Dr. F. Dobson and B. Toulany of the Bedford Institute Oceanography kindly supplied the wave parameters (Fig. 5.4).

Shown in Fig. (5.5) is the time series of $\mathcal{S}(t)$ at Station 2 calculated from the wave parameters. In the conversion from the wave parameters to the Stokes drift, the following procedures have been used:

- Conversion of the "from"-direction of waves with respect to the North clockwise to the "to"-direction with respect to the x-axis (which is alongshore direction, ~ 67.75 deg True North) anticlockwise;

- Low pass filtering with zero phase distortion. The filter, as is shown in Fig. (5.6), is designed to remove residual tidal signals in the current time series. For consistency in processing the data, the other time series are also filtered using this low pass filter.

- Removal of the mean value of the drift.

5.4.2 Wind stress $\tau(t)$

Wind data from two sites are used: Minimet wind buoy near Station 2 (Fig. 5.1) and Shearwater, a permanent land weather station located about 30 kilometers inshore of Station 2. The wind record obtained by the Minimet at sea is short and segmented due to ice clogging problems. A linear relationship between the Minimet data and the Shearwater data allows the data to be extrapolated and interpolated to cover the time span desired.

The wind velocity data were converted to wind stress by

$$\tau_i = \frac{\rho_a}{\rho} C_d W W_i \tag{5.6}$$

where τ_i is the kinematic wind stress, W is the wind speed and W_i is the wind velocity component, ρ_a is the air density, and ρ is the sea water density, (in this study, the
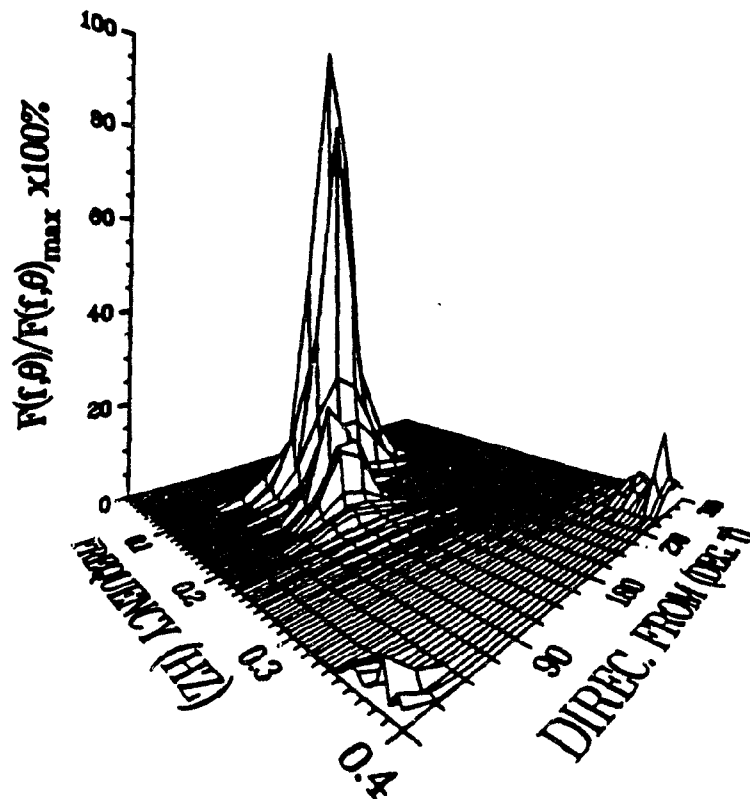
Figure 5.3: An example of the observed 3-D wave energy spectrum. The well defined peak around the frequency 0.1 Hz corresponds to the swell (courtesy of F. Dobson and B. Toulany).
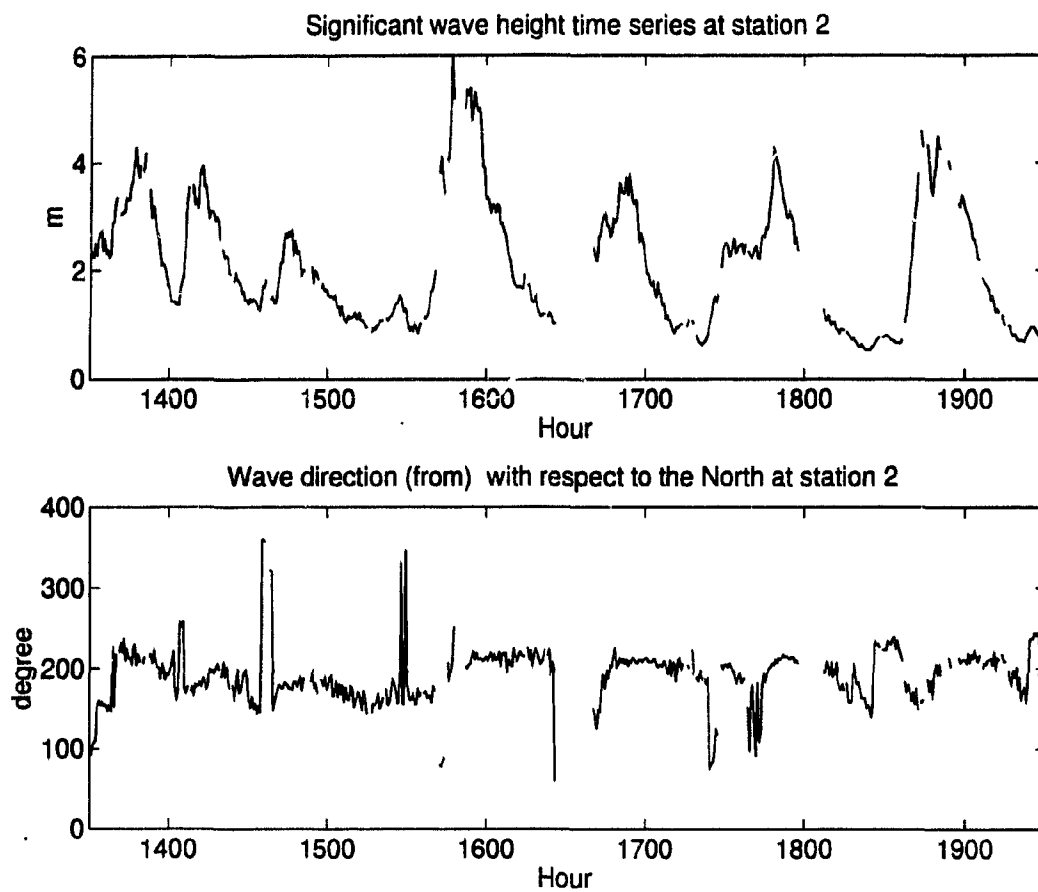
Figure 5.4: Significant wave height and wave direction history at Station 2. The missing data are due to ice clogging the wave buoy and telemetry failure. (The hours are counted from 00:00 Jan.1, 1986, which is regarded as the zero hour throughout this chapter.)
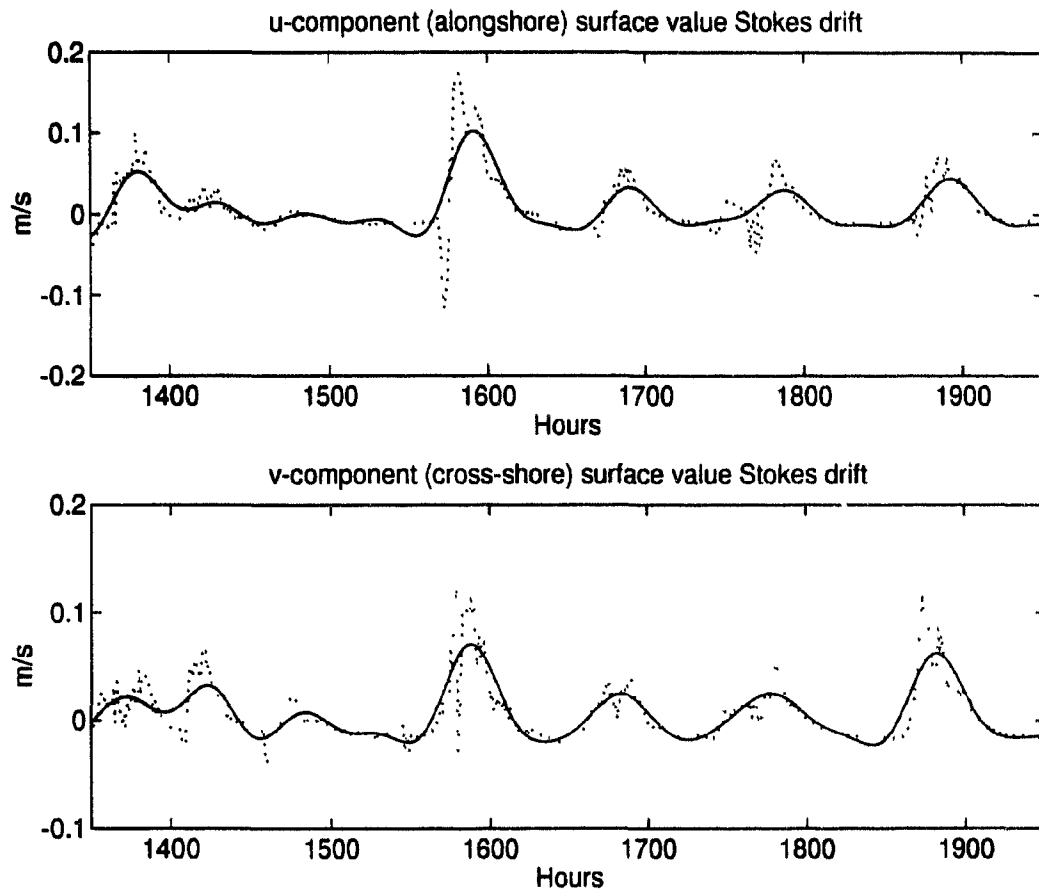
Figure 5.5: u and v components of the Stokes drift time series. The dotted lines are unfiltered series, and the solid lines low pass filtered.

2 OF/DE 2

PM-1 3½"x4" PHOTOGRAPHIC MICROCOPY TARGET
NBS 1010a ANSI/ISO #2 EQUIVALENT

1.0

4.5 2.8 2.5
     3.2 2.2
     36
     4.0 2.0

1.1

1.8

1.25 1.4 1.6
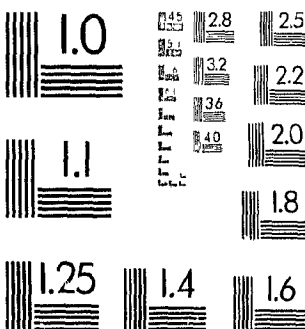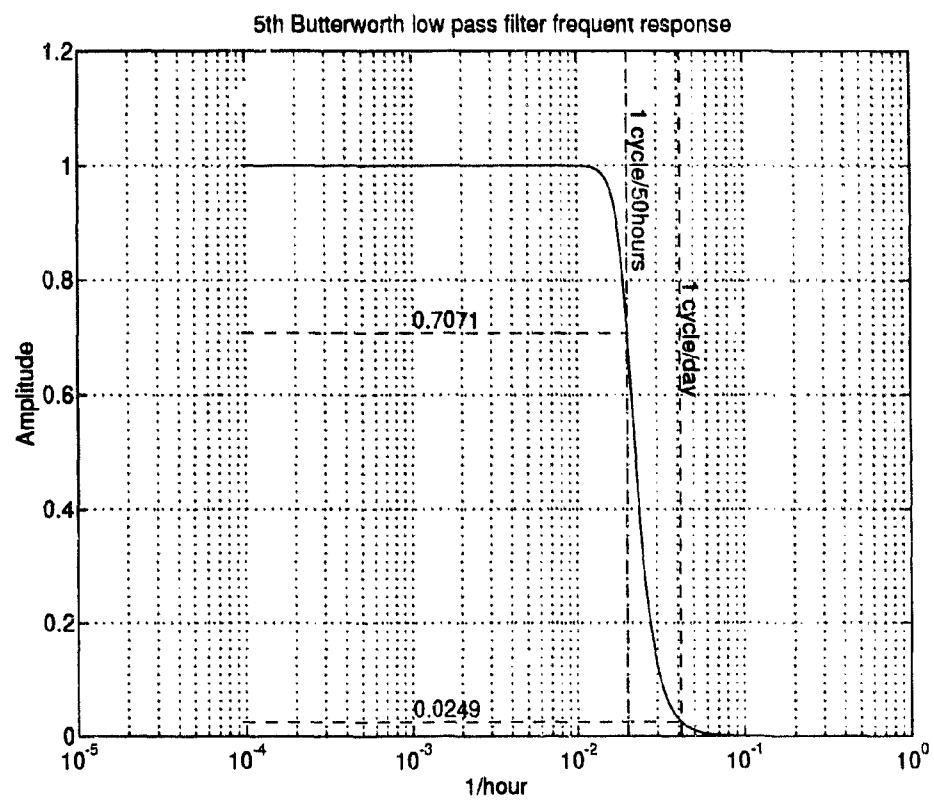
Figure 5.6: The frequency response of the filter used in this data analysis.

ratio of the two densities is taken to be $1.25 \times 10^{-3}/1.025$). C_d is the drag coefficient, which is a step function of the wind speed

$$C_d = \begin{cases} 1.6 \times 10^{-3} & (W \leq 7m/s) \\ 2.5 \times 10^{-3} & (W \geq 10m/s) \end{cases} \qquad (5.7)$$

with a smooth transition for intermediate wind speed (eg., Csanady, 1982). In the calculation, the wind direction has been converted from the "from"-direction with respect to true North to the "to"-direction with respect to the alongshore direction. The wind stress time series is shown in Fig. (5.7) (after the low pass filter has been applied, cf. Fig. 5.6).

5.4.3 The sea surface gradient time series $\nabla \eta(t)$

For a barotropic linear flow, the information required to complete the dynamic field is the surface slope $\nabla \eta$. Its value at a fixed mooring line may be calculated from bottom pressure gauge data if, ideally, there are four bottom gauges deployed around it in a "+" configuration. For reasons that will become clear in the next subsection, the current data from the mooring at $z = -4m$ of Station 8 will be chosen as the response time series. At this station, however the calculation of the pressure gradient from the observations is difficult because there were not four bottom pressure gauges deployed nearby. (In the cross-shore direction, no adjacent bottom pressure gauges were deployed. In the alongshore direction, the two most adjacent Stations, 7 and 10, were too far apart from Station 8). While the alongshore component of the pressure gradient may be assumed to be negligibly small, the cross-shore component must be considered in a near shore region. Fortunately, Station 8 lies between the two cross-shore lines, the Halifax line and the Liscomb line, where there are enough bottom pressure gauges for calculating the cross-shore pressure gradients at Station 2 and Station 10. With the information obtained at these two stations, the cross-shore pressure gradient for Station 8 can then be inferred by linear interpolation,

$$\left.\frac{\partial \eta}{\partial y}\right|_{s4} = \frac{57.08}{98.60} \left.\frac{\partial \eta}{\partial y}\right|_{s2} + \frac{41.52}{98.60} \left.\frac{\partial \eta}{\partial y}\right|_{s10}, \qquad (5.8)$$
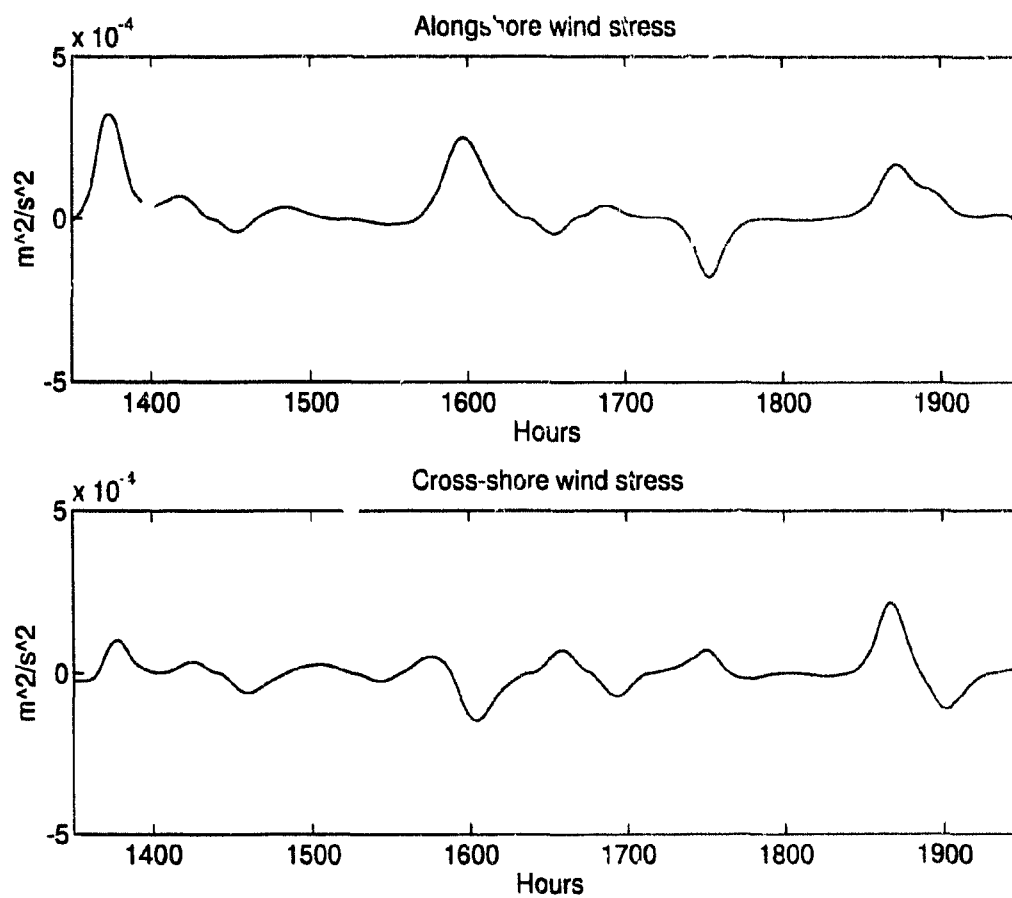
Figure 5.7: Time series of the along and cross-shore wind stress

in which the distance between the three stations have been used as weights (Fig. 5.1) and

$$\frac{\partial \eta}{\partial y}\bigg|_{s2} = 0.9945 \left(\frac{BP_{719} - BP_{720}}{\Delta y} \right)_{s2} \qquad (5.9)$$

$$\frac{\partial \eta}{\partial y}\bigg|_{s10} = 0.9945 \left(\frac{BP_{726} - BP_{727}}{\Delta y} \right)_{s10}, \qquad (5.10)$$

where the factor 0.9945 is used to convert the decibar of BP data to the hydrostatic head in meters (assuming $g = 9.81m/s^2$ and $\rho = 1025kg/m^3$). In the calculations, the mean values of BPs are all removed. Thus the hydrostatic head η converted from BPs can be regarded as the sea surface elevation in the usual sense, measured from mean sea level with positive upwards.

Shown in the top and middle panels of Fig. (5.8) are time series of $\partial \eta/\partial y|_{s2}$ and $\partial \eta/\partial y|_{s10}$. The third panel is the interpolated cross-shore pressure gradient for Station 8. Also shown in the top panel is the alongshore component of the pressure gradient at Station 2 calculated from the bottom pressure data at Stations 7, 2 and 6. The maximum absolute value of this component is 13 times smaller than its cross-shore counterpart, confirming the assumption about it being negligibly small.

5.4.4 The response time series

The time series of current meter data provides the response time series. Since the effect of surface waves on the current is of concern here, data from a shallow current meter are chosen for analysis. For 10 second waves in water depth of 100 m, the Stokes depth is $12m$; below this depth the mean wave effects are expected to be weak. For example, Fig. (5.9) shows the current profile driven by 10 second waves for an Ekman depth of $7m$ and Stokes depth of $12m$ in water of total depth 100m. (The choice for this value of the Ekman depth is based on a regression analysis which appears later.) The figure indicates that the magnitude of the wave-driven flow $20m$ below the surface is about 1/5 the surface value of the Stokes drift, and Fig. (5.5) shows that the surface Stokes drift is less than $10cms^{-1}$. Therefore, if the data around
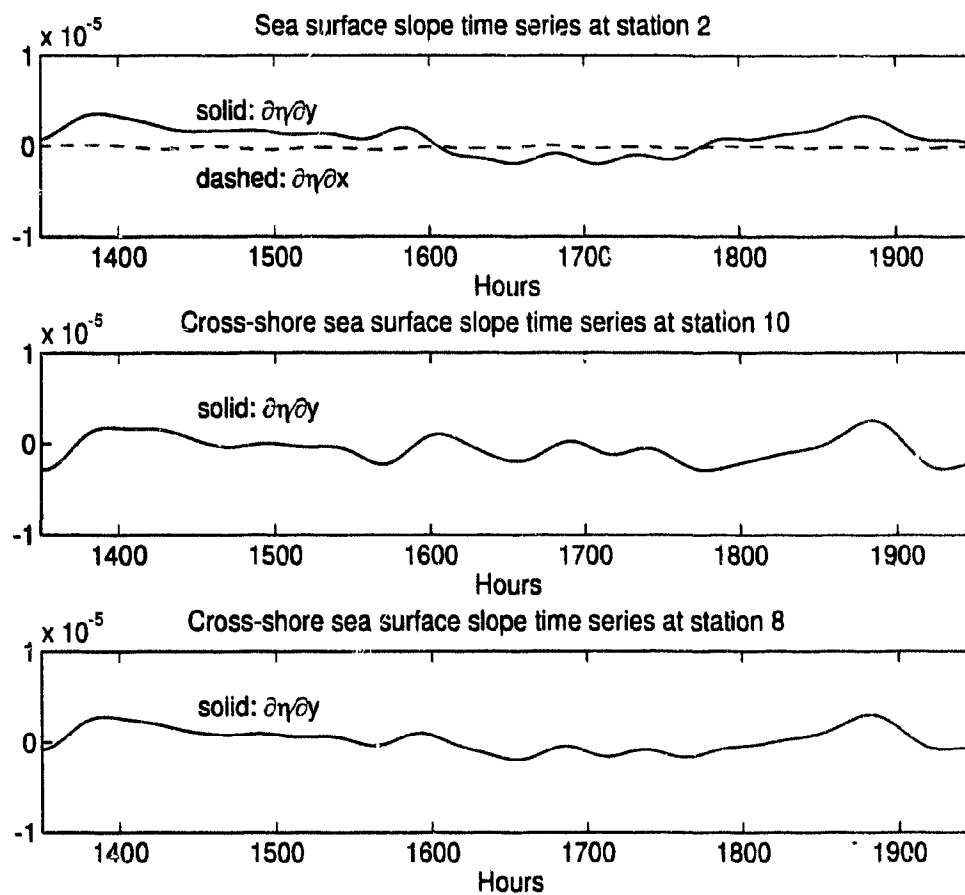
Figure 5.8: The time series of the pressure gradients at three stations. The gradient at Station 2 and that at Station 10 are directly calculated from the records of the bottom pressure gauges. The gradient at Station 8 is a linear interpolation of those at Station 2 and Station 10.

the depth of 20m is analyzed, the signal will be $2cms^{-1}$ at the maximum, difficult to separate from noise.

At Station 2. two shallow current meters were deployed at depths 2.6m and 5m, which would be ideal for our purpose. However, they failed to function. The next shallowest one available at Station 2 is at 18 m, which is too deep for the reasons stated above. Along the 100 m depth contour, the current meter which was both within the Stokes depth and produced a complete data set is the one at a depth $4m$ at Station 8. For the following analysis, therefore, data from this meter will be used as the response time series.

A necessary assumption is then that the winds and waves observed around Station 2 were uniform over to Station 8, which is about $40km$ away. For the winds, this assumption is reasonable because typical spatial scales are larger than $40km$. The waves of 10 second period in water depth of $100m$ can be regarded as deep water waves and their scales of spatial uniformity should be of the same order as that of the wind (which generates the waves). For the cross-shore pressure gradient, values interpolated between Station 2 and Station 10 have already been calculated.

In processing the current data, a tidal model is employed to separate the tidal and non-tidal signals. After detiding, the low pass filter (Fig. 5.6) is used to remove high frequency noise and any residual tidal signals left over from the detiding. Note, to extract the non-tidal signal, one could simply use a low pass filter directly. However, the tidal analysis reveals that the tidal current of the lunar fortnightly constituent, Mf, is not negligible. Hence, if a low pass filter is employed for detiding, then its cutoff frequency should be set low enough so that the Mf constituent is removed. If this is done, the interesting signals with frequencies higher than Mf ($\sim$ 1/13.66 cycle/day) will also be removed. Obviously, this is not desirable.

Presented in Fig. (5.10) is the detided and low pass filtered current time series at $4m$ depth of Station 8. This time series will be taken as the response function for the regression analysis in the next section.
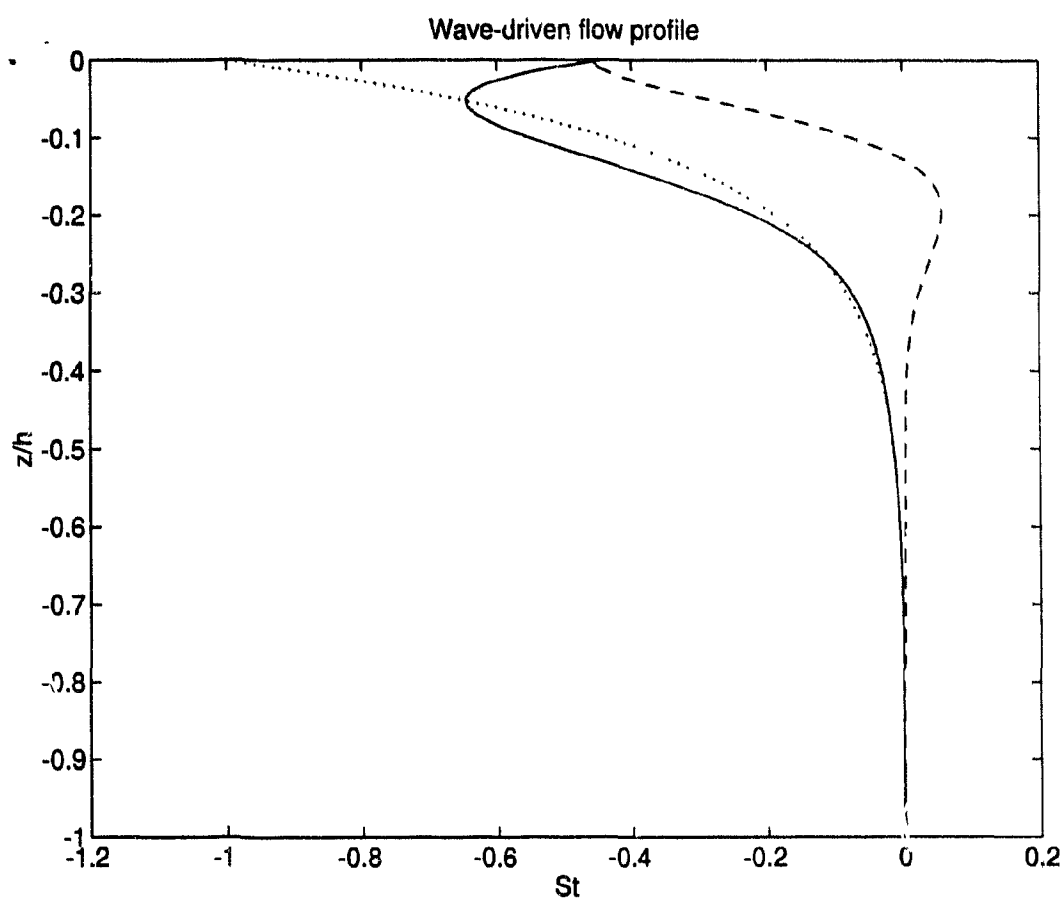
Figure 5.9: The wave-driven flow profile with the parameter values of $\delta_c/h = 0.07$ and $\delta_{st}/h = 0.12$. The dotted line is the wave-driven Eulerian inviscid flow, the solid line the upwave direction (opposite to the direction of wave propagation) the component of the wave-driven Eulerian flow, the dashed line is the along wave-crest component.

Detided and low pass filtered velocity of u-component (alongshore)

Detided and low pass filtered velocity of v-component (cross-shore)
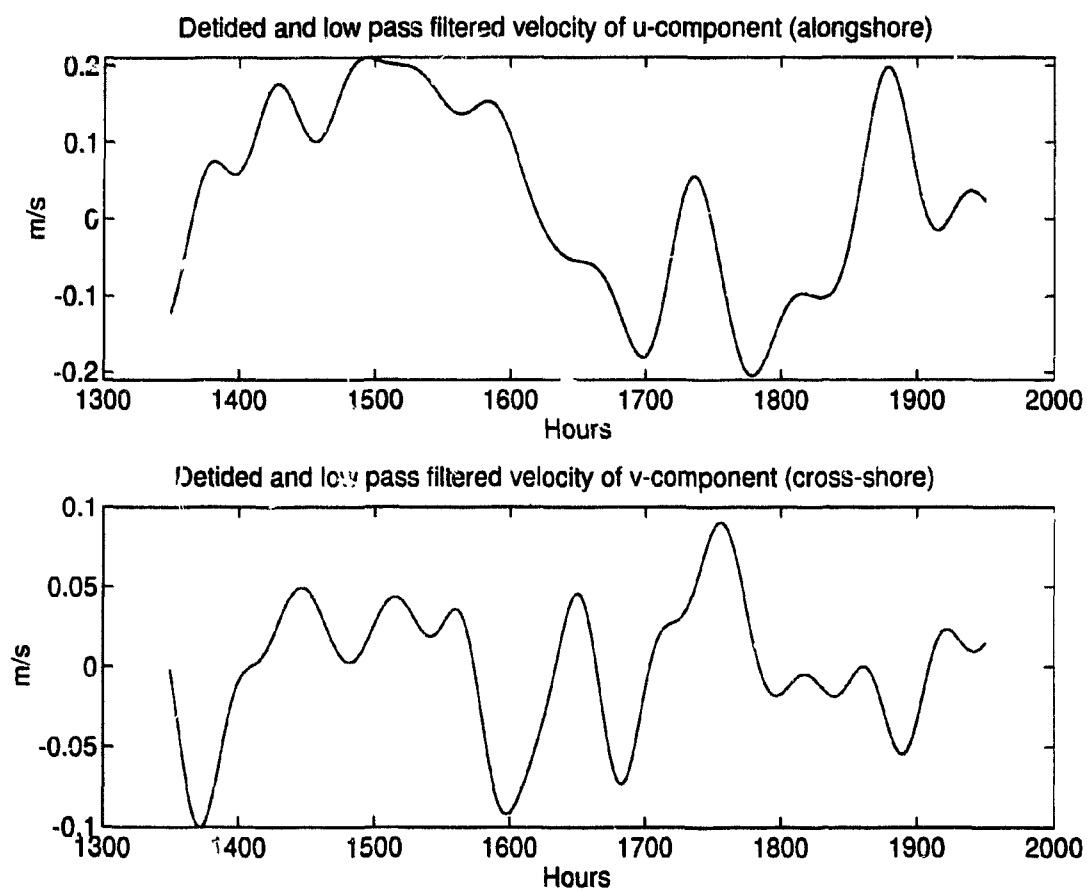
Figure 5.10: The time series of the velocity components at $z = -4m$ of Station 8.

5.5 Regression analysis

In Section 5.4, all the time series needed for the regression model of Eq. (5.2) are prepared. The least squares estimates of the regression coefficients are given by (e.g., Seber, 1977)

$$[\hat{C}_1 \ \hat{C}_2 \ \hat{C}_3]^T \ = \ (\mathcal{H}^T\mathcal{H})^{-1}\mathcal{H}^T q \tag{5.11}$$

where q is the vector of observed complex velocity, hats denote estimates and $\mathcal{H}$ is an $n \times 3$ matrix

$$\mathcal{H} \ = \ [\tau(t_i) \ \mathcal{S}(t_i) \ \nabla\eta(t_i)] \qquad i = 1, 2, \cdots n \tag{5.12}$$

where n is the number of observations. Before substituting in the tii. series to obtain the values of the estimates, it is useful to recall some of the properties of the estimates for later discussion.

- When the noise term ε in the model Eq. (5.2) has zero mean, i.e., $E[\varepsilon(t)] = 0$, the estimates are unbiased,

$$E[\hat{C}_1 \ \hat{C}_2 \ \hat{C}_3] = [C_1 \ C_2 \ C_3], \tag{5.13}$$

where the notation E denotes the expectation operator.

- Furthermore assuming that the noise is uncorrelated, normal distribution with constant variance, i.e., $\mathrm{Cov}[\varepsilon_i\varepsilon_j] = \delta_{ij}\sigma^2$, the following three statistics have an F-distribution with degrees of freedom of 1 and $n - 4$,

$$F_i \ = \ \frac{|\hat{C}_i - C_i|^2/d_{ii}}{\mathrm{RSS}/(n-4)} \qquad i = 1, 2, 3 \tag{5.14}$$

where d_{ii} stands for the ith diagonal component of matrix $(\mathcal{H}^T\mathcal{H})^{-1}$. RSS stands for the residual sum of squares

$$\mathrm{RSS} \ = \ (q - \hat{q})^T(q - \hat{q}) \tag{5.15}$$

in which

$$\hat{q} \ = \ \mathcal{H}[\hat{C}_1 \ \hat{C}_2 \ \hat{C}_3]^T. \tag{5.16}$$

The statistic F_i can be used for testing significance of the estimated coefficients against the null hypothesis $C_i = 0$ in Eq. (5.14). (The properties can be found in most statistics books, e.g., Seber, 1977.)

The condition that the errors have zero mean is relatively easy to satisfy, since the mean values of all the time series have been removed (the time series are understood to be ergodic). Although the further condition that errors are uncorrelated is assumed by the second property, whether this condition can be satisfied or not is unclear. Besides the usual white noise, the errors may contain some slowly varying process which may be auto-correlated on lag times of a few hours. Any such auto-correlation will result in overestimation of the degrees of freedom of the data set, and the confidence level for the estimated coefficients will thus be in doubt. One way to address the confidence level problem when little is known about the underlying error processes is to resort to Monte Carlo simulations of synthetic data sets. Press *et al* (1992, section 15.6) have described the philosophy behind this method. Based on their idea, a technique involving Monte Carlo simulation will be used to estimate confidence levels. For future reference we will refer to this technique as the "clone" technique. In what follows, the error processes will initially be assumed to be uncorrelated. Based on this assumption, the usual linear regression analysis and the null hypothesis test will be carried out. The "clone" technique will then be used as an independent means (independent of our assumptions about the error statistics) to check the confidence level.

5.5.1 Regression results and an estimate of the Ekman depth

The time series prepared above are 601 points long with a one hour sample interval. Shown in Table (5.1) and Fig. (5.11) are the regression results. The values of F_i in Table (5.1) indicate that the three estimated coefficients pass the null hypothesis test at the 5% significance level. (The critical F-value is shown in the caption of the table.) While this seems encouraging, the question whether the condition $\text{Cov}[\varepsilon_i \varepsilon_j] = \delta_{ij}\sigma^2$ is satisfied cannot be answered. For this reason, the "clone" technique will be used.

Table 5.1: The regression analysis results for q_{04} at Station 8 (total 601 hourly samples). The critical value of $F_{0.05}(1,597) = 3.81$.

	τ	$\mathcal{A}$	$\nabla\eta$
q_{04}	$|\hat{C}_1| = 257.68$ $F = 22.73$ $\tan^{-1}\hat{C}_1 = -77.47°$	$|\hat{C}_2| = 0.61$ $F = 17.91$ $\tan^{-1}\hat{C}_2 = -176.31°$	$|\hat{C}_3| = 5.99 \times 10^4$ $F = 300.12$ $\tan^{-1}\hat{C}_3 = 91.58°$

However, first the discussion is focused on the angles of the complex $\hat{C}$, listed in the table.

According to barotropic linear theory, the pressure gradient driven flow near the surface in relatively deep water should be nearly geostrophic, i.e., the flow should lead the force by about 90° (notice the pressure gradient direction is defined from low pressure to high pressure). The corresponding angle of $\hat{C}_3$ listed in the table is very close to the theoretical value. According to the wave-driven flow theory presented in Chapter 2, the wave driven inviscid flow should be 180° opposed to the wave direction; when the viscid effect is taken into account, this angle will be somewhat less than 180°. The angle of $\hat{C}_2$ listed in the table meets this expectation. Knowing the value of δ_e/h will help to determine the theoretical angle for $\hat{C}_2$ at the mooring depth of $4m$.

From the angle of $\hat{C}_1$ (with respect to the direction of wind stress), the thickness of the Ekman layer may be inferred as follows. The direction factor for the wind-induced flow is

$$e^{-i\left(\frac{\pi}{4}+\frac{|z|}{\delta_e}\right)},\tag{5.17}$$

(where for simplicity, $\sinh\alpha(h+z)/\cosh\alpha h$ has been approximated by $e^{\alpha z}$ for the depth of $h = 100m$, where $\alpha = (1+i)/\delta_e$) therefore.

$$\frac{\pi}{4}+\frac{|z|}{\delta_e} = \frac{\tan^{-1}\hat{C}_1}{180}\pi \pm 2k\pi \qquad (k = 0,\ 1,\ 2,...)\tag{5.18}$$

(where one should chose the smallest k still keeping $|z|$ positive). Substitution of the

u-components

v-components
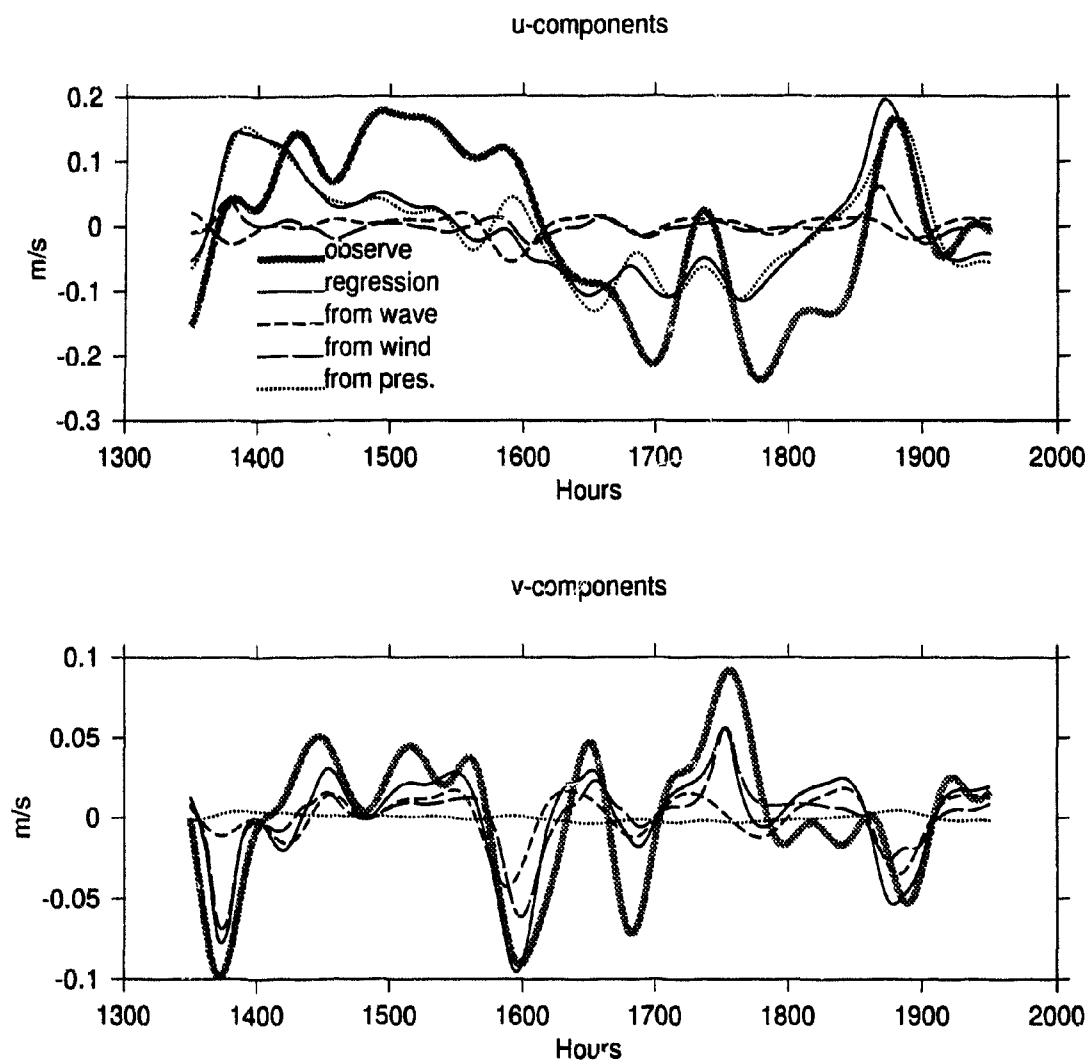
Figure 5.11: The regression analysis results for currents at $z = -4m$ at Station 8. The upper panel is alongshore direction, and the lower panel is cross-shore direction.

value for $\tan^{-1} \hat{C}_1$ listed in Table (5.1) and using $z = 4m$ results in an estimate of

$$\delta_e \approx 7m \qquad (5.19)$$

which corresponds to $\nu = 2.5 \times 10^{-4} m^2/s$ at latitude 44.5°N. For a wind stress of the order of $10^{-4} m^2 s^{-2}$, which is the size for CASP wind data, Csanady (1982, page 12) gave an estimate of $10m$ for the Ekman depth, showing the Ekman depth of $7m$ inferred here is reasonable. With the above estimated Ekman depth, Section 5.6 will establish a local numerical model for the flow driven by the three forces. However, as will be shown in that section, substitution of this value of Ekman depth in $|SE(z)/f\delta_v|$ does not give a value close to $|\hat{C}_1|$ listed in Table 5.1.

5.5.2 Clone technique to check the confidence level

The problem of "significance" of $\hat{C}_i$'s is now addressed using the "clone" technique. The "clone" technique involves using Monte Carlo methods to simulate synthetic data. The idea, when it is applied to the case here, can be explained as follows.

The residual sum of squares, RSS, (i.e., the unexplained variance), has been defined by Eq. (5.15). Generally, RSS will decrease (or more precisely, will not increase) when the number of predictors increases. The matrix $\mathcal{H}$ shown by Eq. (5.12) contains three predictors, each of which corresponds to one of its columns. Now consider the drop in RSS when the second column of $\mathcal{H}$ is excluded (the second column corresponds to the wave predictor, which is of interest here). Define this decrease in RSS by

$$DRSS = RSS1\not{2}3 - RSS123 \qquad (5.20)$$

where RSS123 represents the residual sum of squares when $\mathcal{H}$ contains its full three predictors, and RSS1$\not{2}$3 signifies the residual sum of squares when $\mathcal{H}$ contains only its first and third columns. Substitution of the data in Eq. (5.20) results in

$$DRSS = 0.16 \qquad (5.21)$$

(where the units of m^2/s^2 are understood). The idea of the "clone" is to investigate the chance that a random series, when it takes the place of the column of the wave predictor in $\mathcal{H}$, can bring about this value of DRSS. This can be achieved by repeatedly generating a random series, denoted by $\mathcal{R}_r(t)$ say, and replacing the second column of $\mathcal{H}$ by the random series. A sequence of DRSS follows according to Eq. (5.20). A histogram of DRSS can then be constructed, which should tell how large the random chance is.

The random series is created as follows. The given $\mathcal{R}(t)$ function can be represented by it Fourier series,

$$\mathcal{R}(t) = \frac{1}{n}\sum_k \mathcal{F}(\Omega_k)e^{i\Omega_k t} \tag{5.22}$$

where $\mathcal{F}(\Omega_n)$ is the Fourier transform of $\mathcal{R}(t)$,

$$\mathcal{F}(\Omega_n) = |\mathcal{F}(\Omega_n)|e^{i\phi(\Omega_n)}. \tag{5.23}$$

The random series, $\mathcal{R}_r(t)$, is generated by replacing $\mathcal{F}(\Omega_n)$ in Eq. (5.22) by

$$\mathcal{F}'(\Omega_n) = |F(\Omega_n)|e^{i\phi'(\Omega_n)}, \tag{5.24}$$

where the modulus of $\mathcal{F}'(\Omega_n)$ is the same as $\mathcal{F}(\Omega_n)$ but the phase of $\mathcal{F}'(\Omega_n)$ is random. The phase of $\mathcal{F}'(\Omega_n)$ is the phase of the discrete Fourier transform of a purely random time series.

This "clone" technique can be also used to check the wind and the pressure gradient predictors respectively. Presented in Fig. (5.12) is the histogram of DRSS, resulting from 500 simula ons. Panel (a) checks the wind predictor, panel (b) the wave predictor, and panel (c), the pressure gradient predictor. The dashed line on each panel divides the area under the solid curve into two parts. Take panel (b) as an example, the vertical dashed line at the abscissa of 0.16 (cf. Eq. 5.21) divides the area under the solid curve by 57.5% to its left and 42.5% to its right. An interpretation of this areal division is that there is a 42.5% chance that a randomized series can account for more of the observed DRSS. So the "clone" technique yields a 57.5% confidence

level for the wave predictor, 81% for the pressure gradient predictor, and a 52.6% for wind predictor. Compared with the usual regression analysis, the "clone" technique gives lower confidence levels. This perhaps indicates that the degree of freedom in the regression analysis is overestimated.

The correlation of waves and winds may explain the low confidence levels for winds and waves. Presented in Fig. (5.13) is the absolute value of the cross-correlation function of the winds and the waves. The figure shows that the correlation is about 0.61 near lag s=0. As a result of this fairly high correlation between waves and winds, there will not be a significant drop in the RSS when one is added to the other. For comparison, Fig. (5.14) investigates the significance of adding winds or waves alone in addition to the pressure gradient. The figure shows that the drop in RSS due to the addition of winds or waves is almost the same, and their significance level is also nearly the same. Thus, perhaps the high correlation between waves and winds prevents us from distinguishing the separate contributions of waves and winds. For the purpose of testing the theory of wave-driven flow, an experiment conducted in conditions where swells are high but local winds are low would be more suitable.

5.6 Simulation by a local numerical model

The response kernels of $\dot{q}_d$, $\dot{q}_s$, and $\dot{q}_w$ in Eq. (5.3) are determined when a value for Ekman depth is specified. A $7m$ Ekman depth has been estimated above. Although the "clone" technique has revealed a confidence level problem in the estimation, the estimated Ekman depth should not be worse than a subjectively chosen one as is the case in usual numerical modelling practice. The three time convolutions then can be evaluated by using the recursion scheme developed in Chapter 6 (cf., Eqs. 6.42 and 6.78). Presented in Figs. (5.15), (5.16), (5.17) and (5.18) and Table (5.2) are the results of the evaluation.

It has been shown in Section (5.3) that using a steady regression model is reasonable if the size of the second term in each of the braces on the RHS of Eq. (5.3) is
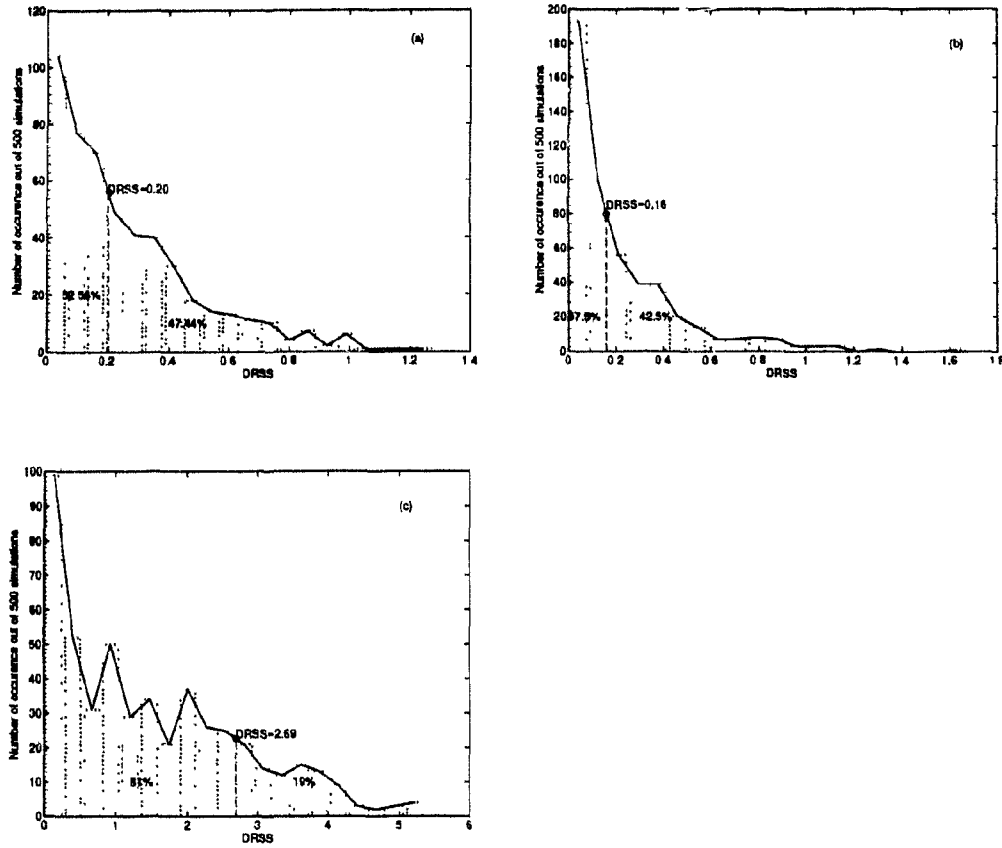
Figure 5.12: Clone technique is used to check the significance of the wind predictor (panel a), the wave predictor (panel b), and the pressure gradient predictor (panel c). In this experiment, the normal matrix $\mathcal{H}$ originally contains three columns (three predictors). When a predictor being examined, the corresponding column of $\mathcal{H}$ is replaced by a column of random data. 500 random time series are simulated.
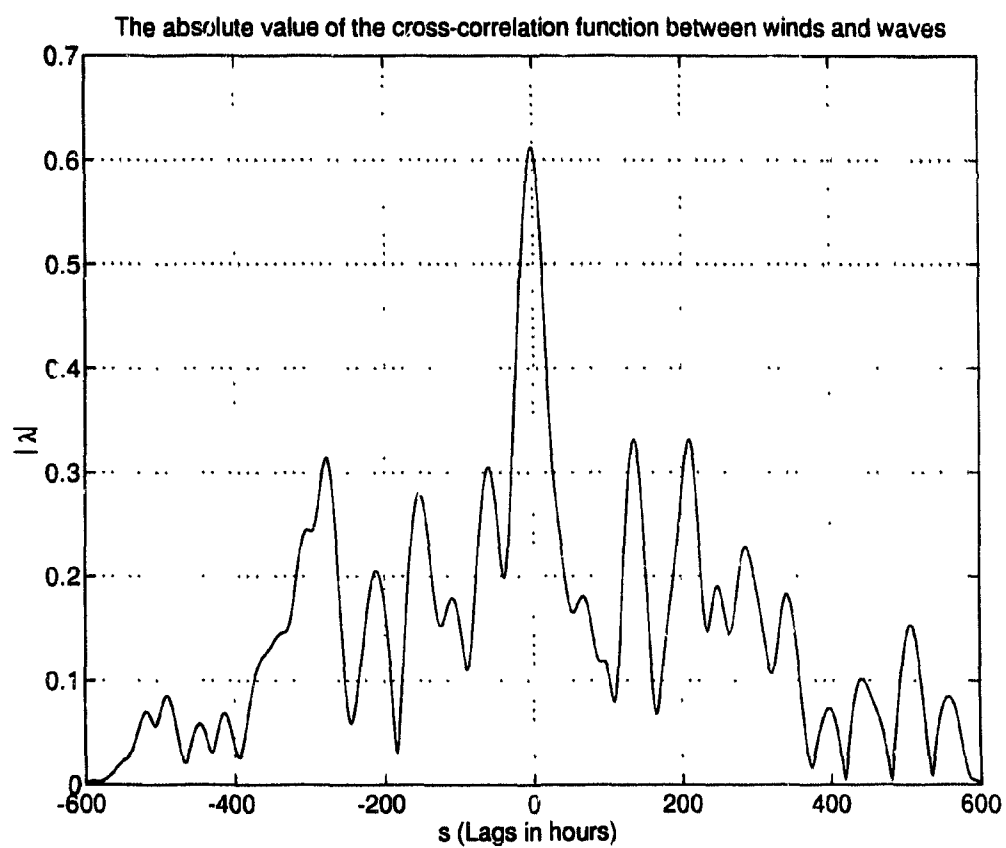
Figure 5.13: The absolute value of the cross-correlation function $|\lambda|$ between waves and winds.
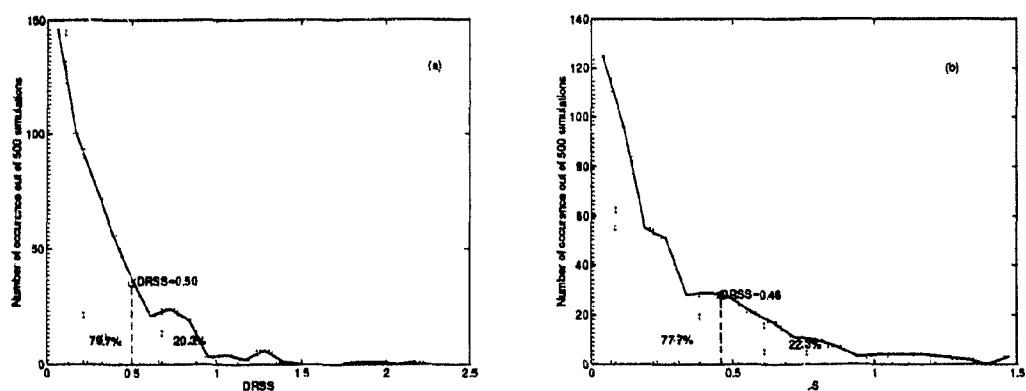
Figure 5.14. Clone technique is used to check the significance of adding wave alone on the top of the pressure gradient (Panel a) and the significance of adding the wave alone on the top of the pressure gradient (Panel b). Note, for this figure the normal matrix $\mathcal{H}$ is a two column matrix (containing two predictors) while for Figure 5.13, $\mathcal{H}$ is three column matrix (containing three predictors).

small. Figures (5.15), (5.16), (5.17) and (5.18) show the effects of the second terms. The dotted lines are the total response, the dashed lines are the steady response. The solid lines represent the low-pass filtered version of the total response. The difference between the dotted lines and the dashed lines consists mainly of damped inertial oscillations, as can be seen from the figures. The good agreement of the solid and the dashed lines suggests that it is appropriate to use a steady regression model (as far as the low-pass filtered motion is concerned, cf. page 69.).

It can be seen from Fig. (5.17) that the alongshore flow is mainly a geostrophic flow. In contrast, the cross-shore flow is induced mainly by local forces. Figures (5.15) and (5.16) show that both wind-induced and wave-induced model responses give a fairly good simulation of observed flows in terms of their fluctuation with time. However, in terms of flow magnitude, the wind-induced flow alone already exceeds the observed flow. The wave-induced flow seems to give a right size of the amplitudes. (But the magnitudes can be adjusted by choosing a different value for the wind drag coefficient and a different representative wave height.)

As mentioned in Section 5.3, the regression coefficients $\hat{C}_1$, $\hat{C}_2$, $\hat{C}_3$ correspond to $SE/f\delta_e$, WA and $igBE/f$ respectively. Listed in Table (5.2) are the moduli and angles of $SE/f\delta_e$, WA and $igBE/f$. Comparison of this table with Table (5.1) shows that the moduli of WA and $igBE/f$ are on the same order with $\hat{C}_2$ and $\hat{C}_3$, but the modulus of $SE/f\delta_e$ is about four times as large as that of $\hat{C}_1$. The agreement in the angles, however, is fairly good. This good agreement between $\tan^{-1}\left(\frac{SE}{f\delta_e}\right)$ and $\tan^{-1}\hat{C}_1$ is not surprising because the former is merely an echo of the input $\delta_e/h = 7m$. The good agreement between $\tan^{-1}\left(\frac{igBE}{f}\right)$ and $\tan^{-1}\hat{C}_3$ is not surprising either because $igBE/f$ is not sensitive to the value of δ_e/h away from the sea bottom. The fairly good agreement between $\tan^{-1}$ WA and $\tan^{-1}\hat{C}_2$, however, is somewhat encouraging. The angle of WA is a complicated function of δ_e/h (cf. Eqs. 4.17 and 4.18), and this information is not contained in the regression model.

u-components

v-components
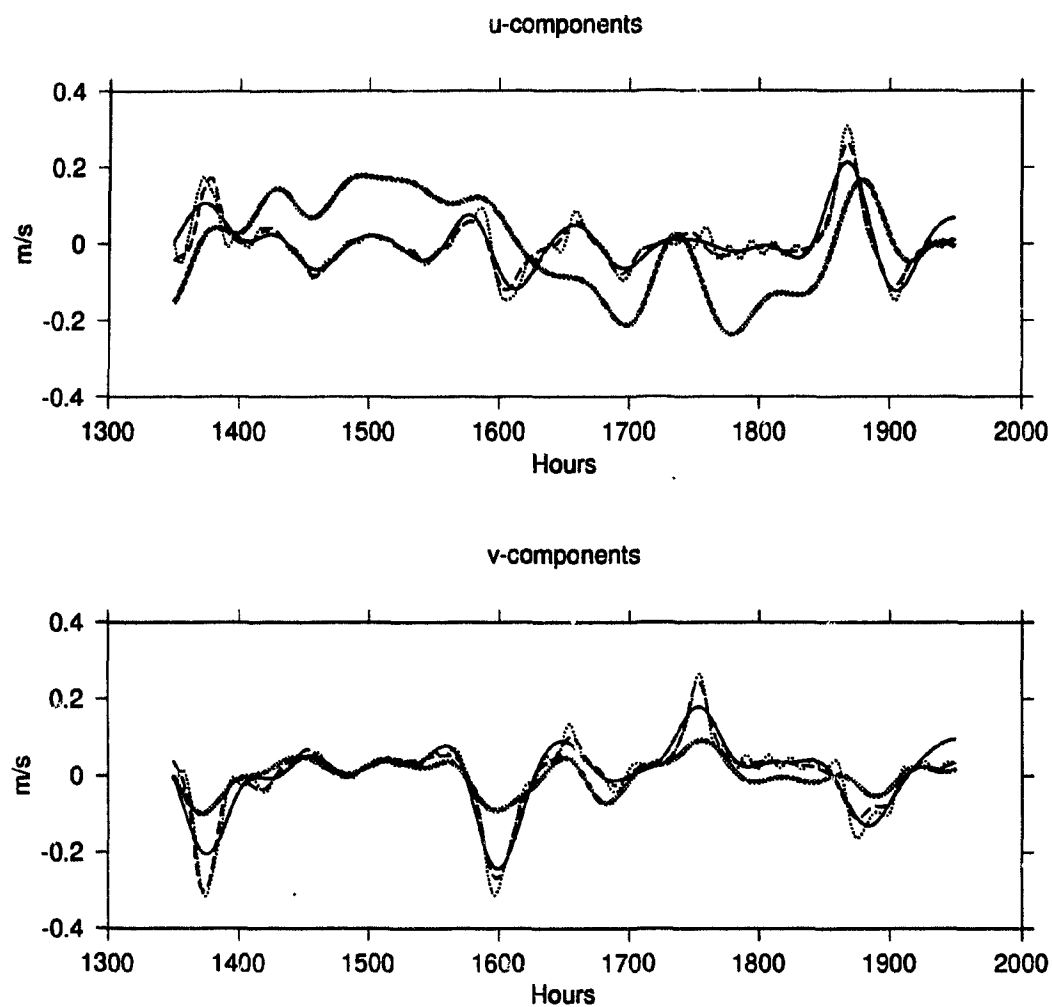
Figure 5.15: The modeled wind induced velocity and the observed velocity (shaded line). The dotted line is the model output which includes the response to the present time force and the past time force. The solid line is the low pass filtered version of dotted line. The dashed line is the model response to the present force.

u-components

v-components
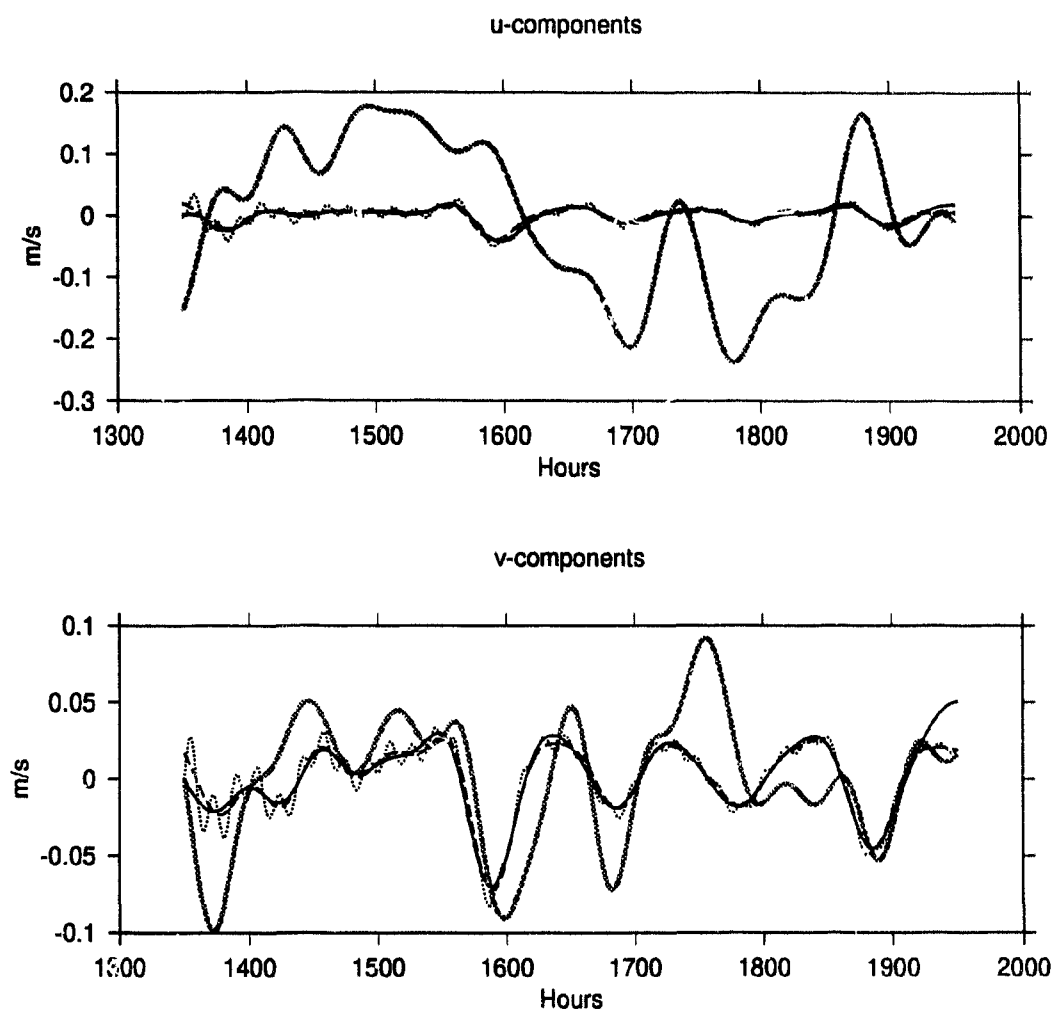
Figure 5.16: The modeled Stokes drift induced velocity and the observed velocity (shaded line). The dotted line is the model output which includes the response to the present time force and the past time force. The solid line is the low pass filtered version of dotted line. The dashed line is the model response to the present force.

u-components

v-components
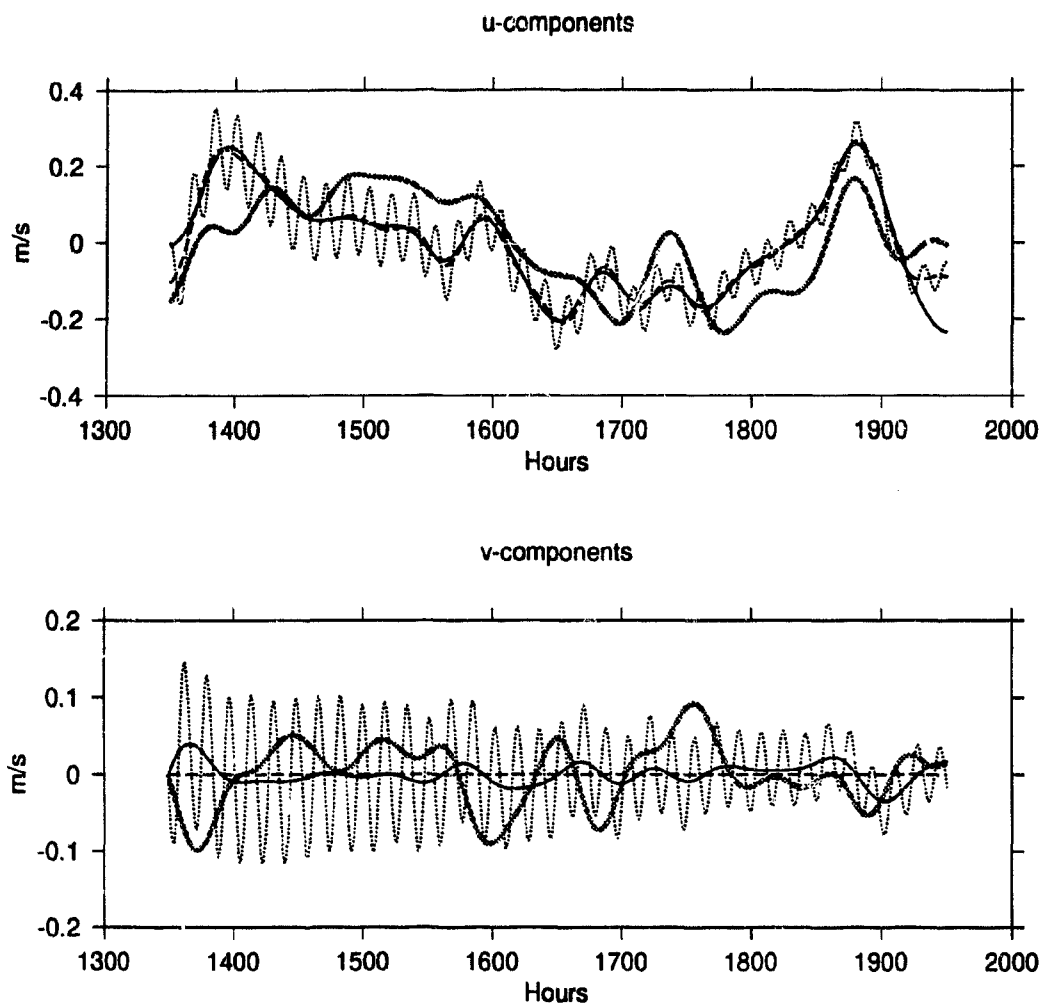
Figure 5.17: The modeled cross-shore pressure gradient induced velocity and the observed velocity (shaded line). The dotted line is the model output which includes the response to the present time force and the past time force. The solid line is the low pass filtered version of dotted line. The dashed line is the model response to the present force.
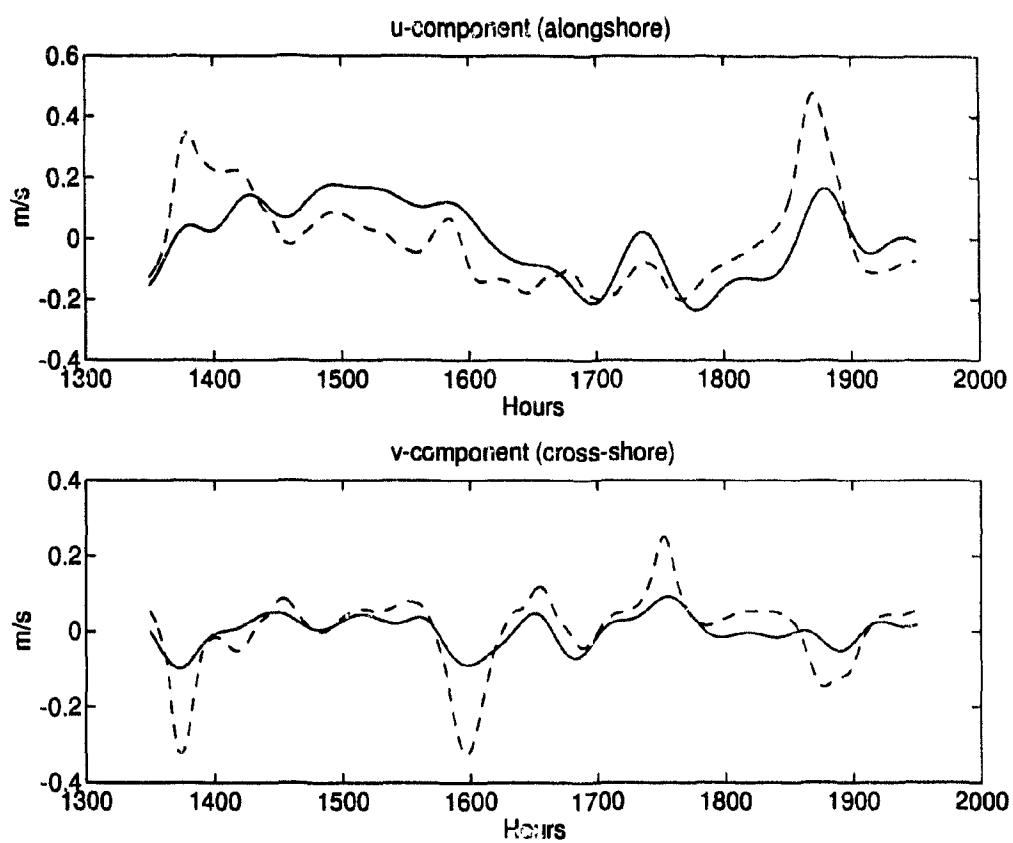
Figure 5.18: The modeled velocity driven by the three forces and the observed velocity. The solid line is the observed data and the dashed line is the model response to the present time force.

Table 5.2: The gain and the phase yielded by the numerical model

	τ	$\mathfrak{S}$	$\nabla\eta$
q_{04}	$\left\|\frac{SE}{f\delta_e}\right\| = 1119$ $\tan^{-1}\frac{SE}{f\delta_e} = -77.72°$	$\|WA\| = 0.36$ $\tan^{-1}\|WA\| = -152.96°$	$\left\|\frac{igBE}{f}\right\| = 9.62 \times 10^4$ $\tan^{-1}\frac{igBE}{f} = 90.00°$

5.7 Summary and discussion

Data of currents, wave parameters, wind velocity and bottom pressure have been gathered and pre-processed from the CASP data set. The wave parameters are combined as a single representative force time series, i.e., the surface Stokes drift $\mathfrak{S}$. The wind velocity is converted to a wind stress, $\tau(t)$, according to the standard conversion formula. The cross-shore pressure gradient data are calculated from four bottom pressure gauges. In the pre-processing of the current data, it is noticed that the Mf (Lunar fortnightly) tidal current is strong. Therefore a detiding procedure is introduced to the data before applying a low pass filter.

The time series of wind stress, surface Stokes drift, and cross-shore pressure gradient are used as inputs to the linear regression model, while the observed currents constitute the output. Since the mean effects of the surface waves decay exponentially with the depth, data from a shallow current meter (the mooring at $z = -4m$ of Station 8) was chosen as the time series for the regression analysis. The regression coefficients represent the gains and angles of the flow driven by the three forces. Further discussion focused on the angles of the flows with respect to their driving forces. The angle of wind-induced flow yields an estimate of $7m$ for the Ekman depth. The angle of wave-induced flow is near the theoretical value.

For testing the significance of the chosen predictors, two approaches are taken: usual regression analysis and "clone" random simulations. The former approach shows confidence levels of ≥ 0.90 for the three predictors. The latter approach gives, however, much lower levels. The confidence level for the predictor of the pressure

gradient drops down to 81%, and those for winds and waves drop down to 52% and 57% respectively. The disagreement between the two approaches may indicate that the degrees of freedom are overestimated in the regression analysis. The low confidence levels for the wind and wave predictors may be explained by the fairly high correlation ($|\lambda| = 0.61$) between them.

Based on the Ekman depth information obtained through the regression analysis, a numerical model is used to calculate the response of a local water column to the same three forces used in the regression model. The numerical model results show that the steady response accounts for most of the total response, which lends support to the use of a steady linear regression model. The numerical model also shows that while the alongshore flow is mainly a geostrophic flow, the cross-shore flow is mainly driven by local forces. Both the wind and the wave driven simulations give fairly good agreement with the observed cross-shore flow in terms time fluctuation. However, whether the waves really played a role in driving the flow is uncertain due to the the fact that the waves and winds are highly correlated. In future experiments, carefully chosen conditions where waves are strong but winds are weak would be vital for investigating the wave-driven flow.

5.8 Appendix A: Responses of a local water column to the present time forces and to the past time forces

Using the relation provided by Eq. (3.45), Eq. (5.1) can be written as

$$q \;=\; \frac{\partial[\tau(t)H(t)]}{\partial t} * q_d + \frac{\partial[\mathfrak{R}(t)H(t)]}{\partial t} * q_w + \frac{\partial[\nabla\eta H(t)]}{\partial t} * q_s. \tag{5.25}$$

Take the first time convolution as an example.

$$\frac{\partial \tau(t)}{\partial t} * q_d \;=\; \left[\tau(t)\delta(t) + \frac{\partial\tau(t)}{\partial t}\right] * \left[\mathrm{SE}(z) - \sum_n a_n \cos(\omega_n z) e^{-b_n t}\right],$$

$$\begin{aligned}
= \quad & \tau(0)\left[\mathrm{SE}(z) - \sum_n a_n \cos(\omega_n z)e^{-b_n t}\right] + [\tau(t) - \tau(0)]\,\mathrm{SE}(z) \\
& -\frac{\partial \tau(t)}{\partial t} * \sum_n a_n \cos(\omega_n z)e^{-b_n t} \\
= \quad & \tau(t)\mathrm{SE}(z) - \tau(0)\sum_n a_n \cos(\omega_n z)e^{-b_n t} \\
& -\frac{\partial \tau(t)}{\partial t} * \sum_n a_n \cos(\omega_n z)e^{-b_n t}.
\end{aligned} \tag{5.26}$$

The second and the third convolutions can be derived similarly, and Eq. (5.3) then follows.

Chapter 6

A New Method for Numerical Modelling of the 3-D Circulation in Shallow Seas

6.1 Introduction

Thus far this thesis has been essentially concerned with motions in a single water column. Of course, water columns are connected to each other through the continuity of the water mass (for linearized motion). A means to combine the 1-D motion of separate columns is needed to obtain a solution for full 3-D motions. A common method is the Jelesnianski bottom stress approach where the 1-D analytical solution is used to supply a bottom stress to a set of depth averaged equations to provide closure for the numerical solution. Jelesnianski's (1970) method originated from one of Welander's (1957) ideas, which was reviewed in Chapter 1 (cf. Table 1.1). Welander's other idea for the "assembling" of the motion of separate fluid columns, i.e, the transport approach, has not yet been implemented (cf. page 7 and Table 1.1).

This chapter implements Welander's second suggestion. First the details of the implementation are described. Then the new method is tested in Heaps' (1971) basin

in order to make a comparison with some standard results. The advantage of the new method over other existing methods will be illustrated with examples and analyzed theoretically. Appendix B to this chapter extends the method to the case where the eddy viscosity profile becomes arbitrary so that the analytical solution in the vertical is no longer possible. The extension of the method to the diagnostic case is also presented in the appendix.

In developing and testing the method, the response to wave forcing is not included. This is both for simplicity and for comparison with previous model results in which the wave forcing was not present. The method itself does allow for the addition of wave forcing.

6.2 The transport approach

6.2.1 Step force response in velocity and transport under slip bottom conditions

The step force responses in velocity to wind and to sea surface slope under the non-slip bottom condition have been presented in Chapter 4 (cf., Eqs. 4.53, 4.54). The slip bottom condition is perhaps a more appropriate form if the "sea bottom" is actually placed on top of the bottom logarithmic layer. It is also more general since the non-slip condition is a limit case of the slip condition. For this reason, and for a comparison with Heaps' results later on, the step force response under the slip bottom condition is considered here.

The step force responses are governed by

$$\left.\begin{array}{l} \frac{\partial q_d}{\partial t} + if q_d - \nu \frac{\partial^2 q_d}{\partial z^2} = 0 \\ \nu \frac{\partial q_d}{\partial z}\Big|_{z=0} = I_\tau, \qquad \left(\nu \frac{\partial q_d}{\partial z} - \kappa q_d\right)_{z=-h} = 0 \\ q_d|_{t=0} = 0 \end{array}\right\} \tag{6.1}$$

and

$$\left.\begin{array}{l} \frac{\partial q_s}{\partial t} + i f q_s - \nu \frac{\partial^2 q_s}{\partial z^2} = -g I_{\nabla \eta} \\ \nu \frac{\partial q_s}{\partial z}\Big|_{z=0} = 0, \qquad \left(\nu \frac{\partial q_s}{\partial z} - \kappa q_s\right)_{z=-h} = 0 \\ q_s|_{t=0} = 0. \end{array}\right\} \qquad (6.2)$$

The parameter κ in the bottom condition may be called the slip parameter.[1] The non-slip condition is recovered under the limit of $\kappa \longrightarrow \infty$. Their solutions are found to be as

$$q_d(t, z; I_\tau) = \frac{I_\tau}{f \delta_e}\left[\text{SE}(z) - \sum_{n=0}^{\infty} a_n e^{-b_n t} \cos(\omega_n z)\right] \qquad (6.4)$$

$$q_s(t, z; I_{\nabla \eta}) = i \frac{g I_{\nabla \eta}}{f}\left[\text{BE}(z) - \sum_{n=0}^{\infty} c_n e^{-b_n t} \cos(\omega_n z)\right], \qquad (6.5)$$

where

$$\text{SE}(z) = \sqrt{2} e^{-i\pi/4} \frac{\sinh \alpha(h+z) + \frac{\alpha\nu}{\kappa}\cosh \alpha(h+z)}{\cosh \alpha h + \frac{\alpha\nu}{\kappa}\sinh \alpha h} \qquad (6.6)$$

$$\text{BE}(z) = 1 - \frac{\cosh \alpha z}{\cosh \alpha h + \frac{\alpha\nu}{\kappa}\sinh \alpha h} \qquad (6.7)$$

$$\delta_e = \sqrt{\frac{2\nu}{f}} \qquad (6.8)$$

$$\alpha = \sqrt{\frac{if}{\nu}} \stackrel{or}{=} \frac{1+i}{\delta_e} \qquad (6.9)$$

$$\gamma_n = \frac{\omega_n h}{\sqrt{2}}\left(\frac{\delta_e}{h}\right) \qquad (6.10)$$

$$a_n = \left(\frac{\delta_e}{h}\right)\frac{4}{\left[(\omega_n h)^2 \left(\frac{\delta_e}{h}\right)^2 + 2i\right](1 + \xi_n)} \qquad (6.11)$$

$$b_n = \left[\frac{(\omega_n h)^2}{2}\left(\frac{\delta_e}{h}\right)^2 + i\right] f \qquad (6.12)$$

---

[1]When the wave force needs to be considered, the following modification for the slip bottom condition may be suitable,

$$\nu \frac{\partial q}{\partial z} = \kappa\left[q - \frac{3}{2}q_{st}(-h)\right], \qquad (6.3)$$

and $\psi(z)$ in the expression for wave body force (cf. Eq. 2.70) should set to be zero accordingly.

$$c_n = i \frac{4 \sin \omega_n h}{\omega_n h \left[(\omega_n h)^2 \left(\frac{\delta_e}{h} \right)^2 + 2i \right] (1 + \xi_n)}. \tag{6.13}$$

The ω_n are the roots of

$$\omega_n \tan \omega_n h = \frac{\kappa}{\nu}, \tag{6.14}$$

which must fall in the range

$$n\pi \leq \omega_n h \leq (n + 1/2)\pi. \tag{6.15}$$

In addition, a parameter

$$\xi_n = \frac{\sin 2\omega_n h}{2\omega_n h} \qquad \text{when } \kappa \to \infty, \, \xi_n \to 0, \tag{6.16}$$

has been introduced to reflect the slipping of each modal motion at the bottom.

The response to the arbitrary forces is obtained by use of Eqs. (3.35) and (3.41) as

$$q(t, z) = \nabla \eta(t) * \dot{q}_s(t, z; I_{\nabla \eta}) + \tau(t) * \dot{q}_d(t, z; I_\tau). \tag{6.17}$$

All the features of the Ekman dynamics, such as top and bottom Ekman layers, damped inertial oscillations with higher modes dying away faster, and the momentum diffusion e-folding time scale $(\delta_e^2/h^2 f)^{-1}$ (cf. Eq. 6.12), have been preserved analytically. The unknown $\nabla \eta(t)$ only affects the amplitude of the velocity profile (in a time convolution fashion).

From the initial conditions in Eqs. (6.1) and (6.2), we have

$$\sum_{n=0}^{\infty} a_n \cos(\omega_n z) = \text{SE}(z) \tag{6.18}$$

$$\sum_{n=0}^{\infty} c_n \cos(\omega_n z) = \text{BE}(z) \tag{6.19}$$

which is obtained by setting $t = 0$ in Eqs. (6.4) and (6.5). In fact, a_n and c_n given by Eqs. (6.11) and (6.13) were calculated from these two relations. Appendix A will use these two relations to accelerate the convergence of the velocity series.

Defining

$$[Q_d(t;\ I_\tau),\ Q_s(t;\ I_{\nabla\eta})] \;=\; \int_{-h}^{0} [q_d(t,z;I_\tau),\ q_s(t,z;\ I_{\nabla\eta})]\,dz \qquad (6.20)$$

as the two step force transport responses induced by wind and sea surface slope, respectively. Substitution of Eqs. (6.4) and (6.5) into the above yields,

$$Q_d(t;\ I_\tau) \;=\; -i\frac{I_\tau}{f}\left(D_d - \sum_{n=0}^{\infty} E_n e^{-b_n t}\right) \qquad (6.21)$$

$$Q_s(t;\ I_{\nabla\eta}) \;=\; i\frac{ghI_{\nabla\eta}}{f}\left(D_s - \sum_{n=0}^{\infty} G_n e^{-b_n t}\right) \qquad (6.22)$$

where

$$D_d \;=\; 1 - \frac{1}{\cosh\alpha h + \frac{\alpha\nu}{\kappa}\sinh\alpha h} \qquad (6.23)$$

$$D_s \;=\; 1 - \frac{1}{\alpha h}\frac{\tanh\alpha h}{1 + \frac{\alpha\nu}{\kappa}\tanh\alpha h} \qquad (6.24)$$

$$E_n \;=\; \frac{4i\sin\omega_n h}{\omega_n h\left[(\omega_n h)^2\left(\frac{\delta_e}{h}\right)^2 + 2i\right](1 + \xi_n)} \qquad (6.25)$$

$$G_n \;=\; \frac{4i\sin^2\omega_n h}{(\omega_n h)^2\left[(\omega_n h)^2\left(\frac{\delta_e}{h}\right)^2 + 2i\right](1 + \xi_n)}. \qquad (6.26)$$

The coefficients, $-iI_\tau/f$ and $ighI_{\nabla\eta}/f$, on the RHS of Eqs. (6.21) and (6.22) are the transport amplitudes, whose physical interpretations are the familiar steady Ekman transport and geostrophic transport in deep water, respectively. The quantities in parentheses are the corrections for the effects of bottom friction and inertial accelerations.

Again, as a result of the initial conditions of Eqs. (6.1) and (6.2), there are two relations:

$$\sum_{n=0}^{\infty} E_n \;=\; D_d \qquad (6.27)$$

$$\sum_{n=0}^{\infty} G_n \;=\; D_s. \qquad (6.28)$$

These two relations will be used later to determine a proper mode number when a tolerance for truncation errors is given.

When the step force responses are known, the responses to arbitrary forcing can be calculated by

$$Q = \nabla\eta(t) * \dot{Q}_s(t;\ I_{\nabla\eta}) + \tau(t) * \dot{Q}_d(t;\ I_\tau). \tag{6.29}$$

6.2.2 The difference form of the continuity equation and an η—Q lattice

The continuity equation can be written in the form

$$\frac{\partial\eta}{\partial t} + \Re\{\nabla^* Q\} = 0, \tag{6.30}$$

where

$$\nabla^* \equiv \frac{\partial}{\partial x} - i\frac{\partial}{\partial y} \tag{6.31}$$

and $\Re$ denotes the real part. Q and η are coupled through the sea surface slope. We need to integrate the continuity Eq. (6.30) and evaluate the transport of Eq. (6.29) numerically through time. Let us first discretize the continuity equation. The next section discusses how to evaluate the transport given the updated value of $\nabla\eta$.

In differencing the above form of the continuity equation, an $\eta - Q$ grid comes naturally (Fig. 6.1), which is the counterpart of the Arakawa E-grid in the complex plane. Adopting the $\eta - Q$ grid not only facilitates calculation of $\nabla\eta$ for each Q point, but also automatically eliminates the spurious residual flow that occurs when one uses the Arakawa C-grid (Jamart and Ozer, 1986) (cf. Figs. 6.6 and 6.7). This is because, in contrast with the Arakawa C-grid, with the $\eta - Q$ grid there is no need to average the Coriolis force over four neighboring grid points.

Using a FTCS (forward in time and centered in space) scheme to discretize Eq. (6.30) yields

$$\eta_{l,m}^{(j+1)} = \eta_{l,m}^{(j)} - \Re\left\{\left[Q_{l,m+1}^{(j)} - Q_{l,m-1}^{(j)}\right] s_x - i\left[Q_{l+1,m}^{(j)} - Q_{l-1,m}^{(j)}\right] s_y\right\} \tag{6.32}$$
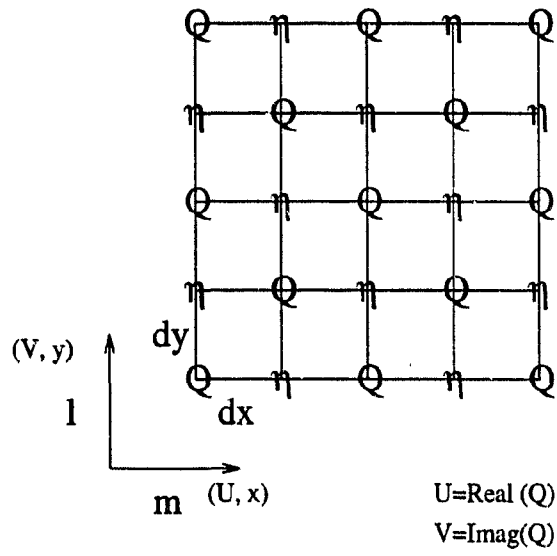
Figure 6.1: $\eta - Q$-grid, a counterpart of the Arakawa E-grid in the complex plane. Using such grid not only facilities calculation of $\nabla\eta$ for each Q point, but also automatically eliminates spurious residual flow problem inherent in the Arakawa C-grid when the Coriolis force is included.

where $s_x = \Delta t/(2\Delta x)$ and $s_y = \Delta t/(2\Delta y)$, and the subscripts l, m d\ notes the grid point indices and the superscript j denotes the jth time step.

6.2.3   A recursion scheme for the time convolution

For convenience, the following notation is introduced: $R(t; 1)$ represents the response of a linear system to a Heaviside unit step force, and $R(t; F)$ represents the response to an arbitrary time varying force F. Thus R can signify the velocity response, transport response, or bottom stress response, and F can represent the wind stress or sea surface slope. The recursion scheme derived below will be suitable for any of these cases. The relationship between $R(t; F)$ and $R(t; 1)$ is given by

$$R(t; F) = \int_0^t F(t') \frac{\partial R(t - t'; 1)}{\partial t} dt'. \tag{6.33}$$

Numerical evaluation of this integral is necessary since $F(t)$ is an arbitrary time function. Because t appears in both the integral limit and in the integrand, the usual discrete summation for the integral would require recalculation of the summation from $t = 0$ for each time step. An economic evaluation scheme is thus needed, and Jelesnianski (1970) has provided one. However, both his derivation and his recursion scheme are complicated. This section gives a derivation for a simpler and more physically appealing recursion scheme.

The structure of the solutions presented in Eqs. (6.4), (6.5), (6.21) and (6.22) suggests that it is proper to write $R(t; 1)$ in the following form

$$R(t; 1) = C(z) - \sum_{n=0}^{\infty} \phi_n(z) e^{-b_n t}, \tag{6.34}$$

(where $C(z)$ can be $\frac{I_r}{f\delta_e} \mathrm{SE}(z)$, $i\frac{gI_n}{f} \mathrm{BE}(z)$, $-i\frac{I_r}{f} D_d$ or $i\frac{ghI_m}{f} D_s$, and $\phi_n(z)$ can be $\frac{I_r}{f\delta_e} a_n \cos\omega_n z$, $i\frac{gI_m}{f} c_n \cos\omega_n z$, $-i\frac{I_r}{f} E_n$, or $i\frac{ghI_m}{f} G_n$). Since the initial response is set to be zero (cf. Eqs. 6.18, 6.19, 6.27 and 6.28), we have

$$\sum_{n=0}^{\infty} \phi_n(z) = C(z) \tag{6.35}$$

(except at $z = 0$ when $R(t; 1)$ represents the stress). Substitution of Eq. (6.34) into Eq. (6.33) gives

$$R(t; F) = \int_0^t F(t') \sum_{n=0}^{\infty} \phi_n(z) b_n e^{-b_n(t-t')} dt'$$

$$= \sum_{n=0}^{\infty} r_n(t; F) \tag{6.36}$$

where

$$r_n(t; F) = \int_0^t F(t') \phi_n(z) b_n e^{-b_n(t-t')} dt' \tag{6.37}$$

which denotes the response to an external force by the nth mode. For the next time step, $t + \Delta t$,

$$R(t + \Delta t; F) = \left\{ \int_0^t + \int_t^{t+\Delta t} \right\} F(t') \sum_{n=0}^{\infty} \phi_n(z) b_n e^{-b_n(t+\Delta t - t')} dt'$$

$$= \sum_{n=0}^{\infty} \left\{ r_n(t; F) e^{-b_n \Delta t} + F(t) \phi_n(z) \left[1 - e^{-b_n \Delta t} \right] \right\} \tag{6.38}$$

where in the first integral the result calculated at the previous time step has been used, and in the second integral $F(t')$ has been approximated by $F(t)$ for $t' \in [t, t + \Delta t]$. (It is allowed here to use a combination of $F(t)$ and $F(t + \Delta t)$ to approximate $F(t')$. However this will lead to an implicit scheme to solve the continuity equation, since $\nabla \eta$ is one of the forces that F signifies.) Let us denote

$$r_n(t + \Delta t; F) = r_n(t; F) e^{-b_n \Delta t} + F(t) r_n(\Delta t; 1) \tag{6.39}$$

where

$$r_n(\Delta t; 1) = \phi_n(z) \left[1 - e^{-b_n \Delta t} \right], \tag{6.40}$$

which gives the response by the nth mode to a unit force in one time step. Then Eq. 6.38 can be written as

$$R(t + \Delta t; F) = \sum_{n=0}^{\infty} r_n(t + \Delta t; F). \tag{6.41}$$

A recursion scheme for evaluating the response convolution is thus obtained. Starting from $r(0; F) = 0$ (by definition of Eq. 6.37), one can use Eq. (6.39) to evaluate the response to an external force by each mode for successive time steps, and then use Eq. (6.41) to obtain the total response. The scheme is summarized in the following box:

$$
\begin{aligned}
\lambda_n &= e^{-b_n \Delta t} \\
r_{nF}^{(0)} &= 0 \\
r_{n1}^{(1)} &= \phi_n(z)(1 - \lambda_n) \\
\\
r_{nF}^{(j+1)} &= r_{nF}^{(j)} \lambda_n + F^{(j)} r_{n1}^{(1)} \\
R_F^{(j+1)} &= \sum_{n=0}^{N} r_{nF}^{(j+1)} \\
&\quad (j = 0, 1, 2, \dots)
\end{aligned}
\tag{6.42}
$$

where the notation $r_{nF}^{(j)}$ is short for $r_n(j\Delta t; F)$, and $r_{n1}^{(1)}$ for $r_n(\Delta t; 1)$, etc., N is a positive integer whose proper value will be discussed later.

A physical interpretation of the recursion scheme is as follows: the first term on the RHS of Eq. (6.39) (or the fourth equation of Eqs. 6.42) is due to the "initial" condition at the previous time step and the second term is due to the latest "kick" by the external force. $r_{n1}^{(1)}$ acts as a weight to partition the external force F into the n modes. Since the frictional force has been taken care of in $r_{n1}^{(1)}$, one may read $F^{(j)} r_{n1}^{(1)}$ as a net force to drive the nth modal motion during the time interval $[j\Delta t, (j+1)\Delta t]$. The factor $e^{-b_n \Delta t}$ describes how each mode evolves once set into motion. Different modes evolve differently because of the different values of b_n ($n = 0, 1, 2, \dots$).

The above recursion scheme can be applied to the response in velocity, stress and transport when one substitutes the corresponding $C(z)$, $\phi_n(z)$ and b_n. In terms of velocity, the recursion scheme is expressed in Appendix A, where a discussion is also given on accelerating the velocity convergence using relations of Eqs. (6.18) and

(6.19). In terms of the transport, the recursion scheme is expressed as

$$
\begin{aligned}
\lambda_n &= e^{-b_n \Delta t} \\
r_{nF}^{(0)} &= 0 \\
r_{n1\tau}^{(1)} &= -i\frac{I_\tau}{f} E_n (1 - \lambda_n) \\
r_{n1\eta}^{(1)} &= i\frac{ghI_{\nabla\eta}}{f} G_n (1 - \lambda_n) \\
\\
r_{nF}^{(j+1)} &= r_{nF}^{(j)} \lambda_n + \tau^{(j)} r_{n1\tau}^{(1)} + \nabla\eta^{(j)} r_{n1\eta}^{(1)} \\
Q^{(j+1)} &= \sum_{n=0}^{N} r_{nF}^{(j+1)} \\
&\quad (j = 0, 1, 2, ...)
\end{aligned}
\tag{6.43}
$$

where Q takes the place of R_F, and E_n and G_n are given by Eqs. (6.25) and (6.26). In programming Eqs. (6.43), one should evaluate those $j-$ independent quantities once before the updating "do-loop". Also, one can replace the symbols of unit wind stress I_τ and unit slope $I_{\nabla\eta}$ in the program by the number 1 so that the inputs τ and $\nabla\eta$ can automatically take care of the units and directions.

The formula for updating Q has now been obtained. Equations (6.32) and (6.43) form an explicit scheme for updating Q and η alternately. In various cases (different values of δ_e/h, flat or varying bottom topography, steady or unsteady wind, etc.) the numerical experimentation shows that the scheme is stable under the CFL condition $\Delta t \leq \Delta x \Delta y / \sqrt{gh(\Delta x^2 + \Delta y^2)}$ (the scheme is still stable even when the equal sign in the condition is taken). However, a theoretical stability analysis for the scheme is not available yet.

6.2.4 Transfer of the zero flux boundary condition to that for the surface elevation

For an open lateral boundary condition, one may use the Sommerfeld radiation condition to update η and Q based on information at neighboring interior points at the previous time step (e.g., Chapman, 1985). For a solid lateral boundary, the $Q - \eta$ lattice introduced above requires that one calculates the surface gradient for Q boundary

points based on the fact that the flux normal to the wall is zero. Here let us focus on the transfer of the zero flux condition to that for the surface gradient.

According to Eq. (6.43), $Q^{(j+1)}$ also can be written as

$$Q^{(j+1)} = \sum_{n=0}^{N} r_{nF}^{(j)} e^{-b_n \Delta t} + \tau^{(j)} R_{1\tau}^{(1)} + \nabla \eta^{(j)} R_{1\eta}^{(1)} \tag{6.44}$$

where

$$R_{1\tau}^{(1)} = \sum_{n=0}^{N} r_{n1\tau}^{(1)} \tag{6.45}$$

$$R_{1\eta}^{(1)} = \sum_{n=0}^{N} r_{n1\eta}^{(1)}. \tag{6.46}$$

Let

$$R_{1\eta}^{(1)} = \mathcal{A} + i\mathcal{B} \tag{6.47}$$

where $\mathcal{A}$ and $\mathcal{B}$ are real, then

$$\nabla \eta^{(j)} R_{1\eta}^{(1)} = \left(\mathcal{A} \frac{\partial \eta}{\partial x} - \mathcal{B} \frac{\partial \eta}{\partial y} \right)^{(j)} + i \left(\mathcal{A} \frac{\partial \eta}{\partial y} + \mathcal{B} \frac{\partial \eta}{\partial x} \right)^{(j)}. \tag{6.48}$$

Thus, from Eq. (6.44), on a lateral boundary where $U = \Re\{Q\}$ should be zero,

$$\frac{\partial \eta^{(j)}}{\partial x} = \frac{\mathcal{B}}{\mathcal{A}} \frac{\partial \eta^{(j)}}{\partial y} - \frac{1}{\mathcal{A}} \Re \left\{ \sum_{n=0}^{N} r_{nF}^{(j)} e^{-b_n \Delta t} + \tau^{(j)} R_{1\tau} \right\}, \tag{6.49}$$

and on a lateral boundary where $V = \Im\{Q\}$ should vanish,

$$\frac{\partial \eta^{(j)}}{\partial y} = -\frac{\mathcal{B}}{\mathcal{A}} \frac{\partial \eta^{(j)}}{\partial x} - \frac{1}{\mathcal{A}} \Im \left\{ \sum_{n=0}^{N} r_{nF}^{(j)} e^{-b_n \Delta t} + \tau^{(j)} R_{1\tau} \right\} \tag{6.50}$$

where $\Im$ denotes the imaginary part of a complex quantity. In a corner where both U and V vanish,

$$\begin{bmatrix} \frac{\partial \eta}{\partial x} \\ \frac{\partial \eta}{\partial y} \end{bmatrix}^{(j)} = - \begin{bmatrix} \mathcal{A} & -\mathcal{B} \\ \mathcal{B} & \mathcal{A} \end{bmatrix}^{-1} \begin{bmatrix} \Re\{...\} \\ \Im\{...\} \end{bmatrix}^{(j)} \tag{6.51}$$

where $\{...\}$ is the same as those of Eqs. (6.49) and (6.50).

6.2.5 How large must N be?

In the transport method, the solution for the sea surface elevation is a major calculation. Once this is known, velocities can be evaluated with the analytical formula of Eq. (6.17), which converges exponentially since both SE(z) and BE(z) have been extracted from the series (cf. Eq. 6.82). In numerically solving for the elevation, the transport method only involves the transport series, as the name of the method suggests. Thus, given a truncation error tolerance, the number of modes necessary to specify the transport series must be addressed.

Returning to the expressions for the transports given in Eqs. (6.21) and (6.22) allows the determination for a value of N given a truncated error tolerance. Rewrite Eqs. (6.21) and (6.22), with a reference to Eqs. (6.27) and (6.28), in the form

$$\frac{Q_d(t; I_\tau)}{I_{Q_d}} = \left(\sum_{n=0}^{N} + \sum_{n=N+1}^{\infty}\right)(1 - e^{-b_n t})E_n \tag{6.52}$$

$$\frac{Q_d(t; I_\tau)}{I_{Q_s}} = \left(\sum_{n=0}^{N} + \sum_{n=N+1}^{\infty}\right)(1 - e^{-b_n t})G_n \tag{6.53}$$

where, for brevity, the notation I_{Q_d} and I_{Q_s} has been introduced to represent the transport amplitudes $-i\frac{I_\tau}{f}$ and $i\frac{ghI_{\nabla\eta}}{f}$, respectively. Truncation errors per I_{Q_d} and per I_{Q_s} may then be defined as

$$er_1 = \sum_{n=N+1}^{\infty}(1 - e^{-b_n t})E_n \approx \sum_{n=N+1}^{\infty}E_n \tag{6.54}$$

$$er_2 = \sum_{n=N+1}^{\infty}(1 - e^{-b_n t})G_n \approx \sum_{n=N+1}^{\infty}G_n. \tag{6.55}$$

In the above definition, the terms $e^{-b_n t}E_n$ and $e^{-b_n t}G_n$ have been dropped, because $\sum_{n=N+1}^{\infty} e^{-b_n t}E_n$ and $\sum_{n=N+1}^{\infty} e^{-b_n t}G_n$ approach zero much faster than $\sum_{n=N+1}^{\infty} E_n$ and $\sum_{n=N+1}^{\infty} G_n$ respectively, so we need only consider the slowly convergent component to evaluate the truncation errors. Substitution of Eqs. (6.25) and (6.26) into Eqs. (6.54) and (6.55) yields

$$er_1 = \sum_{N+1}^{\infty}\frac{4i\sin\omega_n h}{(\omega_n h)\left[(\omega_n h)^2\left(\frac{\delta_e}{h}\right)^2 + 2i\right](1 + \xi_n)} \tag{6.56}$$

$$er_2 = \sum_{N+1}^{\infty} \frac{4i\sin^2\omega_n h}{(\omega_n h)^2 \left[(\omega_n h)^2 \left(\frac{\delta_e}{h}\right)^2 + 2i\right](1+\xi_n)}, \tag{6.57}$$

where $n\pi \le \omega_n h \le (n + 1/2)\pi$ (from Eq. 6.15). The first error corresponds to the wind induced flow and the second to the sea surface slope induced flow.

From the above Eqs. (6.56) and (6.57), we see that the coefficients of the two error series decrease towards zero as $1/n^3$ and $1/n^4$ $(n \ge N + 1)$ respectively. For problems concerning purely slope-induced flow (like tidal currents), N will be smaller for a given truncation error than for problems which include wind forcing. We also see that both truncation errors are inversely proportional to $(\delta_e/h)^2$. Thus we expect that N will be smaller in relatively shallow water (larger δ_e/h) than in deep water (smaller δ_e/h). This is because in shallower water, the momentum *versus* depth distribution is more uniform due to the stronger frictional effects, so fewer modes are needed to specify the distribution.

The absolute values of the errors can also be calculated. Using Eqs. (6.27) and (6.28), we have from Eqs. (6.54) and (6.55)

$$|er_1| = \left| D_d - \sum_{n=0}^{N} E_n \right| \tag{6.58}$$

$$|er_2| = \left| D_s - \sum_{n=0}^{N} G_n \right|, \tag{6.59}$$

with which one can quickly decide on a proper value of N for a given truncation error tolerance. For the case of non-slip bottom condition ($\kappa = \infty$), the absolute errors are tabulated in Tables (6.1) and (6.2) as a function of N, for different values of δ_e/h. These tables help to determine a proper mode number for a given error tolerance.

A complete description of the transport method for the case of constant eddy viscosity and constant density has been given. Table (6.3) concludes this section. The table shows that the main task in the transport method is calculation of the sea surface elevation, which requires fewer number of modes than calculation of the velocity and the bottom stress. After the main do-loop, the velocity profile at locations of interest can be recovered. A discussion on extension of the method to the case of arbitrary

Table 6.1: Truncation error per I_{Qd} $(=I_\tau/f$ where I_τ is one unit kinematic wind stress) when $t = 0$ for different values of δ_e/h and N. The truncated error is defined to be $er_1 = \sum_{N+1}^{\infty}$

	$\delta_e/h = 1$	$\delta_e/h = 1/2$	$\delta_e/h = 1/10$
N	$|er_1| \leq$	$|er_1| \leq$	$|er_1| \leq$
0	0.0319	0.1200	0.2734
1	0.0062	0.0245	0.1495
2	0.0021	0.0083	0.0955
3	0.0009	0.0037	0.0614
4	0.0005	0.0020	0.0392
5	0.0003	0.0011	0.0254
6	0.0002	0.0007	0.0170
7	0.0001	0.0005	0.0118
8	0.0001	0.0003	0.0084
9	0.0001	0.0003	0.0062
10	0.0000	0.0002	0.0047
11	0.0000	0.0001	0.0037
12	0.0000	0.0001	0.0029
13	0.0000	0.0001	0.0023
14	0.0000	0.0001	0.0019
15	0.0000	0.0001	0.0016

depth-dependent eddy viscosity, $\nu = \nu(z)$, and arbitrary density profile $\rho = \rho(x, y, z)$, is presented in Appendix B to this chapter.

6.3 Test of the transport method in Heaps' basin

6.3.1 Heaps' basin and Heaps' problem

In this section, the method described in the last section is tested against some standard results. Heaps' (1971) problem and Heaps' (1971) spectral method are chosen for comparison. The Heaps' problem is to numerically model the linear response of water in a rectangular basin to a constant wind. It is due to Heaps' (1971) pioneering work that the spectral method was introduced into oceanography for simulating 3-D

Table 6.2: Truncation error per I_{Q_s} ($=ighI_{\nabla\eta}/f$ where $I_{\nabla\eta}$ is one unit sea surface slope) when $t = 0$ for different values of δ_e/h and N. The truncated error is defined to be $er_2 = \sum_{N+1}^{\infty}$.

	$\delta_e/h = 1$	$\delta_e/h = 1/2$	$\delta_e/h = 1/10$
N	$|er_2| \leq$	$|er_2| \leq$	$|er_2| \leq$
0	0.0096	0.0365	0.1452
1	0.0015	0.0061	0.0589
2	0.0005	0.0019	0.0297
3	0.0002	0.0008	0.0163
4	0.0001	0.0004	0.0095
5	0.0001	0.0003	0.0058
6	0.0000	0.0002	0.0038
7	0.0000	0.0001	0.0026
8	0.0000	0.0001	0.0018
9	0.0000	0.0001	0.0013
10	0.0000	0.0000	0.0010
11	0.0000	0.0000	0.0008
12	0.0000	0.0000	0.0006
13	0.0000	0.0000	0.0005
14	0.0000	0.0000	0.0004
15	0.0000	0.0000	0.0003

Table 6.3: A summary of the transport approach.

Input

τ and lateral B.C.

Main do-loop

Numerical part

$$\frac{\partial \eta}{\partial t} + \Re\{\nabla^* Q\} = 0$$

Use (6.32)

$\nabla \eta$

Q

Analytical part

$$Q = \nabla \eta * \dot{Q}_s + \tau * \dot{Q}_d$$

Use (6.43)

Output

$\eta, \nabla \eta, Q$

$\nabla \eta$

$$q = \nabla \eta * \dot{q}_s + \tau * \dot{q}_d$$

Velocity profile recovery
at locations of interest

Use (6.82)
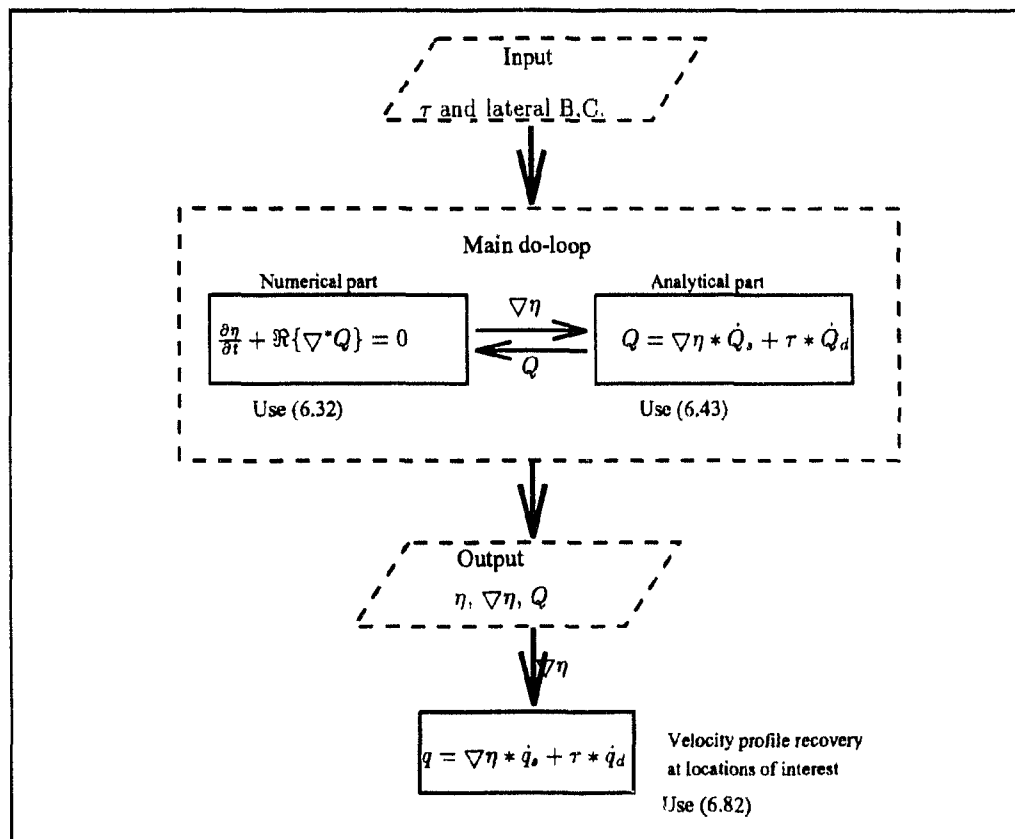
flows. The results from Heaps' work have been taken as a standard for comparison by most of the later spectral models (e.g, Davies, 1979; Davies, 1983; Davies, 1988; Lardner and Cekirge, 1988; Lardner, 1990; Sheng and Thompson, 1993).

Heaps' rectangular basin is 800 km long (North-South) and 400 km wide (East-West). This basin has been called Heaps' basin, whose geometry mimics the North Sea. Heaps used the C-grid scheme to locate η, u and v points in a horizontal plane grid of 35 × 19 lines (Fig. 6.2.b, solid line), using

$$\Delta x = 400/9 km, \quad \Delta y = 800/17 km. \tag{6.60}$$

Four η points (A, B, C, and D) were marked. At these points time series of the surface elevation, velocities (averaged over the four neighboring points) were recorded. Since the $\eta - Q$ grid scheme is used in the transport method, in order to locate the points A, B, C and D four η points in the grid plane with the same geometry as those of Heaps, a grid of 69 × 19 lines (Fig. 6.2.b) is placed on the horizontal plane for the transport method.

6.3.2 Comparison with Heaps' numerical solutions for the transient state

Shown in Fig. (6.3) are the three surface elevation time series at point B generated by the transport method, using 2 modes. They are compared with those generated by Heaps' spectral method with 10 modes. (For Heaps' spectral model, the "wet point only" technique, proposed by Jamart and Ozer, 1986, has been used to avoid a spurious residual flow). The difference between the two methods is represented by $\delta\eta_i$ ($i = 1, 2, 3$ for three values of ν, $\delta\eta_i = |\eta_T - \eta_H|_i$, where η_T represents η generated by the transport method and η_H generated by Heaps' spectral method). The figure demonstrates that the transport method works well and gives results that are very close to Heaps' results.

When the surface elevation field is obtained, a major part of the computation is completed. The velocity profiles at grid points of interest can then be recovered using
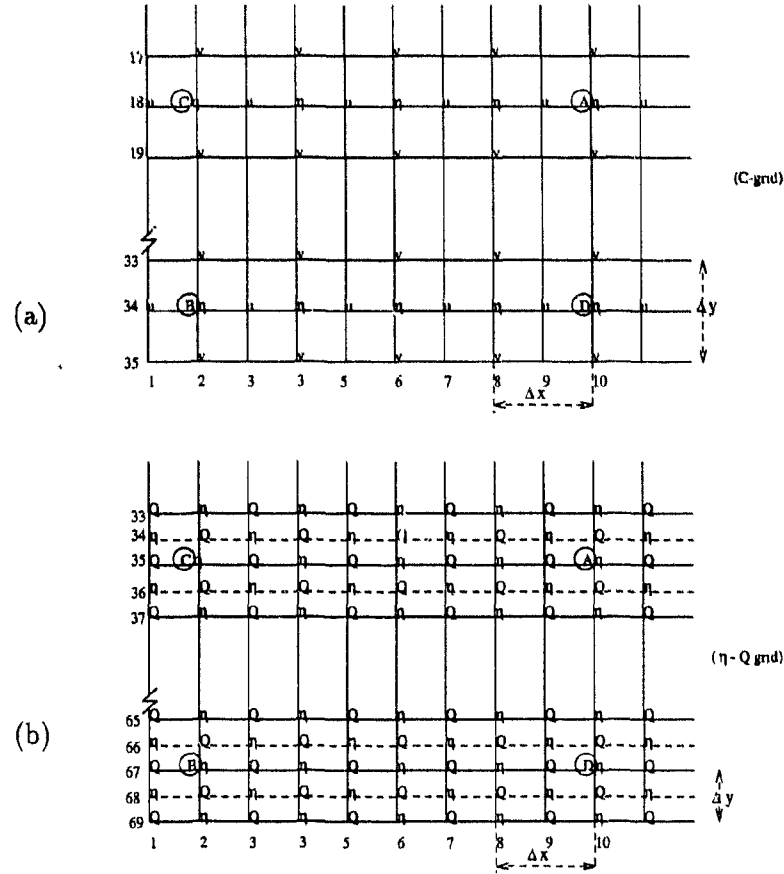
Figure 6.2: Panel (a) is the C-grid used by Heaps (1971) and panel (b) is the $\eta - Q$ grid used in this model. Heaps divided the basin horizontal plane into 35×19 lines, and we divide into 69×19 lines. The double dense grid lines in y-direction is merely to locate the four marked η points, A, B, C, and D, in the lower panel with the same geometrical coordinates as those in the upper panel.
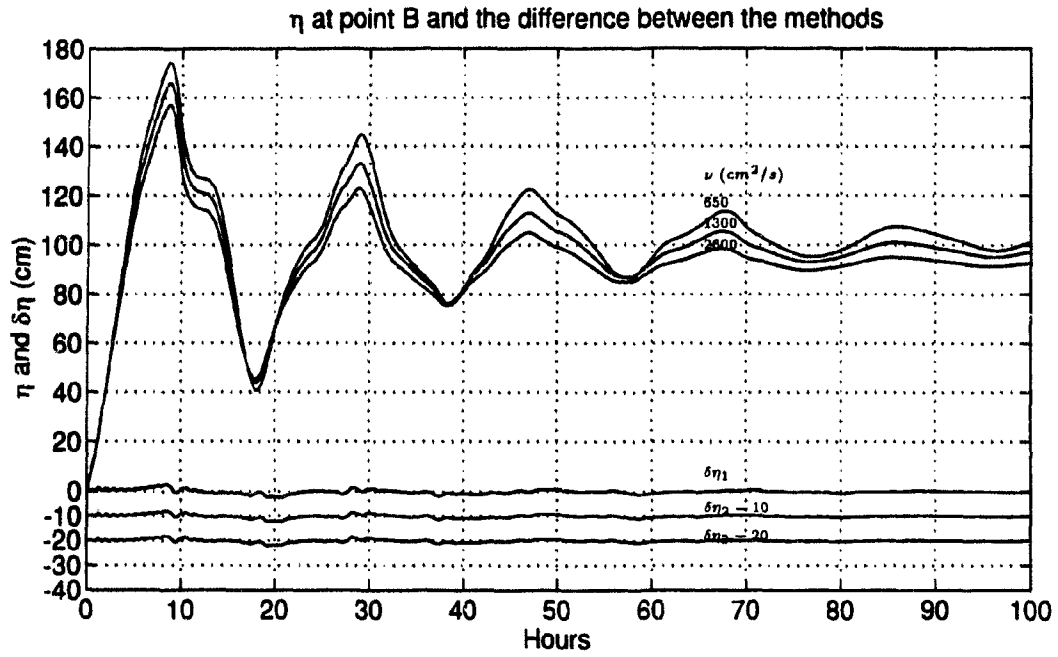
Figure 6.3: Time series of the surface elevation at point B for the first group of tests. Three elevation curves for different values of ν are generated by the transport method (using 2 modes), and compared with the same type of curves generated by Heaps' spectral method (using 10 modes). The difference between the two methods are shown by $\delta\eta_1$, $\delta\eta_2$ and $\delta\eta_3$ ($\delta\eta_1 = |\eta_T - \eta_H|$, where η_T is generated by the transport method and η_H is generated by Heaps' method, for $\nu = 650cm^2/s$, and so on. For clarity, they are offset by -10 in the figure.) The figure demonstrates that the transport method yields results in a good agreement with Heaps' results. (Parameters: $f = 1.22 \times 10^{-4}s^{-1}$, $g = 9.81ms^{-2}$, $\tau = -1.5Pa$, $\rho = 1.025kgm^{-3}$, $\Delta t = 6min$, $h = 65m$, $k = 0.002ms^{-1}$, $\nu = [0.065, 0.13, 0.26]m^2s^{-1}$ $\delta_e/h = [0.50, 0.71, 1.00]$).

u and v at point C generated by the two methods
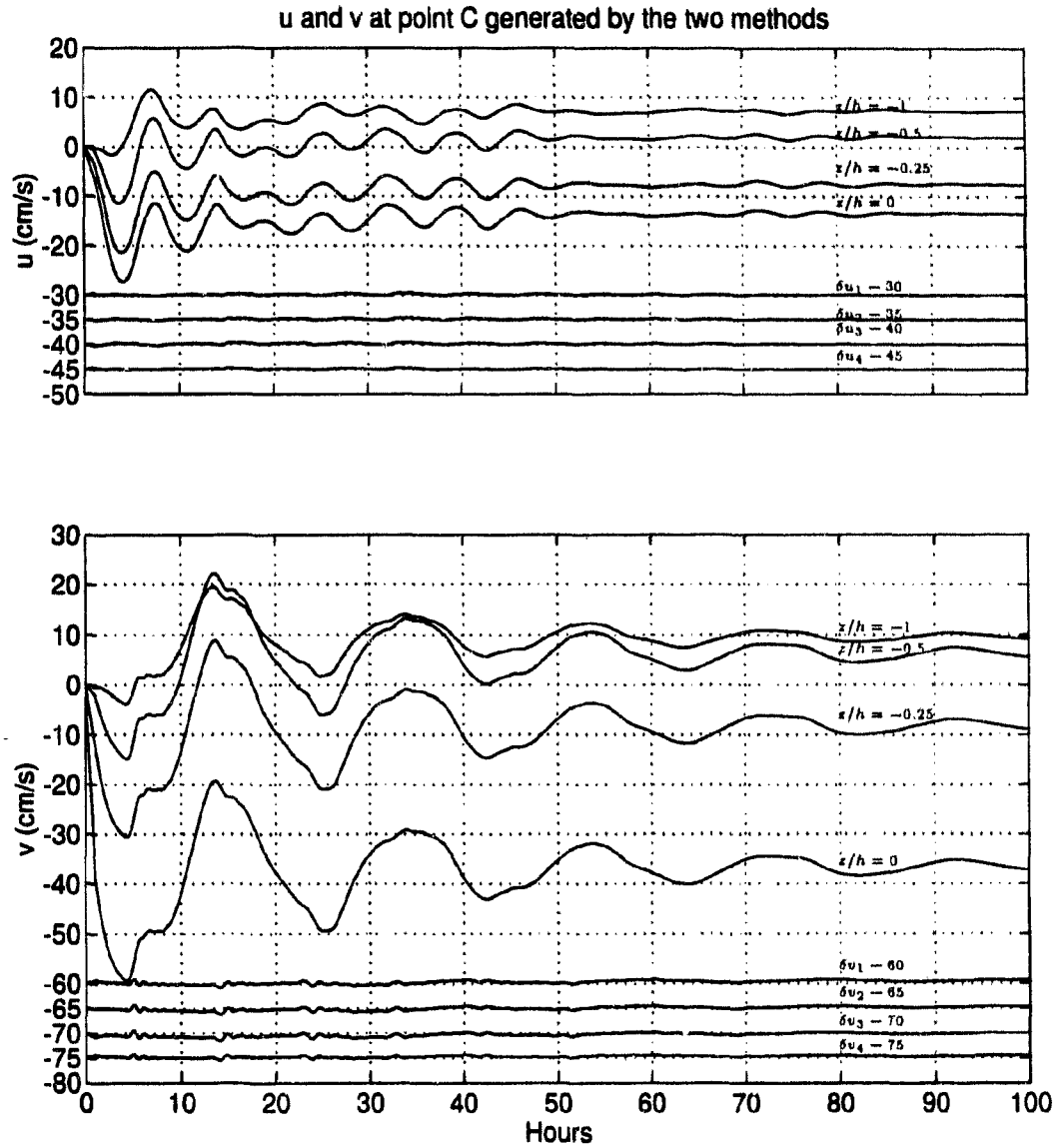
Figure 6.4: Velocity time series at four depths generated by the transport method (using 2 modes) and their difference from those generated by Heaps' method (using 10 modes). The differences are represented by δu_i and δv_i ($i = 1, 2, 3, 4$ for $z/h = 0, -0.25, -0.5 - 1$), offset at the different horizontal lines for clearity. (Parameters are the same as those for figure 2 except for $\nu = 0.065 m^2 s^{-1}$ only.)

the record of $\nabla\eta$ at those points (Table 6.3). Figure (6.4) shows velocity (using 2 modes) recovered at grid point C. The difference between the results of this method and Heaps' spectral method (using 10 modes) are represented by δu_i ($i = 1, 2, 3, 4$ for $z/h = 0, -0.25, -0.50, -1$ and $\delta u = u_H - u_T$, u_H, where denotes u generated by Heaps' method and u_T by transport method), and by δv_i (for clarity, they are offset at different horizontal lines in the figure). The figure shows that the results yielded by the transport method are in satisfactory agreement with those by Heaps' method.

Figure (6.5) shows the effects of using 2, 10 and 20 modes (dashed, dotted, and solid) by Heaps's method (1st and 3rd panels) and the transport method (2nd and 4th panels). From the figure, we can see that for calculating sea surface elevation, 2 modes are enough in both methods. But for calculating velocity, 2 modes are sufficient in the transport method but not in Heaps' method. It should be pointed out that the comparison is under the parameter value of $\delta_e/h = 1/2$. When this ratio gets smaller, the difference in the number of modes used by the two methods will become bigger.

This example illustrates two important features of the transport method. First is the fact that calculation of sea surface elevation requires less modes than calculation of velocity. The transport method takes advantage of this fact by separating the two calculations. There are many practical cases which only require that the velocity profile be calculated at a few grid points, rather than at every grid point. The transport approach allows one to calculate the velocity profiles at only the points of interest. In contrast, Heaps' spectral method requires calculation of the velocity profiles at every grid point, whether they are needed or not. Second, in calculating velocity profiles, the transport method extracts both the surface wind induced Ekman spiral, SE(z), and the slope-induced Ekman spiral, BE(z), from the series, and so the remainder series converges exponentially (see the discussion in Appendix A and Eq. 6.82). Heaps' method does not extract the Ekman spirals, which explains its slow convergence near the surface and bottom. In a word, separation of the two calculations and extraction of the two Ekman spirals is the feature of the transport method.

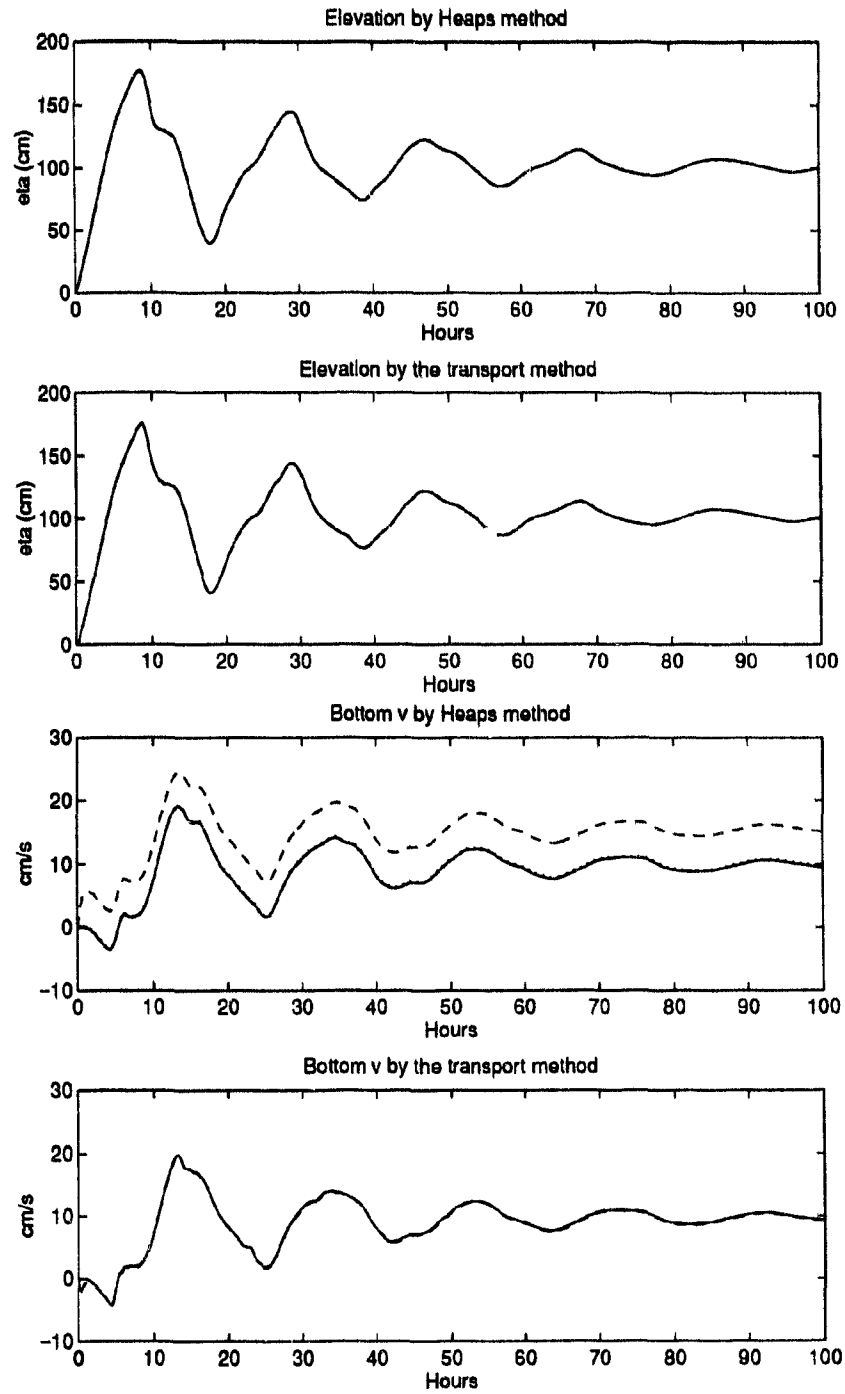Sheng and Thompson (1993) proposed a modification to Heaps's method, which

Figure 6.5: Comparison of convergence rates of the transport method (2nd and 4th panels) and Heaps' spectral method (1st and 3rd panels) (dashed lines: 2 modes, dotted lines: 10 modes, solid lines: 20 modes.)

involves extracting the wind induced surface Ekman spiral from the series. As a result, their method also improves the convergence near the surface effectively. In fact, they found that 4 modes are sufficient for the same Heaps' problem outlined here. However, the slope-induced bottom Ekman spiral is left in the series in their method. Also, their method requires calculation of velocities over the entire model grid. A more theoretical comparison of the transport method with the existing methods will be presented in Section 6.4.

6.3.3 Comparison with analytical solutions at the steady state

For Heaps' rectangular basin problem, an analytical solution for η and $q(z)$ for the steady state can be found. The transport should be zero everywhere in the steady state because of the flat bottom and the uniform wind field. Thus from Eqs. (6.21) and (6.22) one can deduce a relationship between the ultimate sea surface slope, denoted as $\nabla \eta^{(\infty)}$, and the wind stress,

$$\nabla \eta^{(\infty)} \;=\; \frac{D_d}{D_s} \frac{\tau}{gh}, \tag{6.61}$$

which is a constant over the entire basin. Thus the sea surface is a plane and can be described by

$$\eta^{(\infty)} \;=\; \Re\left\{ \frac{D_d}{D_s} \frac{\tau}{gh} \right\} x + \Im\left\{ \frac{D_d}{D_s} \frac{\tau}{gh} \right\} y + c \tag{6.62}$$

in which the constant c can be determined by the fact that the surface at the middle point of the basin should be zero due to the conservation of water mass and the symmetry in basin geometry. For example, if the origin of the coordinate is on the center of the basin, then $c = 0$. The ultimate velocity profile can be calculated by

$$q^{(\infty)} \;=\; \frac{\tau}{f\delta_e} \left[\mathrm{SE}(z) + i\frac{\delta_e}{h} \frac{D_d}{D_s} \mathrm{BE}(z) \right]. \tag{6.63}$$

Jamart and Ozer (1986) gave the steady solutions only for the sea surface slope and the velocity, not for the sea surface itself. However, the fact that the sea surface plane should go through the zero point at the center of the basin completely determines the

whole steady solution. Equations of (6.61), (6.62) and (6.63) are useful in the sense that every new algorithm proposed for spectral methods is first tested in the Heaps' basin.

Figure (6.6) shows a comparison between the theoretical steady state (represented by dashed lines) and the model output at 300 hours after the constant wind is set up (represented by solid lines). As one can see the agreement between the theoretical prediction and model calculations is satisfactory. The top panel of the figure is the time series of the depth averaged velocity, showing that there are no undamped inertial oscillations (Davies, 1987; Hunter and Hearn, 1988) with the transport approach. The bottom panel also shows that adopting the $\eta - Q$ grid automatically eliminates the spurious residual flow problem, (Jamart and Ozer, 1986) which occurs when using an Arakawa C-grid. To appreciate the problem, two of Heaps' (1971) plots are copied in Fig. (6.7). At the steady state the plots show the curved surface elevation contours near the wall and non-vanishing residual flow over the entire domain, which are erroneous results for Heaps' rectangular basin problem. The spurious residual flow problem was noticed by Jamart and Ozer, who proposed a "wet point only" technique to amend the problem. In the $\eta - Q$ grid adopted here, u and v are combined by a complex velocity, $q = u + iv$ (remember Q is the depth integral of q) and are co-located. Therefore there is no need to average the Coriolis forcing, and thus no spurious residual problem arises.

6.4 A comparison of the transport method, the bottom stress method, and the spectral method

To solve the linearized equations of motion, we have three closely related methods at our disposal: the spectral method, the bottom stress method and the transport method. These focus on three related, but different, expansions. The spectral method
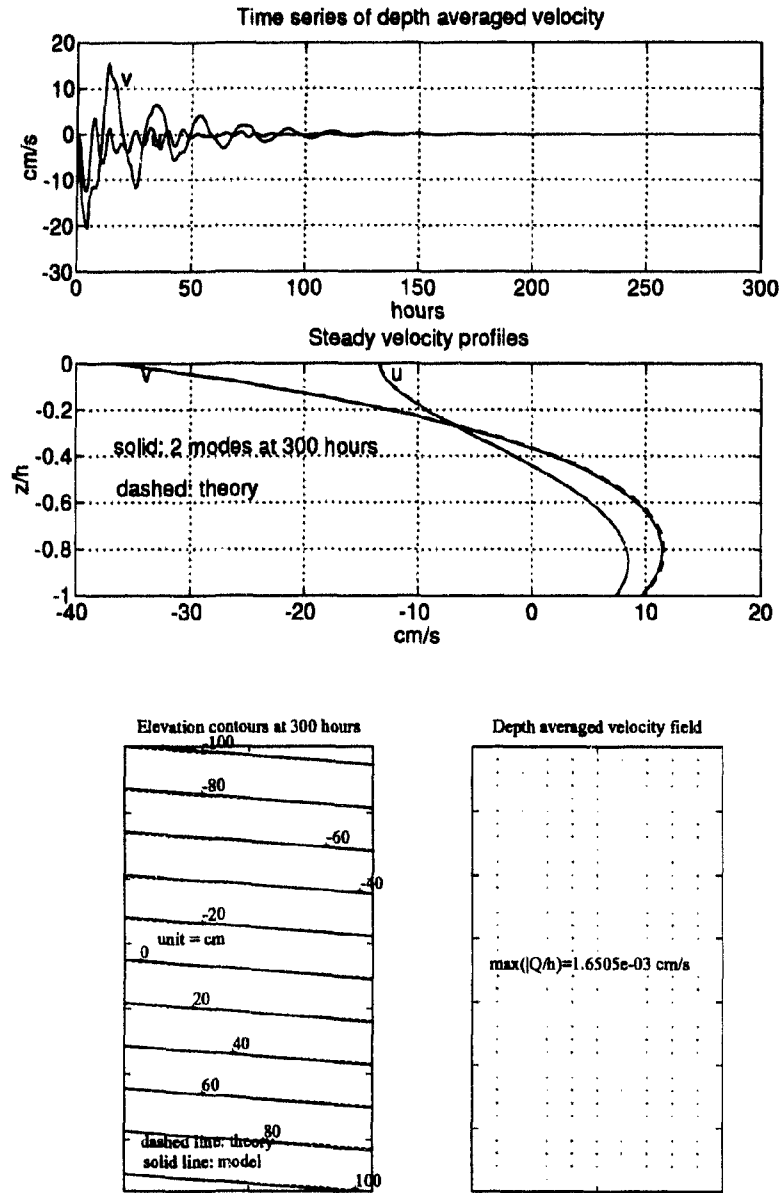
Figure 6.6: The top panel shows the vanishing depth averaged velocity. The middle and the bottom panel are a comparison between the theoretical steady state and the model output at 300 hours. Two modes are used in updating η and Q in the main do-loop and in recovering the velocity profile afterwards. This figure also shows that, in transport method, there is no undamped inertial oscillation or spurious residual flow.
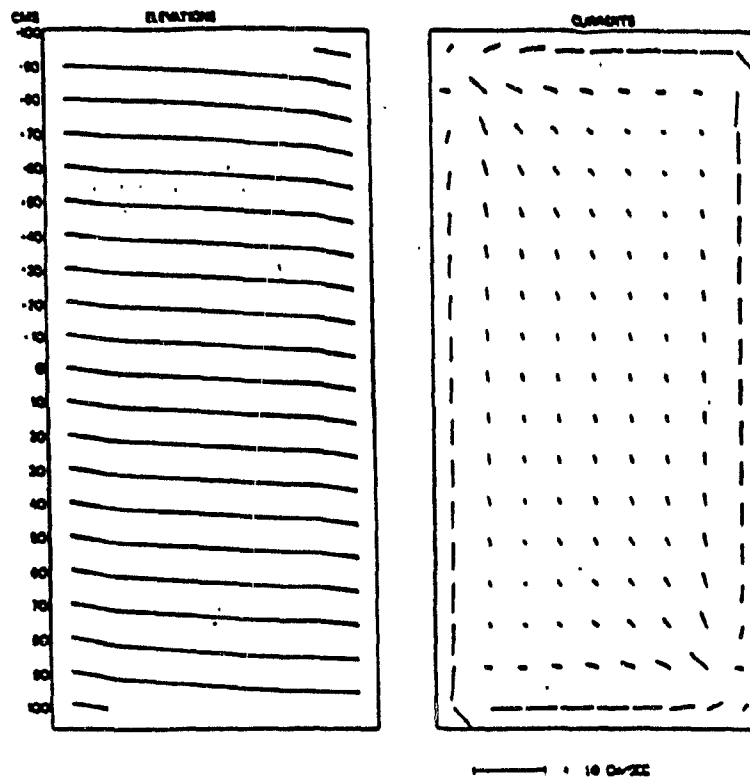
Figure 6.7: A copy of two of Heaps' (1971) plots demonstrates the spurious residual flow problem. For Heaps' rectangular basin problem, the sea surface contours should be straight lines and the depth averaged velocity should vanish over the entire domain at the steady stage. The problem, noticed by Jamart and Ozer (1986), was attributed to the adoption of C-grid. In contrast, the $\eta - Q$ grid does not have such problem (cf. Fig. 3.4).

employs a velocity expansion of form

$$q \sim \Sigma A_n \cos \omega_n z, \tag{6.64}$$

in which the A'_ns are updated at each time step by solving a set of modal equations. In this sense, the spectral method may also be classified as a velocity approach. The bottom stress approach employs a bottom stress expansion, which is a vertical derivative of Eq. (6.64). The transport approach employs a transport series, a vertical integral of Eq. (6.64). Thus three approaches are related in the sense they all deal with the same family of series, but different in the sense that they pick different family members, as is summarized in Table (6.4).

When comparing the convergence rates of two trigonometric series, it is a usual practice to compare the rates at which their coefficients approach zero (e.g., Tolstov, 1962, pages 144-145). In the following discussion, terms like " rate", "speed", "fast" or "slow" are to be understood in this sense.) Now suppose that

$$\frac{A_n}{n^{-p}} = constant \qquad \text{as } n \to \infty, \tag{6.65}$$

for the velocity series, where p is a positive number. (From Eqs. 6.11, 6.13 and 6.15 one can deduce immediately that $p = 2$ when wind is present and $p = 3$ when only the sea surface slope forcing is present.) Then, because $\omega_n h \sim n$, we have

$$\frac{A_n/(\omega_n h)}{n^{-(p+1)}} = constant \qquad \text{as } n \to \infty, \tag{6.66}$$

for the transport series, and we have

$$\frac{A_n(\omega_n h)}{n^{-(p-1)}} = constant \qquad \text{as } n \to \infty, \tag{6.67}$$

for the bottom stress series. Thus, the coefficients of the transport series decreases faster than those of the velocity series and the stress series. Figure (6.8) illustrates this graphically.

From Table (6.4), we can see that the transport approach decouples the rapidly convergent series from the slower series, while the other approaches mix the rapidly

Table 6.4: The relevance and difference of three approaches.

	Transport Approach (This study)	Velocity Approach (Heaps 1971)	Bottom Stress Approach (Jelesnianski 1971)	
Series Involved in the Main Do-loop	— $\sum \frac{A_n}{\omega_n} \sin \omega_n h$ —	$\sum A_n \cos \omega_n z$ $\sum \frac{A_n}{\omega_n} \sin \omega_n h$ —	— $\sum \frac{A_n}{\omega_n} \sin \omega_n h$ $\sum A_n \omega_n \sin \omega_n h$	(velocity) (transport) (stress)
Series Involved in the Velocity Recovery	$\sum (a_n, c_n) e^{-b_n \Delta t} \cos \omega_n z$	—	$\sum (a_n, c_n) e^{-b_n \Delta t} \cos \omega_n z$	
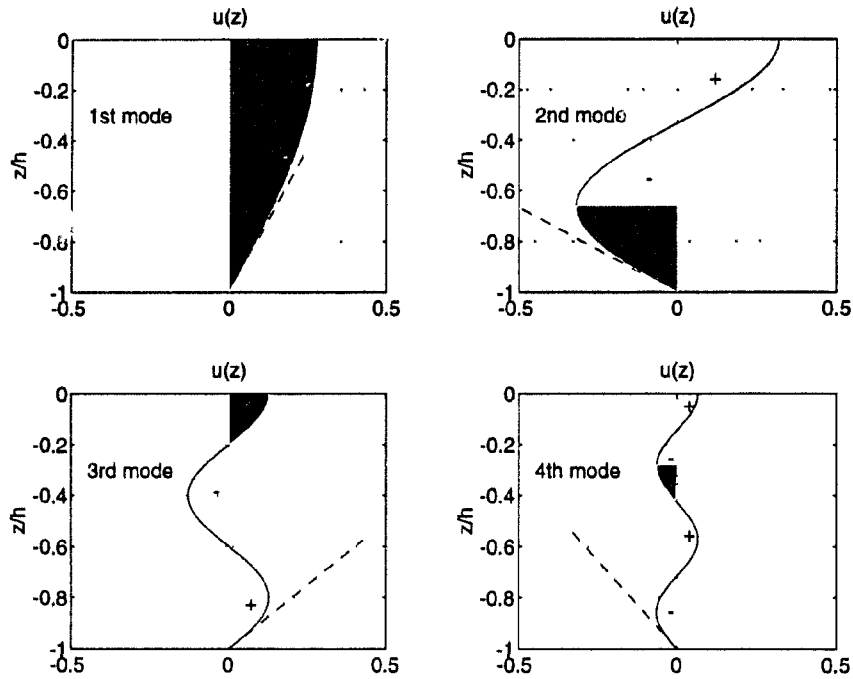
Figure 6.8: This diagram illustrates why the transport series converges the quickest. The net transport due to each mode is represented by the shaded area, and the bottom stresses by the dashed line. The transport in this example is mainly due to the first and the second modes; higher modes contribute little to the transport but may significantly contribute to the velocity and even more to the bottom stress. (The curves shown here are for the velocities of each mode based on the second part of q_d when $t = 0$ and $\delta_e/h = 1/2$ and $\kappa = \infty$.)

convergent series with the slow one. When the calculation process involves summation of two series simultaneously, the convergence rate is controlled by the slowly convergent series. In the velocity approach and in the stress approach the calculation of the elevation is slowed by the calculation of the velocity and the bottom stress respectively. The transport method has no such problem, and the calculation for the elevation proceeds at its own speed. After the elevation calculation is completed , the transport approach employs the analytical formula of Eq. (6.17) to recover the velocity. The main advantage in using the analytical formula is that the formula extracts both the wind-induced surface Ekman spiral and the slope-induced bottom Ekman spiral so that the remainder converges exponentially (cf. Eqs. 6.4, 6.5, 6.82, and Table 6.3).

There are two additional advantages in using the analytical formula. First, one can use a different time step than that used in the main do-loop. For an explicit scheme, the time step in the main do-loop, say Δt_M, is restricted by the CFL condition and can be very small when water is very deep. In this case, one might consider using a multiple of Δt_M as the time step for the velocity calculation. Figure (6.9) shows the effects on the velocity recovery of using a different time step as well as a different number of modes. Second, as has been stated in the preceding section, the transport approach allows one to calculate the velocity profiles at only the points of interest. Any of these advantages results in a great saving of computational workload, and their combination saves even more. The bottom stress shares the same advantages in the velocity recovery, but it needs the greatest numbers of modes in the main do-loop, since it employs the most slowly convergent series.

Another feature of the transport approach is that it solves only one equation (the continuity equation) numerically, rather than three, thus the numerical task is made easier. Lynch et al. (1987, 1992) proposed a method for solving the 3-D linearized equations of motion, which essentially also solves a single Helmholtz-like equation for η. However, arbitrary time dependent motion is replaced by a single harmonic motion in their work. In this work, there is no restriction on the time dependence of
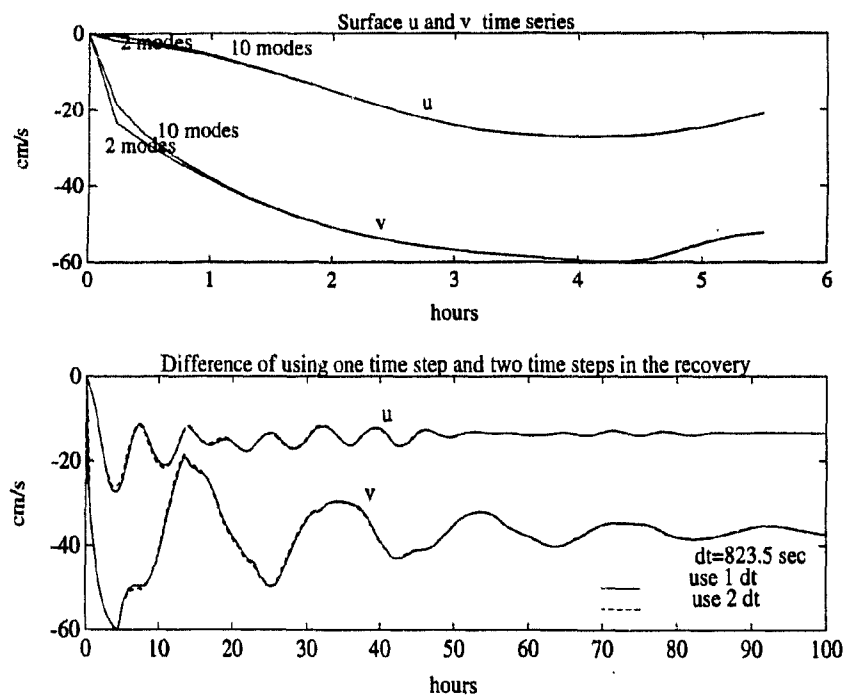
Figure 6.9: Since the transport method separates the calculation of the transport and elevation from that for the velocity, it is permissible to use a different number of modes and a different time step in the velocity recovery. This can be an advantage in reducing the computational workload in most cases. This figure shows the effects in using a different number of modes and a different time step. (Note, because of the factor $e^{-b_n \Delta t}$, $(b_n \sim n^2)$, the value of N is also affected by the choice of Δt. In a slowly varying problem, a large value of Δt can be chosen and the value of N can be reduced accordingly given a fixed truncation error. In a rapidly changing problem, a small value should be chosen for Δt, and thus the value of N should be increased. The transport method flexibly accommodates these needs.)

the motion, the forcing function can be arbitrary.

6.5 Comments on the velocity split form in the spectral method

The purpose of this chapter is to implement Welander's transport approach. However, one point, which is closely related to the recent efforts to improve the convergence of velocity in the spectral method, warrants further discussion. It was found that Heaps' classical spectral method converges very slowly (e.g., Davies, 1983; Lardner, 1990) near the surface when there is non-zero wind stress on the surface. This is because Heaps' spectral method uses cosine functions. The contradiction of zero derivative of the cosine functions and non-zero wind stress on the sea surface ($z = 0$) causes the slow convergence. Early efforts to accelerate the convergence used some other base functions whose derivatives on the surface are not zero, like Chebyshev and Legendre polynomials (Davies and Owen, 1979). However, these functions cost more computational workload in their evaluations than the simple cosine functions.

Recent efforts have split the velocity into two parts, a prescribed part, and a remainder series,

$$q = \Psi(z) + \sum A_n \cos \omega_n z, \qquad (6.68)$$

in which $\Psi(z)$ is a prescribed function, and the coefficients of the remainder series, A_n, need to be updated by numerically solving a set of modal equations. The prescribed part, $\Psi(z)$, accommodates the non-zero wind stress. The convergence rate of the remainder series depends strongly on the choice of form for $\Psi(z)$. Different authors (Lardner, 1990; Zitman, 1992; Davies, 1991; Davies, 1992; Sheng and Thompson, 1993) have proposed different forms of $\Psi(z)$, as summarized in Table (6.5). A general formula for all the previously proposed forms can be written as

$$\Psi(z) = F_s \Psi_s(z) + F_b \Psi_b(z) \qquad (6.69)$$

where Ψ_s and Ψ_b are two prescribed profiles and F_s and F_b are two depth independent quantities, usually related to the surface stress and the bottom stress respectively.

An alternative expression for Eq. (6.17) is

$$q = \frac{\tau(t)}{f\delta_e}\text{SE}(z) + \frac{ig\,\nabla\eta(t)}{f}\text{BE}(z)$$
$$-\sum_{n=0}^{\infty}\left[\frac{a_n}{f\delta_e}\frac{\partial\tau}{\partial t} + c_n\frac{ig}{f}\frac{\partial\nabla\eta(t)}{\partial t}\right] * e^{-b_n t}\cos\omega_n z. \tag{6.70}$$

This form suggests that perhaps a more suitable form for $\Psi(z)$ is

$$\Psi(z) = \frac{\tau(t)}{f\delta_e}\text{SE}(z) + i\frac{g\,\nabla\eta(t)}{f}\text{BE}(z), \tag{6.71}$$

where $\text{SE}(z)$ and $\text{BE}(z)$ are given by Eqs. (6.6) and (6.7) or can be obtained numerically for arbitrary eddy viscosity $\nu(z)$. In a system (such as Heaps' basin) which permits an eventual steady state, this form is clearly optimal. When t is sufficiently large, any other form of $\Psi(z)$ will cause the remainder series to contain a non-vanishing part, i.e.,

$$\sum A_n\cos\omega_n z = \left[\frac{\tau}{f\delta_e}\text{SE}(z) - F_s\Psi_b(z) + i\frac{g\,\nabla\eta}{f}\text{BE}(z) - F_b\Psi_b(z)\right]. \tag{6.72}$$

The difference between Eqs. (6.69) and (6.71) is then buried in the remainder series. Given a truncation error tolerance, one needs to sum a certain number of modes to compute this buried part no matter how much time passes. If one chooses Eq. (6.71) for $\Psi(z)$, then one will not need to sum over any modes when t is sufficiently large.

For time dependent cases, since the external forces, $\tau(t)$, and $\nabla\eta(t)$, can be arbitrary functions of time, let us turn to considering single frequency forcing. Conclusions from the single frequency study should be illuminating for arbitrary forcing since the latter can be decomposed into different frequencies. So assume harmonic time-dependence with the frequency Ω,

$$\tau(t) = \tau e^{i\Omega t} \tag{6.73}$$

$$\nabla\eta(t) = \nabla\eta e^{i\Omega t} \tag{6.74}$$

Table 6.5: Various forms suggested by different authors for $F_a\Psi_a(z)+F_b\Psi_b(z)$ in order to accelerate the convergence of the remainder series.

Authors	F_a	$\Psi_a(z)$	F_b	$\Psi_b(z)$	Note
1) Lardner 1990	$\frac{\tau_a h}{\nu}$	$1+\frac{z}{h}+\frac{\nu}{\kappa h}$	0	0	
2) Zitman 1992	$\frac{\tau_a h}{\nu}$	$\frac{\sin\gamma_1 z}{\gamma_1 h}$	0	0	note 1
3a) Davies 1991, 1992	$\frac{\tau_a h}{\nu}\beta$	$\begin{cases} \frac{(z+z_0)^2}{2hz_0} & z\in[-z_0,\,0] \\ 0 & z\in[-h,\,-z_0] \end{cases}$	$\frac{\tau_a h}{\nu}\beta$	$\begin{cases} 0 & z\in[-z_0,\,0] \\ \frac{(z+z_0)^2}{2(z_0-h)h} & z\in[-h,\,-z_0] \end{cases}$	$z_0>0$ note 2
3b) Davies 1991, 1992	$\frac{\tau_a h}{\nu}\beta$	$\left(\frac{1}{2}\frac{z^2}{h^2}+\frac{z}{h}+\frac{1}{3}\right)$ $-\frac{2}{\pi^2}\sum_{n=1}^{N-1}\frac{1}{n^2}\cos\frac{n\pi}{h}z$	$\frac{\tau_a h}{\nu}\beta$	$\left(\frac{1}{2}\frac{z^2}{h^2}-\frac{1}{6}\right)$ $-\frac{2}{\pi^2}\sum_{n=1}^{N-1}\frac{(-1)^n}{n^2}\cos\frac{n\pi}{h}z$	
4) Sheng & Thompson 1993	$\frac{\tau_a}{f b_z}$	$SE(z)$	0	0	
5) Xu This study	$\frac{\tau_a}{f b_z}$	$SE(z)$	$i\frac{\tau_a\nabla\eta}{f}$	$BE(z)$	

Note 1: γ_1 is the first positive root of $\gamma h\cos\gamma h + \frac{\kappa h}{\nu}\sin\gamma h = 0$;

Note 2: $0 < \beta \le 1$, introduction of this free parameter is for numerical stability (see Davies, 1992);

after which combination of Eqs. (6.70), (6.68), and (6.69) gives

$$\sum_{n=0}^{\infty} A_n \cos \omega_n z = \left[\frac{\tau e^{i\Omega t}}{f \delta_e} \mathrm{SE}(z) - F_s \Psi_s(z) + i \frac{g \nabla \eta(t) e^{i\Omega t}}{f} \mathrm{BE}(z) - F_b \Psi_b(z) \right]$$

$$- \sum_{n=0}^{\infty} \frac{i\Omega}{i\Omega + b_n} \left[a_n \frac{\tau e^{i\Omega t}}{f \delta_e} + c_n \frac{ig}{f} \nabla \eta e^{i\Omega t} \right] \cos \omega_n z$$

$$+ \sum_{n=0}^{\infty} \frac{i\Omega}{i\Omega + b_n} \left[a_n \frac{\tau e^{i\Omega t}}{f \delta_e} + c_n \frac{ig}{f} \nabla \eta e^{i\Omega t} \right] e^{-b_n t} \cos \omega_n z$$

$$- \sum_{n=0}^{\infty} \left[a_n \frac{\tau}{f \delta_e} + c_n \frac{ig}{f} \nabla \eta \right] e^{-b_n t} \cos \omega_n z. \tag{6.75}$$

This equation provides a means for a theoretical assessment of all the previously proposed forms of the basis functions of $\{\cos \omega_n z\}$ which are the eigenfunctions of Eqs. (6.1) and (6.2). If one chooses Eq. (6.71) for $\Psi(z)$, one will find (with reference to Eqs. 6.11 to 6.15) that the coefficient of the remainder series is described by,

$$A_n \sim \max \left(\frac{\Omega/f}{n^4}, \frac{\Omega/f}{n^5}, \frac{e^{-n^2 t}}{n^2}, \frac{e^{-n^2 t}}{n^3} \right) \tag{6.76}$$

(in which the first and the third terms are related to the wind forcing and the second and fourth terms are related to the pressure forcing). When $t > 0$, the last two terms in the parentheses approach zero exponentially as $n \to \infty$, leaving the first term (or the second term when $\tau(t) = 0$) as the controlling term. Substituting all the previously proposed forms (Lardner, 1990; Zitman, 1992; Davies, 1991; Davies, 1992; Sheng and Thompson, 1993) in Eq. (6.75) reveals that

$$A_n \sim \frac{1}{n^3} . \tag{6.77}$$

Thus, the form of Eq. (6.71) is preferable to the others as a prescribed part of the velocity under the basis of the eigenfunctions to the problem of Eqs. (6.1) and (6.2). (For other basis functions, like $\{\cos \frac{n\pi}{h} z\}$, which are not the eigenfunctions of the problems of Eqs. (6.1) and (6.2) when $\kappa \neq 0$, whether this preference still holds needs further investigation.)

6.6 Conclusion

Regarding the pressure gradient force in the two linearized momentum equations as a local external force, on··· tains two step force responses of the local Eulerian velocity. These responses can be expressed analytically in terms of unit constant wind stress and unit constant pressure gradient. The coefficients in the expression, however, may either have an analytical dependence on the mode number, n, and the system parameters $(\delta_e/h, \kappa)$, or have numerical values, depending on the form of the eddy viscosity profile $\nu(z)$, and the density profile $\rho(z)$. The response to arbitrary wind and pressure forcing can be obtained by convolving these two forces with the time derivatives of the two step force responses. Thus, a full velocity profile, $q(t, z; \nabla\eta, \tau)$, is analytically extracted. Our knowledge of the system would be complete if $\eta(t, x, y)$ (hence $\nabla\eta(t, x, y)$) were known. Thus, the key point is finding the solution for $\eta(t, x, y)$. To get $\eta(t, x, y)$, the transport method solves the continuity equation numerically (where the transport is supplied by the depth integration of the velocity profile) instead of solving a set of depth averaged equations of motion. By doing so, the numerical task is reduced since only one equation needs to be finite differenced and integrated and, more importantly, the convergence rate is enhanced, since high modes do not contribute to the transport as much as they do to the velocity or the bottom stress.

6.7 Appendix A: Velocity recursion scheme and acceleration of velocity convergence using Equations (19) and (20)

The recursion scheme of Eq. (6.42) can apply to the response in velocity, stress and transport when one substitutes the corresponding $C(z)$, $\phi_n(z)$ and b_n. In terms of

velocity, the recursion scheme is expressed as

$$
\begin{aligned}
\lambda_n &= e^{-b_n \Delta t} \\
r_{nF} &= 0 \\
r_{n1\tau} &= \tfrac{I_\tau}{f\delta_s} a_n \cos(\omega_n z)(1 - \lambda_n) \\
r_{n1\eta} &= i\tfrac{g I_{\nabla\eta}}{f} c_n \cos(\omega_n z)(1 - \lambda_n) \\[2mm]
r_{nF}^{(j+1)} &= r_{nF}^{(j)} \lambda_n + \tau^{(j)} r_{n1\tau} + \nabla\eta^{(j)} r_{n1\eta} \\
q^{(j+1)} &= \textstyle\sum_{n=0}^{N} r_{nF}^{(j+1)} \\
& \quad (j = 0, 1, 2, ...)
\end{aligned}
\tag{6.78}
$$

where q takes the place of R_F in Eq. (6.42) and a_n and b_n are given by Eqs. (6.11) and (6.12).

As we can see from the above, in the summation of the series

$$
\sum_{n=0}^{\infty} r_{nF}^{(j+1)},
\tag{6.79}
$$

the convergence rate is controlled by the series

$$
\sum_{n=0}^{\infty} a_n \cos(\omega_n z), \qquad \sum_{n=0}^{\infty} c_n \cos(\omega_n z)
\tag{6.80}
$$

rather than

$$
\sum_{n=0}^{\infty} a_n \cos(\omega_n z)\lambda_n, \qquad \sum_{n=0}^{\infty} c_n \cos(\omega_n z)\lambda_n.
\tag{6.81}
$$

The latter converges much faster than the former, since the factor of λ_n decreases exponentially as n increases. We obviously want to take advantage of this fact. This can be achieved by using Eqs. (6.18) and (6.19) to extract the slowly converging parts from the summations. Thus we can derive the following more rapidly convergent

scheme for the velocity recovery.

$$
\begin{aligned}
\lambda_n &= e^{-b_n \Delta t} \\
r_{nF} &= 0 \\
r_{n1\tau} &= \frac{I_\tau}{f \delta_e} a_n \cos(\omega_n z)(1 - \lambda_n) \\
r_{n1\eta} &= i \frac{g I_{\nabla \eta}}{f} c_n \cos(\omega_n z)(1 - \lambda_n) \\
R_{1\tau} &= \frac{I_\tau}{f \delta_e} \left[\mathrm{SE}(z) - \sum_{n=0}^{N} a_n \cos(\omega_n z) \lambda_n \right] \\
R_{1\eta} &= \frac{g I_{\nabla \eta}}{f} \left[\mathrm{BE}(z) - \sum_{n=0}^{N} c_n \cos(\omega_n z) \lambda_n \right] \\[2mm]
q^{(j+1)} &= \sum_{n=0}^{N} r_{nF}^{(j)} \lambda_n + \tau^{(j)} R_{1\tau} + \nabla \eta^{(j)} R_{1\eta} \\
r_{nF}^{(j+1)} &= r_{nF}^{(j)} \lambda_n + \tau^{(j)} r_{n1\tau} + \nabla \eta^{(j)} r_{n1\eta} \\
& \quad (j = 0, 1, 2, \dots)
\end{aligned}
\tag{6.82}
$$

6.8 Appendix B: Extension of the approach

The two step force velocity responses are obtained under the assumption of constant eddy viscosity and constant density. Discussed in this appendix is the extension of the transport approach to the cases of arbitrary but time invariant eddy viscosity $\nu(z)$ and density anomaly $\rho = \rho_0[1 + \epsilon(x, y, z)]$, where $\epsilon(x, y, z)$ stands for the anomaly.

6.8.1 The case of arbitrary depth-dependent $\nu(z)$

When $\nu = \nu(z)$, the formal solution (like Eq. 6.4 or 6.5) to the step force velocity response still holds

$$
q(t, z; I) = C(z) - \sum_{n=0}^{\infty} A_n e^{-(\gamma_n^2 + i)ft} Z_n(z)
\tag{6.83}
$$

where $C(z)$ is a steady current (wind induced or slope induced), and Z_n and γ_n are eigenfunctions and eigenvalues values defined by

$$
\frac{\partial}{\partial z}\left(\nu(z) \frac{\partial Z}{\partial z} \right) = -f \gamma_n^2 Z
\tag{6.84}
$$

$$
\left. \frac{\partial Z}{\partial z} \right|_{z=0} = 0, \qquad Z|_{z=-h} = 0
\tag{6.85}
$$

and A_n are Fourier coefficients with the respect to the eigenfunctions. The steady velocity $C(z)$ should be easy to obtain by numerical integration. If the eigenfunctions and eigenvalues are known, then the Fourier coefficients A_n can be obtained by numerical evaluation of

$$A_n = \frac{1}{\|\cdot\|} \int_{-h}^{0} C(z) Z(z) dz \qquad (6.86)$$

where $\|\cdot\|$ denotes the norm of Z_n, and Eq. (6.83) can be evaluated, and the step force responses in velocity determined. Therefore the main issue here is how to solve the Sturm-Liouville eigenvalue problem given by Eqs. (6.84) and (6.85). When $\nu(z)$ is of some specified form, such as a linear function, exponential, power, etc., there exist various analytical solutions to Eqs. (6.84) and (6.85), (Jordan, 1980) . What is needed here is a numerical solution of the eigenvalue problem when $\nu(z)$ does not admit an analytical solution.

Davies solved the eigenvalue problem using a Galerkin method by expanding each of the eigenfunction in terms of a set B-spline functions (Davies, 1983) or alternatively by using the Runge-Kutta-Merson iteration method (Davies, 1986). In the following a direct way for solving the problem is presented. Without loss of generality, let us consider the following form of the eigenfunction problem:

$$(\nu Z')' = -\ell Z \qquad (6.87)$$

$$Z'(0) = 0, \qquad Z(-1) = 0, \qquad (6.88)$$

which can be regarded as non-dimensional forms of Eqs. (6.84) and (6.85). Dividing $[-1, 0]$ into $(n-1)$ equal parts and applying centered differences on Eq. (6.87) results in

$$AZ = -\ell Z \qquad (6.89)$$

where

$$A = \frac{1}{(\Delta z)^2} \begin{bmatrix} -\nu_{5/2} & \nu_{5/2} & 0 & 0 & \cdots & 0 \\ \nu_{3/2} & a_2 & \nu_{5/2} & 0 & \cdots & 0 \\ 0 & \nu_{5/2} & a_3 & \nu_{7/2} & \cdots & 0 \\ \vdots & \vdots & \ddots & \ddots & \ddots & \vdots \\ 0 & 0 & \cdots & \nu_{n-3/2} & a_{n-1} & \nu_{n-1/2} \\ 0 & 0 & \cdots & 0 & \nu_{n-1/2} & a_n \end{bmatrix} \tag{6.90}$$

$$a_i = -(\nu_{i-1/2} + \nu_{i+1/2}) \qquad \text{(for } i = 2 \dots n) \tag{6.91}$$

$$Z = [Z_1 \ Z_2 \ \dots \ Z_n]^T \tag{6.92}$$

where $[Z_1 \ Z_2 \ \dots Z_n]$ is a set of values of the eigenfunction evaluated at $[z_1 \ z_2 \ z_3 \ \dots z_n]$. Thus the Sturm-Liouville problem has been turned into a matrix eigenvalue problem. An introduction to this numerical method of solving Sturm-Liouville problems can be found in Zwillinger (1989).

For illustration, a computational example is supplied in which the eddy viscosity profile is specified in two layers and the analytical solutions for the eigenvalues and eigenfunctions were obtained by Heaps (1981a, 1981b) . Figure (6.10) shows the eddy viscosity profile and a comparison of the first five eigenfunctions calculated analytically and numerically. The numerical solution of the eigenvalue problem gives a satisfactory approximation to the analytical one. Also, we can see that the bottom logarithmic layer is well resolved.

6.8.2 The case of non-uniform density field, $\rho = \rho_0[1 + \epsilon(x, y, z)]$

In this case, there will be an extra component, say q', compared with the case of barotropic pressure and constant eddy viscosity, in the step force velocity response contributed by the baroclinic pressure force described by

$$\frac{\partial q'}{\partial t} + ifq' = -g \ \nabla \ \eta_d(x, y, z) + \nu \frac{\partial^2 q'}{\partial z^2} \tag{6.93}$$
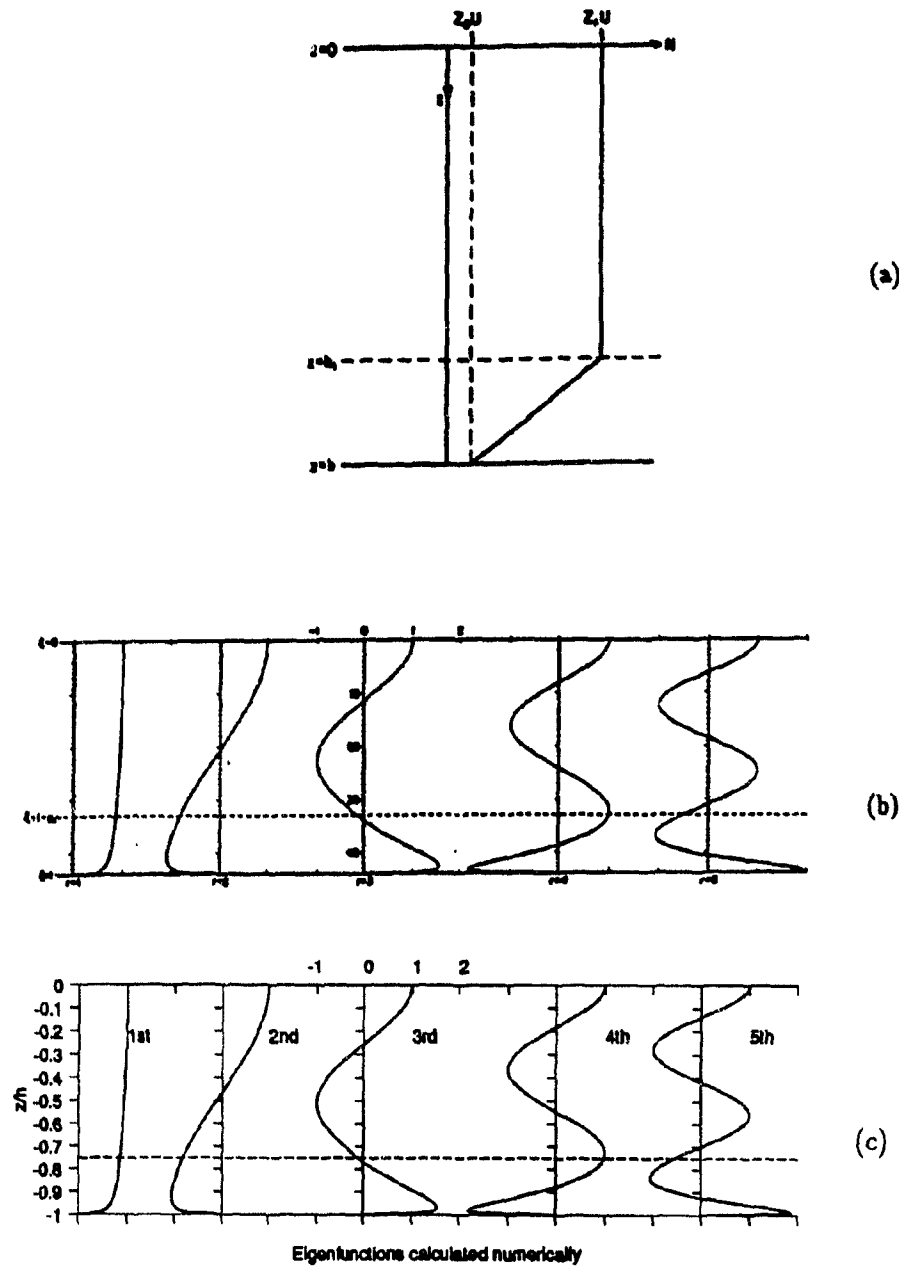
Figure 6.10: The top panel is the eddy viscosity used by Heaps (1981a, b), and the middle panel is the first 5 eigenfunction obtained analytically by Heaps (scanned from Heaps' paper). The bottom panel is the first 5 eigenfunctions calculated numerically by using the method described in the text.

where

$$\eta_d = \int_z^0 \epsilon dz,$$ (6.94)

subject to the same boundary condition as those in Eqs. (6.2). The solution can be found

$$q' = C'(z) - \sum_{n=0}^{\infty} A_n e^{-(\gamma_n^2 + i)ft} \cos \omega_n z,$$ (6.95)

where

$$A_n = \frac{2}{h} \int_{-h}^0 C'(z) \cos \omega_n z \, dz$$ (6.96)

and $C'(z)$ is a steady solution of Eq. (6.93), which may be found by using Green's function method. The transport approach introduced above then can be followed.

Chapter 7

Summary and Discussion

Two topics related to shelf dynamics are covered by this thesis: the introduction of the wave forcing into the shallow water dynamics, and the presentation of a new numerical method, the transport approach, for solving the 3D linearized equations of motion which govern the dynamics.

The wave force originates from a combination of the effect of the earth's rotation on the Stoke's drift and the frictional effects of the surface and bottom wave boundary layers. Unlike classical wave radiation stresses whose existence depends on the horizontal gradient of wave energy, these two types of wave stresses exist wherever there are surface waves. The size of these wave induced stresses may not be negligible compared with typical wind stresses. Chapter 2 derives an Eulerian description of the wave stress. Dealing with the mean wave force can involve complicated and lengthy algebra because of the nature of non-linearity, and as a result the Lagrangian form of the equations of motion is often used. On the other hand, it is desirable to incorporate this wave force into shelf circulation models without altering the usual formulation of equations (i.e., the Eulerian description). Therefore, this thesis makes a special effort to simplify the derivation of the wave force while retaining the usual Eulerian equations.

Chapter 3 establishes a set of general 3D equations which includes both the classical wave radiation stresses and the stress derived in Chapter 2. Using the assumptions

144

of small Rossby number and horizontal homogeneity of the wave force, the general equations are simplified to a linearized system which allows the study to focus on the mean flow driven by the waves.

A methodology is introduced and used throughout the thesis whereby the response of a local Eulerian water column to a step function force is first determined, then a time convolution technique is used to establish the response to an arbitrary force. Chapter 4 studies the response to a step function of wave force in detail. The early work of Longuet-Higgins, Ursell, Hasselmann and Madsen were shown to be limiting cases of the solutions found here. The addition of wave-induced flow to wind-induced flow enriches the vertical structure of the total flow, as it introduces another vertical scale ratio, namely the ratio of Stokes depth over the water depth, δ_{st}, in addition to the existing ratio of Ekman depth over the water, δ_e/h. Implications of the wave-driven flow are further discussed. Besides the generation mechanism for inertial oscillations proposed by Hasselmann (1970), they include the mirror image wave-induced Eulerian return flow compensating the Stokes drift, a possible explanation for the alongshore momentum imbalance in the coastal experiments, and the dependence of wave forcing on large scale topography.

Experimental work testing the existence of the wave forces has lagged theoretical work. For the virtual wave stress, Longuet-Higgins designed a laboratory experiment and demonstrated its existence (Longuet-Higgins, 1959). Applied to the real ocean, this virtual wave stress should induce a surface Ekman flow as if the same magnitude of wind stress were applied. However there appears to be no studies verifying the existence of this type of flow in the field. As to the Coriolis induced wave stress, even its laboratory confirmation has not yet been reported, let alone field observations. Nevertheless, Chapter 5 of this thesis uses a pre-existing data set, the CASP data, and investigates whether there is any flow that might be driven by the wave stresses (the Coriolis induced stress and the virtual stress). Although similar patterns are found in both the observed cross-shore flow and the simulated wave-driven flow, this analysis cannot determine whether waves played a role in the observed flow, or if the

patterns are due to aliasing effects of wind (winds and waves are correlated in the CASP data). The results from this preliminary exploration emphasises the need for an experiment specially designed for investigating flows driven by Coriolis-induced wave stress.

Chapter 6 provides a new method for numerically solving the 3D linearized equations for the shelf circulation. The method first treats all the local forces, including the pressure gradient, as constant forces of unit magnitude and zero angle with respect to the chosen x-axis. Under this treatment, the local water response to these special forces is easy to obtain. The responses to arbitrary forces are obtained by using a time convolution technique. The method then combines these step function responses in a global model to complete the description of the sea surface elevation field. The philosophy of this method originates from Welander (1957) but has not previously been implemented. As is demonstrated in Chapter 6, the method brings a substantial decrease in the computational workload. This can be valuable for a problem involving many iterations of the solutions, such as data assimilation. In developing and testing the method, the wave forcing is not included. This simplifies the computation and makes possible the direct comparison with previous model results (in which the wave force was not present). The method itself easily allows the addition of the wave forcing. It also allows the addition of a baroclinic force (specified diagnostically) due to a non-homogeneous density field.

The development of the method also produced two by-products, which may have value for any non-time convolution method. These are the $\eta - Q$ grid scheme, and the extraction of both the wind induced surface Ekman profile and the pressure induced bottom Ekman profile as a prescribed part of the velocity profile. The former automatically eliminates the spurious residual flow problem (Fig. 6.6), and the latter is an optimal form for the specified velocity profile in order to accelerate the convergence of the solution (Table 6.5).

The method is limited to a linearized system. However, since the Rossby number for oceanic motion is often small, the linearized system is a powerful tool for modelling

many physical oceanography problems, including tidal flows, storm surges, and shelf circulation. Using a perturbation technique, the method can, in principle, be extended to a weakly non-linear dynamic system.

Bibliography

[1] Allen J.S. and R.L. Smith. On the dynamics of wind-driven shelf currents. *Phil. Trans. Roy. Soc. London*, A302:617-634, 1981.

[2] Anderson C. and P. Smith. Oceanographic observations on the Scotian Shelf during CASP. *Atmosphere-Ocean*, 27(1):130-156, 1989.

[3] Andrews D. G. and M. E. McIntyre. An exact theory of nonlinear waves on a Lagrangian-mean flow. *J. Fluid Mech.*, 89(4):609-646, 1978.

[4] Batchelor G.K. *Fluid Dynamics*. Cambridge University Press, 1967.

[5] Bowen A.J., D.L. Inman, and V. P. Simmons. Wave 'set-down' and set-up. *J. Geophys. Res.*, 73(8):2569-2577, 1968.

[6] Chapman D.C. Numerical treatment of cross-shelf boundaries in a barotropic coastal ocean model. *Journal of Physical Oceanography*, 15:1060-1075, 1985.

[7] Cox C. S. Measurement of slopes of high-frequency wind waves. *J. Mar. Res.*, 16:199-225, 1958.

[8] Csanady G.T. *Circulation in the Coastal Ocean*. D.Reidel Publishing Company, 1982.

[9] Davies A.M. and A. Owen. Three dimensional numerical sea model using the Galerkin method with a polynomial basis set. *Appl. Math. Modelling*, 3:421-428, 1979.

148

[10] Davies A.M. Formulation of a linear three-dimensional hydrodynamic sea model using a Galerkin-eigenfunction method. *Int. J. Numerical Meth. Fluids*, 3:33-60, 1983.

[11] Davies A.M. On the determination of vertical structure functions for time-dependent flow problems. *Tellus*, 38 A:462–477, 1986.

[12] Davies A.M. Spectral models in continental shelf sea oceanography. In N. S. Heaps, editor, *Three-Dimensional Coastal Ocean Models*, pages 245-255. American Geophysical Union, Washington, D.C., 1987.

[13] Davies A.M. On formulating two-dimensional vertical integrated hydrodynamic numerical models with an enhanced representation of bed stress. *J. Geophys. Res.*, 93(C2):1241–1263, 1988.

[14] Davies A.M. Solution of the 3D linear hydrodynamic equations using an enhanced eigenfunction approach. *International Journal for Numerical Methods In Fluids*, 13:235–250, 1991.

[15] Davies A.M. Modelling currents in highly sheared surface and bed boundary layers. *Continental Shelf Research*, 12(1):189–211, 1992.

[16] De Vriend H.J. and M.J.F. Stive. Quasi-3d modelling of nearshore currents. *coastal Engineering*, 11:565–601, 1987.

[17] Dobson F. and B. Toulany. On the deep-water fetch laws for wind-generated surface gravity waves. *Atmosphere-Ocean*, 27(1):210–236, 1989.

[18] Earle M. D. and Bishop J. M. *A practical guide to ocean wave measurement and analysis*. ENDECO, INC., Mariton, MA U.S.A., 1979.

[19] Farringtong C. C., R. T. Gregory and A. H. Taub. On the numerical solution of Sturm-Liouville differential equations. *Method of Computation*, 11:131-150, 1957.

[20] Forristall G.Z. Three-dimensional structure of storm-generated currents. *J. Geophys. Res.*, 79(18):2721–2729, 1974.

[21] Forristall G.Z. Continental shelf currents in tropical storm Delia: observations and theory. *Journal of Physical Oceanography*, 7:532–546, 1977.

[22] Forristall G.Z. A two-layer model for hurricane-driven currents on an irregular grid. *Journal of Physical Oceanography*, 10:1417–1437, 1980.

[23] Godin G. *The Analysis of Tides*. University of Toronto Press, 1972

[24] Grant W., A Williams, and S. Glenn. Bottom stress estimates and their prediction on the Northern California continental shelf during Code-1: The importance of wave-current interaction. *Journal of Physical Oceanography*, 14:506–527, 1984.

[25] Hasselmann K. Wave-driven inertial oscillations. *Geophysical Fluid Dynamics*, 1:463–502, 1970.

[26] Hasselmann K. On the mass and momentum transfer between short gravity waves and larger-scale motions. *J. Fluid Mech.*, 50, part 1:189–205, 1971.

[27] Heaps N.S. On the numerical solution of the three dimensional hydrodynamic equations for tides and storm surges. *Memories Societe Royale des Science de Liege*, Ser.6:143–180, 1971.

[28] Heaps N.S. Three-dimensional model for tides and surges with vertical eddy viscosity prescribed in two layers, I Mathematical formulation. *Geophys. J.R. Astron. Soc.*, 64:291–302, 1981a.

[29] Heaps N.S. Three-dimensional model for tides and surges with vertical eddy viscosity prescribed in two layers, II Irish Sea with bed friction layer. *Geophys. J.R. Astron. Soc.*, 64:303–320, 1981b.

[30] Hearn C.J. and J.R. Hunter A new method of describing bottom stress in two-dimensional hydrodynamical models of shallow homogeneous seas, estuaries, and lakes. *Appl. Math. Modelling*, 12:573–580, 1988.

[31] Huang N.E. Mass transport induced by wave motion. *J. Mar.Res.*, 29:35 50, 1970.

[32] Hunter J.R. and C.J. Hearn. On the convolution method of describing bottom friction in depth-averaged models. *Journal of Physical Oceanography*, 18:1752 1754, 1988.

[33] Hunter J.R. and C.J. Hearn The single relaxation approximation for bottom stress in two-dimensional hydrodynamic models of shallow seas. *Continental Shelf Research*, 9(5):465–478, 1989.

[34] Jamart B.M. and J. Ozer. Numerical boundary layers and spurious residual flows. *J. Geophys. Res.*, 91(C9):10,621–10631, 1986.

[35] Jelesnianski C.P. "Bottom stress time-history" in linearized equations of motion for storm surges. *Mon. Weather Rev.*, 98(6):462–478, 1970.

[36] Jenkins A.D. A theory for steady and variable wind- and wave-induced currents. *Journal of Physical Oceanography*, 16:1370–1377, 1986.

[37] Jenkins A. D. Wind and wave induced currents in a rotating sea with depth-varying eddy viscosity. *Journal of Physical Oceanography*, 17:938–951, 1987a.

[38] Jenkins A. D. A Lagrangian model for wind- and wave-induced near-surface currents. *Coastal Engineering*, 11:513–526, 1987b.

[39] Jenkins A. D. The use of a wave prediction model for driving a near-surface current model. *Dt. hydrogr.*, 42 (3-6):133–149, 1989.

[40] Jordan T.F. and J. R. Baker. Vertical structure of time-dependent flow dominated by friction in a well-mixed fluid. *Journal of Physical Oceanography*, 10:1091–1103, 1980.

[41] Lardner R.W. and H.M. Cekirge. A new algorithm for three-dimensional tidal and storm surge computations. *Appl. Math. Model*, 12:471–571, 1988.

[42] Lardner R.W. Numerical solution of the linearized three-dimensional tidal equations using eddy viscosity eigenfunctions. *Journal of Geophysical Research*, 95(C12):22269–22274, 1990.

[43] LeBlond P. H. and L. A. Mysak. *Waves in the Ocean*. Elsevier Scientific Publishing Company, 1978.

[44] Lee T.N., E. Williams, J. Wang, and R. Evans. Response of South Carolina continental shelf waters to wind and Gulf Stream forcing during winter of 1986. *J. Geophys. Res.*, 94(C8):10715–10754, 1989.

[45] Lentz C.D. and S.J. Winant Subinertial currents on the Southern California shelf. *Journal of Physical Oceanography*, 16:1737–1750, 1986.

[46] Lively R. R. Current meter, meteorological, sea-level, and hydrographic observations for the CASP experiment off the coast of Nova Scotia. Technical report, Physical and Chemical Sciences Branch, Scotia-Fundy Region, Department of Fisheries and Oceans; Bedford Institute of Oceanography, 1988.

[47] Longuet-Higgins M.S. Mass transport in water waves. *Phil. Trans. Royal Soc.*, A245:535–581, 1953.

[48] Longuet-Higgins M.S. The mechanics of the boundary-layer near the bottom in a progressive wave. — appendix to R. C. H. Russell and J. D. C. Osorio, "an experimental investigation of drift profiles in a closed channel.". In *Proc. 6 th Conf. on Coastal Engng.*, pages 171–193, Berkeley, 1958.

[49] Longuet-Higgins M.S. Mass transport in the boundary layer at a free oscillating surface. *J. Fl. Mech.*, 8:293–306, 1959.

[50] Longuet-Higgins M.S. and R.W. Stewart. Changes in the form of short gravity waves on long waves and tidal currents. *J. Fluid Mech.*, 8:565 583, 1960.

[51] Longuet-Higgins M.S. Radiation stresses in water waves; a physical discussion, with applications. *Deep-Sea Research*, 11:529–562, 1964.

[52] Longuet-Higgins M.S. On the transport of mass by time-varying ocean currents. *Deep-Sea Research*, 16:431–447, 1969a.

[53] Longuet-Higgins M.S. A nonlinear mechanism for the generation of sea waves. *Proc. Roy. Soc.*, A. 311:371–389, 1969b.

[54] Lynch D. R., F. E. Werner, D. Greenberg, and J. W. Loder. Diagnostic model for baroclinic, wind-driven and tidal circulation in shallow seas. *Continental Shelf Res.*, 12:37–64, 1992.

[55] Madsen O.S. Mass transport in deep water waves. *Journal of Physical Oceanography*, 8:1009–1015, 1978.

[56] Masse A.K. *Estuary-shelf interaction: Delaware Bay and inner shelf.* PhD thesis, University of Delaware, 1988.

[57] Murty T. S. *Storm Surges*, Bulletin 212. Canadian Bulletin of Fisheries and Aquatic Sciences, 1984.

[58] Pedlosky J. *Geophysical Fluid Dynamics.* Springer-Verlag, 1979.

[59] Pettigrew N.R. *The Dynamics and kinematics of the Coastal Boundary Layer off Long Island.* PhD thesis, Woods Hole Oceanographic Institution, 1981.

[60] Phillips O.M. *The Dynamics of the Upper Ocean.* Cambridge University Press, 2nd edition, 1977.

[61] Platzman G. W. The dynamical prediction of wind tides on Lake Erie. In *Meteorological Monographys*, volume 4, pages 1–44. American Meteorological society, 1963.

[62] Pollard R.T. Surface waves with rotation: an exact solution. *J. Geophys. Res.*, 75:5895–5898, 1970.

[63] Press W. H., S. A. Teukolsky, W. T. Vetterling, and B. P. Flannery. *Numerical Recipes.* 2nd edition, 1992.

[64] Russell R. C. H. and J. D. C. Osorio, 1958 (see the reference for Longuet-Higgins, 1958).

[65] Seber G.A.F. *Linear Regression Analysis.* John Wiley & Sons, New York, 1977

[66] Sheng J. and K. R. Thompson. A modified Galerkin-spectral model for three-dimensional, barotropic, wind-induced shelf circulation. *J. Geophys. Res.*, 98(C4):7011–7022, 1993.

[67] Simons T.J. *Circulation Models of Lakes and Inland Seas*, Bulletin 203. Canadian Bulletin of Fisheries and Aquatic Sciences, 1980.

[68] Stokes G.G. On the theory of oscillatory waves. *Trans. Camb. Phil. Soc.*, 8:441–455, 1847.

[69] Svendsen Ib. A. Velocities in combined undertow and longshore currents. *Coastal Engineering*, 13:55–79, 1989.

[70] Tolstov G. P. *Fourier Series.* Prentice-Hall, Inc., 1962.

[71] Trowbridge J. and O. S. Madsen. Turbulent wave boundary layers 1. model formulation and first-order solution. *J. Geophys. Res.*, 89(C5):7989–7997, 1984a.

[72] Trowbridge J. and O. S. Madsen. Turbulent wave boundary layers 2. second-order theory and mass transport. *J. Geophys. Res.*, 89(C5):7999–8007, 1984b.

[73] Ünlüata Ü. and C. C. Mei. Mass transport in water waves. *J. Geophys. Res.*, 75:7611–7618, 1970.

[74] Ursell F. On the theoretical form of ocean swell on a rotating earth. *Mon. Not. R. Astron. Soc., Geophys. Suppl.*, 6:1–8, 1950.

[75] Weber J.E. Steady wind- and wave-induced currents in the open ocean. *Journal Physical Oceanography*, 13:524–530, 1983a.

[76] Weber J.E. Attenuated wave-induced drift in a viscous rotating ocean. *J. Fluid Mech.*, 137:115–129, 1983b.

[77] Weber J.E. Eulerian versus Lagrangian approach to wave-drift in a rotating ocean. *Vetenskaps och Vitterhets-samhället, Göteborg. Acta Geophysica*, 3:155–170, 1990.

[78] Weber J.E. and Arne Melson. Volume flux induced by wind and waves in a saturated sea. *J. Geophy. Res.*, 98(C3):4739–4745, 1993a.

[79] Weber J.E. and Arne Melson. Transient ocean currents induced by wind and growing waves. *Journal Physical Oceanography*, 23:193–206, 1993b.

[80] Welander P. Wind action on a shallow sea: Some generalizations of Ekman's theory. *Tellus*, IX:45–52, 1957.

[81] Welander P. Numerical prediction of storm surges. In H. E. Landsberg and J. Van Mieghem, editors, *Advances in Geophysics*, volume 8, pages 316–379. Academic Press, New York and London, 1961.

[82] Zitman T. Quasi three-dimensional current modelling based on a modified version of Davies' shapefunction approach. *Continental Shelf Research*, 12(1):143–157, 1992.

[83] Zwillinger D. *Handbook of Differential Equations*. Academic press, Inc., 1989.

END

05-02-96

FIN